# $GaAs/Al_xGa_{1-x}As$ Quantum Well Lasers Grown on GaAs and Si by Molecular Beam Epitaxy

Thesis by

Howard ZeHua Chen

In Partial Fulfillment of the Requirements

for the Degree of

Doctor of Philosophy

California Institute of Technology

Pasadena, California

1990

(Submitted November 6, 1989)

*To My Parents*

## Acknowledgments

I would like to express my most sincere gratitude and deepest appreciation to my advisor Professor Amnon Yariv, who taught me quantum physics and optoelectronics when I was an undergraduate, and encouraged and supported me in my graduate years at Caltech. His powerful vision has guided me throughout the entire research. It has been a privilege to work in his highly motivated quantum electronics group.

A very special thanks goes to Professor Hadis Morkoç of University of Illinois, who is one of the finest scientists in this research field and definitely the most dedicated one I have known. Hadis collaborated with me during my most productive year, when many technological breakthroughs were made. His vast knowledge has been an instant solution to many problems I have encountered. Hadis has not only taught me the art of MBE (*Many Beautiful Evenings*) growth when everything is working, but how to use it when things are broken (*Mostly Broken Equipment*). Without his help, this thesis would never have been written.

A special thanks also goes to Mr. Ali Ghaffari who has helped me with MBE operations, device fabrications, and testings throughout the entire research presented here, in the most helpful way, often beyond the duties of any research engineer.

I would also like to express my appreciation to Mr. Joel Paslaski, for many fruitful and stimulating discussions. I have benefited significantly from his excellent physical insight, his experimental techniques, and his help with the high-speed measurements.

I am indebted to Dr. L.C. Chiu who first introduced me to the quantum electronics group and worked with me in my early years and remains a valued friend. I have learned from Dr. S. Margalit who has helped me with numerous discussions on device physics, Dr. A. Larsson who has helped me to learn MBE operations, and Dr. H. Wang who has helped me with device processing techniques. Mrs. Jana Mercado and Mr.

Desmond Armstrong also helped me throughout my graduate study and deserve me special thanks. I have also benefited from discussions with Mr. Lars Eng, Mr. Hal Zarem, Mr. Sidney Kan, Mr. Michael Mittelstein, Mr. Ilan Grave, Mr. Victor Leyva, and Mr. Steve Sanders. Steve Sanders has also read the entire thesis and made many valuable suggestions.

Professor Kerry Vahala and Mr. Michael Hoenk have also with me in this research and deserve my thanks.

I would like to thank Ms. Paula Samazan of the applied physics library for her assistance in literature search.

Finally, the financial support of the California Institute of Technology is greatly appreciated.

## Abstract

Molecular beam epitaxy (MBE) has been known as a "black art" since its invention in the early 1970's. The main goal of this thesis is to present practical techniques used daily MBE experts which have never been discussed in the literature. If this thesis can make a small step toward a better understanding and utilization of this technology, the author is more than satisfied.

The following is a summary of experimental and theoretical work of GaAs-on-GaAs and GaAs-on-Si material growth by MBE. Except for the relatively new GaAs-on-Si research, background information is presented at a minimum level. Emphasis is made on both theoretical and experimental *techniques* rather than on general discussions which exist in the literature.

The thesis begins with an introduction, in Chapter 1, to activities in molecular beam epitaxy and related crystal growth methods as well as their applications in the field of optical interconnects using low-threshold lasers and high-speed photodetectors.

In Chapter 2, a Green's function formulation of interface matching problems is presented. A very simple equation can be derived, which can provide some support to a very controversial, yet highly successful and very popular quantum dipole model for Schottky barriers and heterojunctions by J. Tersoff. A simplified model can be obtained, which eliminates the uncertainties in Tersoff's scheme and predicts very well the band offsets for several important semiconductor heterosystems including GaAs/AlAs. The theory is found to be in excellent agreement with a photoelectric measurement on the band offsets of the GaAs/AlGaAs system.

Chapter 3 deals with details of MBE growth of GaAs/AlGaAs quantum well laser material on GaAs substrates. Various growth techniques and substrate orientations are discussed. The dependence of threshold current density of a GaAs/AlGaAs GRINSCH

laser on quantum well thickness is experimentally studied. The experimental results are in good agreement with a qualitative analysis. A theoretical discussion of the effect of quantum well thickness on the threshold current density is used to explain the experimental results. Furthermore, this study has achieved for the first time, threshold current densities below 100 A/cm$^2$ in any semiconductor laser. The transparency current density obtained in this study, 60 A/cm$^2$, is very close to the theoretical prediction of 63 A/cm$^2$. It also establishes a record of lowest threshold current density for any semiconductor lasers.

Chapter 4 presents some important issues in GaAs-on-Si research. Both the potentialities and limitations of GaAs-on-Si technology are discussed. The main advantage of GaAs-on-Si technology is the special features of Si substrates not available in GaAs substrates.

Chapter 5 discusses the experimental aspects of GaAs-on-Si laser growth by MBE. The formation and prevention of antiphase domains (APDs) are discussed. Various methods to reduce defect density are presented. The first low threshold current density GaAs-on-Si laser growth by MBE, and the first room temperature continuous wave (CW) operation are described in detail. Important applications such as high-speed modulation of GaAs-on-Si stripe lasers and high-speed GaAs-on-Si p-i-n photodiodes are also presented.

Appendix I summarizes the operation and maintenance of a Riber 2300 MBE system from a practical point of view. Only several components in this MBE system are absolutely needed to grow high quality materials. It also discusses the routine material calibrations performed. Appendix II, III, IV, V, and VI deal with the details of material processing and device fabrication.

# Table of Contents

**Chapter 1 An Introduction**

**Chapter 2 Band Offsets at a Heterojunction**

**Chapter 3 MBE Growth of GaAs-on-GaAs Quantum Well Lasers**

# Chapter 1

## An Introduction

### § 1.1 An overview of activities in MBE

Molecular beam epitaxy (MBE) [1] is an ultra-high vacuum thin film technology developed in the early 1970's. It has been used extensively in laboratories to produce materials for the study of fundamental semiconductor properties and for the fabrication of novel microwave and optoelectronic devices. At present, materials routinely deposited by MBE include, from the III-V category, GaAs, AlGaAs, GaP, AlAs, GaAsP, GaSbAs, InP, InGaAs, InAlAs, InSb, InAs, InGaP, etc.; from the IV category, Si, Ge, SiGe; from the II-VI category, CdTe, CdS, ZnTe, HgCdTe; and from IV-VI category, PbTe, PbSe, PbSnTe, PbSnSe, as well as several metals, Al, In, W, Mo, Au, Pt, Ti, $CoSi_2$, $NiSi_2$.

The major achievements of MBE research can be summarized as:

*1) control of interface abruptness and doping profiles to monolayer precision*

*2) high device-quality materials growth*

*3) microwave devices such as IMPATT diodes, mixer diodes, MESFETs, HEMTs, HBTs; and optoelectronic devices such as LEDs, quantum well lasers, graded bandgap detectors, and multiquantum well structures*

*4) development of heteroepitaxies such as GaAs-on-Si technology*

*5) surface, heterojunctions, and interface studies*

*6) novel quantum well (wire) devices grown on patterned substrates.*

The dramatic expansion in the activity of MBE research is also shown by the rapidly growing number of institutions currently using this technique. In 1979, their number was only about 30 worldwide. Today, their number is estimated to be about 400. In addition to the United States, Japan, and Europe, countries such as Canada, Australia, India, China, and even Saudi Arabia are actively engaging themselves in MBE research. Furthermore, MBE systems have grown out of the experimental phase, and sophisticated versions are now commercially available from several companies.

## § 1.2 The role of MBE in III-V technology

Two epitaxial methods being successfully applied to the growth of high quality III-V compound materials are MBE and MOCVD (metal organic chemical vapor deposition) as well as their variations. MBE and MOCVD are two fundamentally different crystal growth methods: MBE is primarily a non-equilibrium process while MOCVD is a quasi-equilibrium process. In comparison to MOCVD, MBE offers a superior capability in generating highly complex compositional and doping profiles required for high performance devices. This strength is the result of the conceptual simplicity of the MBE growth process, where doped III-V layers are produced by laying down the constituent III-V elements and dopants atom by atom. MBE growth can be understood without using either thermodynamics or crystalline physics. The composition of a layer and its doping level depend only on the arrival rate of the participating atoms, which depends very simply on the production rate of their sources. The rate of production of the sources can be very easily and accurately controlled by effusion cell temperatures. An MOCVD, however, is complicated by the need for chemical decomposition of the starting materials at elevated temperatures which introduces both diffusion and autodoping problems. Furthermore, fine control of atomic abruptness is severely affected by finite gas flow velocities and boundary layer effects.

Ideally, MBE is a much simpler process for crystal growth compared to MOCVD, and all of the record-making microwave and optoelectronic devices are grown by MBE. The widespread application of MBE systems in industry, however, will ultimately depend on the possibility of carrying over their high performance into a production environment at an acceptable cost. Today, a fully equipped MBE system can cost as much as $1,000,000, compared with $500,000 for a fully equipped MOCVD system. The MBE grown wafer area is also limited by the size of a single substrate, where as MOCVD can process many wafers at the same time. The cost and throughput definitely favor MOCVD.

But when performance is of paramount importance, MBE has an edge; for example, there are several devices that have to be fabricated from MBE grown wafers. One example is the low-threshold CW GaAs-on-Si quantum well lasers [2]. Since MBE is a relatively low temperature, non-equilibrium growth, the defects due to the lattice and thermal mismatch are likely to be localized and usually will not affect the device operation a few $\mu$m away from the GaAs/Si interface. Results up to now show that room temperature CW operation can be obtained only with MBE grown wafers. A second example is the ultra-low-threshold current GaAs/AlGaAs buried heterostructure stripe lasers [3], which are grown by liquid phase epitaxy (LPE) on top of the properly etched MBE grown quantum well laser structures. During LPE regrowth, a high growth temperature of about 850°C causes dopant atoms to diffuse. To prevent this problem, a carefully designed doping profile is needed in the first growth of the laser structure which can be easily done by MBE. Recently, MBE growth on non-planar GaAs substrates using orientation dependent growth rate, has resulted in the lowest threshold current laser [4] *without* the difficult second LPE regrowth (the same can not be done with a MOCVD due to its equilibrium nature), and has further demonstrated the enormous potential of this ever improving technology.

Until MOCVD can rival its performance, MBE (and many of its improved versions) is here to stay, although its role may continue to be restricted to research laboratories. Recently, the discovery of high $T_c$ superconductivity materials have inspired researchers to grow superconductors using MBE ( not as a high vacuum system but an oxygen filled environment ) on GaAs and Si substrates. The success of this may open the way to a new superconductor technology based on MBE.

## § 1.3 Future trends in MBE

It is difficult to predict exactly where the field of MBE research and technology is headed; however, there are several obvious areas that are scientifically challenging and commercially profitable, which are expected to be explored very intensely in the near future. They are:

1) *GaAs-on-Si.* This is a field that offers numerous opportunities and challenges. Presently, almost all the popular microwave and optoelectronic devices have already been demonstrated, despite of the difficulty of GaAs-on-Si growth. The main problem areas remaining are the high defect density in GaAs, the control and localization of interface defects and strain, the improvement of device performance, and the development of the applications GaAs-on-Si technology has promised.

2) *GaAs/AlGaAs.* Although much has been done, there remains the unresolved problem of heterojunction band discontinuity and the physics on the heterointerfaces. We still know embarrassingly little about the microscopic nature of a heterojunction interface. Theoretical models need to be developed that can explain the experimental data.

3) *GaSb/InAs.* This is an unusual combination of III-V with III-V compounds where the conduction band edge $E_c$ of InAs lies about 0.14 eV below the valence band edge $E_v$ of GaSb at the $\Gamma$ -point of the Brillouin zone. As a result, in a GaSb/InAs superlattice, confined electrons and holes are spatially separated. Consequently, the GaSb/InAs structure does not need additional impurities to generate a two-dimensional electron gas. Since the electron mobility in InAs is twice that in GaAs, we can expect the electron mobilities in GaSb/InAs heterostructures in excess of $10^6 \mathrm{cm}^2\mathrm{V}^{-1}\mathrm{s}^{-1}$.

4) *MBE growth on non-planar substrates.* Results so far have shown that the growth rate depends on the orientation of substrate, and the underlying physics is still being investigated [5]. It has also been established that even the type of doping depends on the orientation. These two features can be used as powerful tools to fabricate novel lateral structures such as the V-groove low-threshold lasers.

5) *Novel MBE systems.* These include CBE (chemical beam epitaxy) [6] which combine the advantages of MBE and MOCVD, and GSMBE (gas-source MBE) [7]. They provide a long-term supply of source materials without breaking the vacuum which is very desirable in mass production, and they offer easy control of As to P flux ratio in growing GaInAsP quaternary material that cannot be done with conventional solid-source MBE. The only drawback has been the safety concerns over the use of highly toxic gases. A comparison of MBE and MOCVD related crystal growth methods are listed in **Figure 1.1.**

6) *In situ processing.* The combination of ion beam etching techniques and molecular beams in an MBE system offers an opportunity to complete the material growth, masking, etching, and metalization steps in an MBE system without breaking the vacuum. Such a technology is potentially more reliable and more cost-effective.

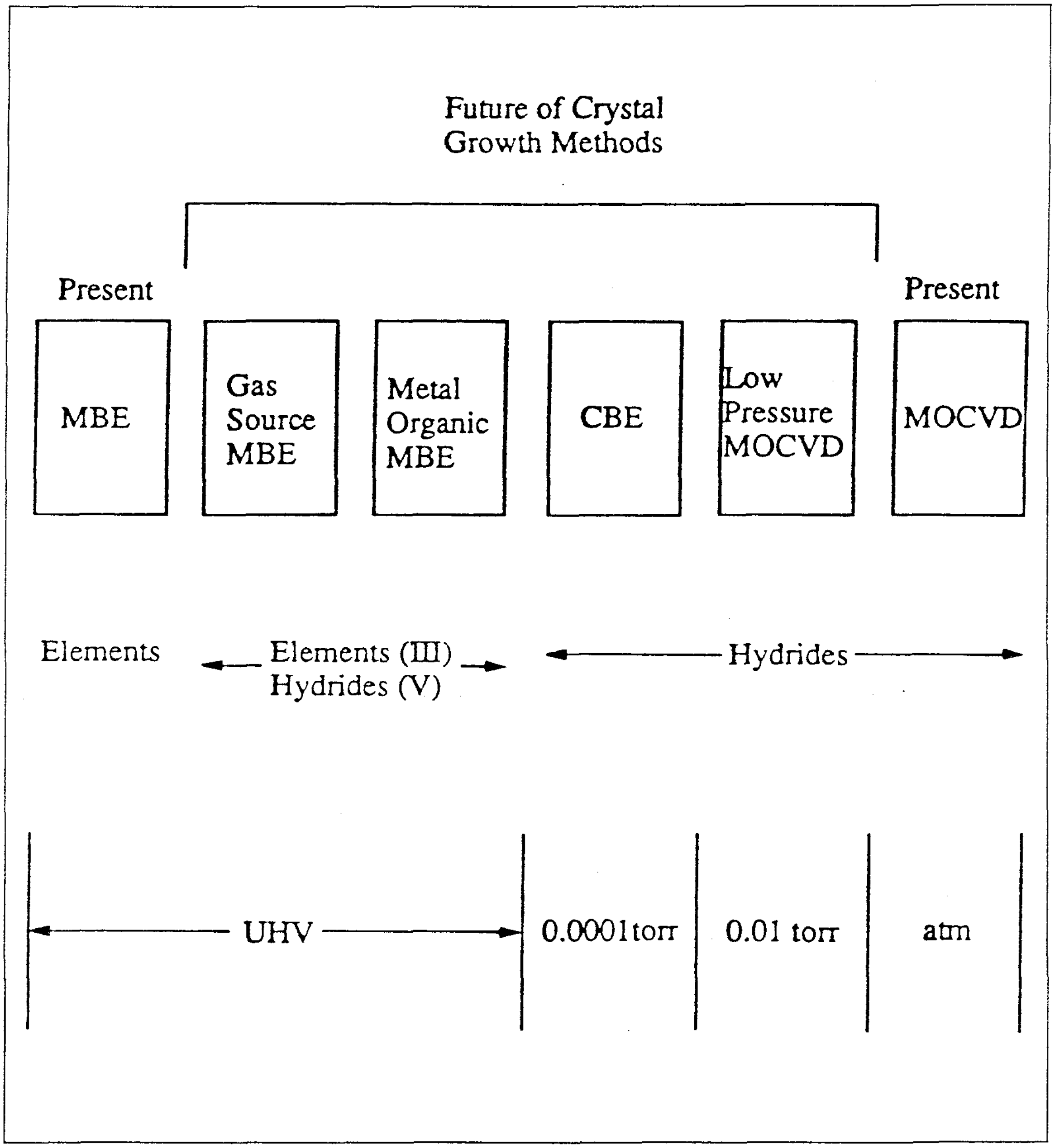

**Figure 1.1** *A comparison of the MBE and MOCVD growth methods.*

Research in other areas such as III-V compounds grown on group IV element systems, group IV Si/Ge systems, Si-on-GaAs materials, IV-VI (e.g., PbTe/SnPbTe) compounds, semiconductor semimetal (e.g., CdTe/HgTe) structures, semiconductor-metal (e.g., metal-GaAs) structures, semiconductor-insulator (e.g., GaAs/$SiO_2$) structures, metal-metal (e.g., Nb/Cu) structures, strained layer (e.g., GaAs/InAs) superlattices, and doping (n-i-p-i) superlattices, will also be expected to continue.

## § 1.4 An overview of activities in optical interconnects

Future high-speed digital computers will process a tremendous amount of data to meet the ever growing demand in science and technology. The throughput of a computer has to be increased dramatically from the current level. To achieve this goal, denser and faster integrated circuits and new computer architectures are being developed. Currently, *electrical interconnects* and *switching speed* have been identified as the two major bottlenecks to throughput of computing systems. We will not be able to take full advantage of the development of high-speed Si (gate delay is now 11 ps) and GaAs (gate delay is now 5 ps) switching and parallel architecture, unless we can solve the interconnect problem.

### Interconnections in a VLSI system

A modern computing system functions by bringing a large number of separate elements to bear on a common problem. Coordinated operation of the elements requires a large amount of communication among them through many long wires. Variability in manufacturing and fluctuation in a system causes the elements of a system to differ from one another in their response to signals. Therefore, signals must be large enough to be interpretable by any element of the system. This means high-power dissipation over a finite length of interconnections. Thus, fitting a complex interconnection pattern into a small space becomes the most limiting factor in a computer system (the other one being the switching speed of an element).

Currently, the study of communication and information is aimed at providing the largest bandwidth and lowest power possible in a system. In general, we are faced with a few fundamental limits that are unique to a computing system. First, the nature of a computing system which requires more than two streams of information to interact indicate that the times of arrival of information at a device are extremely important. Second, the coding of data streams that allows efficient use of a communication channel capacity can not be applied to a computer because the methods of information processing through the interaction of two or more streams of coded data are not known yet.

Experimentally, the packaging of microelectronics presents an enormous problem for system designers. In the following, we briefly discuss the complexity involved in packaging of a VLSI system [8]. First, we need to introduce a few terms used in computer science.

A *block graph* is a structure consisting of interconnected blocks.

A *block* is an abstract element in a system which can be an NAND gate, a storage element, a register, or an integrated circuit chip.

A *net* is an abstraction of electrical interconnection that carries a signal between the terminals of blocks connected.

A *module* is a container that holds blocks and connects nets.

### Rent's rule

The relationship between the average number of pins connecting a *module* to the *outside world* $P$, and the number of *blocks* contained in that *module* $B$ can be described by Rent's rule which was discovered by E. F. Rent [9] of IBM in 1960 in a study of the IBM series 1400 computers. It states that:

$$P = KB^{\alpha} \tag{1.1}$$

where $K$ is the average number of pins per block and $\alpha$ is an exponent. For the IBM system/360 machines, $K = 4$ and $\alpha = 0.7$. Therefore, we get $P = 4B^{0.7}$.

Rent's rule can not be proved mathematically, but is rather taken as a empirical law of nature. Communication systems obeying Rent's rule are common. One such example is a vertebrate nervous system where cerebral neurons are long dendrites and axons that allow communication with others.

Using Rent's rule, Donath [10] has calculated the average interconnection length $l$ on an integrated circuit as a function of circuit complexity $N$

$$l = l_c\, a(\alpha) N^{\alpha - 1/2} \qquad \alpha > 1/2 \tag{1.2}$$

where $a(\alpha)$ is a proportionality constant related to layout technology, and $\alpha$ is the Rent exponent. For very complex circuits, the interconnection length is expected to increase exponentially with complexity. There is, however, a limit on the interconnection length $l$ given by

$$l \approx v\, \tau_r = \frac{c}{n} \tau_r \tag{1.3}$$

where $v$ is the speed of the signal, $n$ is the index of refraction of the medium surrounding the connection line, and $\tau_r$ is the pulse rise time. When the interconnection length is comparable to $v\tau_r$, the clock phasing and system synchronization becomes difficult. How optical interconnects can help in such a complex system is discussed below.

## § 1.5 Signal fan-out: electrical vs. optical interconnects

Deciding between electrical and optical interconnects is a complex task [11]. Although fiber optic transmission techniques have some intrinsic merits, the existing computer architectures are based on electrical interconnects and can seriously limit the application of optical interconnects. In general, insertion of optical interconnects as a direct one-to-one replacement of point-to-point electrical interconnects does not offer any advantages for present-day computer systems. This is because: (1) overall system reliability would decrease because of the use of hybrid optical components, (2) overall system power consumption can increase because of the inefficiency of the optical-to-electrical conversion, and (3) increased costs due to the increase in packaging complexity [12]. The cost factor can be offset by higher performance; the high-power consumption can be reduced with sub-milliamper threshold lasers and high quality photodetectors, but the system reliability issue can not be solved easily. It is therefore desirable to use as few optical interconnects as possible, in the most effective places. One area where optical interconnects can improve system performance is where large signal fan-outs are required over long distance and at high-speeds.

High electrical fan-outs are common at the intra-chip and interboard levels, including data bus, control lines, and clock lines.

### Electrical fan-outs

If the distance between two elements on a transmission line is much less than the wavelength of the signal (at microwave frequencies it is about 3cm at 10GHz), the entire fan-out system can be viewed as a single transmission line with a load increasing with distance [13]. The impedance of a transmission line is

$$Z = \sqrt{\frac{L}{C}} \tag{1.4}$$

where L and C are the inductance and capacitance per unit length. Without fan-out, the unloaded line has an impedance of

$$Z_0 = \sqrt{\frac{L_0}{C_0}} \tag{1.5}$$

With loading, the capacitance per unit length is changed to

$$C = \frac{C_0 C_l}{C_0 + C_l} \tag{1.6}$$

where $C_0$ and $C_l$ are unloaded and distributed loading capacitance due to fan-outs. Substitute $C$ into eq.(1.4), we get the impedance on the line a distance $d$ away from the starting point

$$Z(d) = \frac{Z_0}{\sqrt{1 + C_{load}/C_0 d}} \tag{1.7}$$

where $C_{load}$ is the total load capacitance, $d$ is the line length, $C_0$ is the intrinsic line capacitance. For example, if $C_0 = 1\text{pF}$, $C_l = 3\text{pF}$, then after 5 fan-outs the characteristic impedance drops from a standard 50 ohms to 25 ohms. As a result, the driving power has to be increased to maintain a constant signal level.

Another effect due to increased fan-out is the propagation delay. Since the velocity of propagation is given by

$$v = \frac{1}{\sqrt{LC}} \tag{1.8}$$

we have

$$t(d) = t_0(d) \sqrt{1 + \frac{C_{load}}{C_0 d}} \tag{1.9}$$

The increase in propagation delay is due to the charging-up of capacitive elements at each fan-out.

While the increase in driving power is not fundamentally limiting since the driver lines can be designed to carry enough power, the propagation delay decreases the critical line length $l_c$, which is the distance that an electrical signal can travel without causing any clock (signal) skew.

## Optical fan-outs

The fundamental difference between electrical and optical fan-outs is that in the case of electrical fan-outs, the signal travels in the media surrounding the transmission line (usually the ceramic or polyimid printed circuit board), where as for optical fan-outs, the signal travels in a guided media, the optical fiber. In an optical fiber, the effect of capacitive loading does not exist since no conductor is used. The number of fan-outs for optical interconnects is limited by the available power to the detectors. The amount of power available to the detectors is determined from the source power and the distributed losses throughout the system. Optical fan-out is achieved by power splitting of a channel. The fan-out can be done in star, tree, or tap networks. The power should be split equally among $n$ detectors. In addition to the distributed loss, there is an excess loss due to the imperfect coupling. Assuming a tree fan-out structure, the total power loss can be written as [14]:

$$\alpha \;=\; 10\ log(\frac{1}{n}T^{log_2 n}) \tag{1.10}$$

where $n$ is the number of fan-outs, and $T$ is the transmission percentage of each of the couplers in the tree. Let the sensitivity of detectors used in the system be $P_{min}$; then the maximum number of optical fan-outs can be calculated by

$$P_{source} + \alpha \;=\; P_{min} \tag{1.11}$$

### Electrical vs. optical fan-outs

The optical fan-outs can offer a higher fan-out speed since there is no additional propagation delay, and they do not require increased driving power.

Unterminated electrical transmission lines are limited by the critical line length ( given the total $C_{load}$ for the entire system, the line length dominates ) while terminated transmission lines are limited by the density of fan-out ( given the total line length, the per unit length capacitance dominates ) along the line.

It is obvious from the above analysis that optical interconnects should be used to implement data buses and distribution structures within computing systems which are currently limited by electrical interconnects.

The work to be presented in Chapters 4, 5, and 6, is part of the effort to explore the possibility of using optoelectronics in future computer systems.

## § 1.6 low-threshold lasers for inter-chip communication

When system considerations justify the use of optical interconnects, lasers and detectors can be used as inter-chip high-speed links over a long distance. The fiber media is lightweight, low loss (can travel a few hundred miles), and virtually bandwidth unlimited over a short distance. A laser can also function as a detector when reverse biased. Therefore, it can perform both fan-in and fan-out for a digital processing system. Two key issues are (i) operating power and (ii) lifetime of these devices. To this date, the best GaAs/AlGaAs lasers have a 0.55mA threshold current [3]. Notice however that (i) these are GaAs/AlGaAs lasers which have yet to show a long lifetime which in the past has been limited by dark line defects, (ii) integration of these low-threshold lasers and high-speed photodetectors on the same chip has not been demonstrated, (iii) the requirement of cleaving mirrors makes it incompatible with existing planar processing technology, and (iv) the performance of these low-threshold lasers under mechanical vibrations and thermal fluctuations in a real world environment is unknown. In this thesis, we will focus on the problem of threshold current, and will investigate experimentally and theoretically the lowest possible threshold current that can be achieved in a GaAs/AlGaAs quantum well laser.

## § 1.7 GaAs-on-Si detectors for optical clock synchronization

Some numerical data of a computer will help to understand the distance a signal has to travel. In the IBM 3081 computer, 100 chips are mounted on a ceramic 9×9 $cm^2$ module. Each chip contains about 100 signal pins. About 10 modules are mounted onto a board. Each module contains 100 m of wire and each board contains 1000 m of interconnections. The average length that a electrical signal has to travel can be as large as a few meters.

Suppose the clock signal is what we are talking about and the speed of it in a printed circuit board is 0.5c, then the time delay over one meter is about 7ns. This is 1000 times of the shortest gate delay available today.

In a VLSI system, parasitic transmission line capacitance and resistance cause a skew in clock signals arriving at different locations on the chip. An optical clock distribution system can capitalize on the three-dimensional nature of imaging optics and avoid transmission line propagation delays. The clock signal is mapped at the speed of light from an off-chip laser diode onto the surface of silicon chip. The VLSI system is synchronized by the many detectors over the entire chip. The high-speed GaAs-on-Si detectors [15] can be used for detection of clock broadcasting by a laser diode directly above the chip.

At this point, one may ask "why not make Si detectors on the same Si chip," the answer is, that Si has a much larger absorption depth than that of GaAs. At the wavelength of about 1.0$\mu$m, Si has an absorption depth of 10$\mu$m, where as GaAs has an absorption depth of 1$\mu$m. Therefore, at the same sensitivity level, Si requires an absorption region 10 times longer. In a typical p-i-n detector, Si will have an intrinsic region 10 times longer, resulting in a long sweep-out of photo-carriers. The smaller absorption depth and higher carrier velocity make GaAs p-i-n detectors much faster. In this thesis, a major effort is made to understand the growth process of GaAs-on-Si single quantum well lasers, and their operations under both CW and microwave modulation conditions.

## § 1.8 References

[1] A. Y. Cho, *The Technology and Physics of Molecular Beam Epitaxy*, ed. E. H. C. Parker, Plenum Press, New York, 1985, p. 1, and references therein.

[2] H. Z. Chen, J. Paslaski, A. Yariv, and H. Morkoç, *Research and Development*, p. 61, Jan. , 1988.

[3] P. L. Derry, H. Z. Chen, H. Morkoç, A. Yariv, K. Y. Lau, N. Bar-Chaim, K. Lee, and J. Rosenberg, J. Vac. Sci. Tech. , **B6**, 689(1988).

[4] E. Kapon, J. P. Harbison, C. P. Yun, and N. G. Stoffel, Appl. Phys. Lett. , **52**, 607(1988).

[5] M. Hoenk, H. Z. Chen, K. J. Vahala, A. Yariv, and H. Morkoç, to be published.

[6] W. T. Tsang, J. Crystal Growth, **81**, 261(1987), and references therein.

[7] M. B. Panish, Prog. Crystal Growth and Charact. , **12**, 1(1986), and references therein.

[8] B. S. Landman and R. L. Russo, IEEE Trans. Comp. , **C20**, 1469(1971).

[9] Rent never stated the equation, but corresponding analysis of his data revealed the relationship $P = KB^{\alpha}$, and was hence known as Rent's rule.

[10] W. E. Donath, IEEE Trans. Circuit. Syst. , **26**, 272(1979).

[11] J. W. Goodman, F. J. Leonberger, S. Kung, and R. A. Athale, Proc. IEEE, **72**, 850(1984).

[12] P. R. Haugen, S. Rychnovsky, A. Husain, and L. D. Hutcheson, Opt. Eng. , **25**, 1076(1986).

[13] W. R. Blood, *MECL System Design Handbook*, Motorola Corp. , Phoenix, Arizona, 1983.

[14] R. G. Smith and S. D. Personick, in *Semiconductor Devices for Optical Communications*, (Springer-Verlag, New York, 1980), p. 89.

[15] J. Paslaski, H. Z. Chen, H. Morkoç, and A. Yariv, Appl. Phys. Lett. , **52**, 1410(1988).

# Chapter 2

## Band Offsets at a Heterojunction

### § 2.1 An introduction

Perhaps the most important issue concerning a device physicist working with compound semiconductors is how energy bands line up at a heterojunction. In general, electrons and holes in a semiconductor move according to the forces exerted on them: one of which is due to the macroscopic electrostatic field in a region such as a p-n junction, and one which is due to the local electrical field resulting from a compositional gradient (better known as bandgap grading) typically caused by a band offset at a heterojunction.

The macroscopic electrostatic force either as a result of doping variation or the application of an external field, is responsible for the operation of a large class of electronic devices such as p-n junction rectifiers, bipolar transistors, and metal-oxide-semiconductors (MOS) which serve as the fundamental elements of today's VLSI technology. The above devices utilize what is known as *homojunctions* which do not have any bandgap variation.

A heterojunction, on the other hand, is formed with two semiconductors of different bandgaps, preferably with a lattice match. It adds a new degree of freedom, namely, the bandgap grading, to this field of device physics. In a heterojunction, the two forces acting on electrons and holes can be balanced to manipulate their motions (the quasi-electric field caused by bandgap grading can dominate the field caused by doping in a p-n junction). This is the principle behind the operation of a new class of devices employing heterojunctions: the separate confinement heterostructure quantum well lasers (the main subject of this thesis research and will be discussed later), high electron mobility transistors (HEMTs), and heterojunction bipolar transistors (HBTs). A good understanding of a heterojunction is essential to designing any heterojunction devices.

In general, the two energy bands line up in one of the three ways shown in **Figure 2.1**: straddling, staggered, or broken-gap. The way these two bands line up (the direction of quasi-electric field due to bandgap grading) determines the motion of electrons and holes that will rule device operations. In the following, I propose a one-parameter theory to predict the line-up of energy bands and band offsets at a heterojunction.

## § 2.2 Green's function in semiconductors

We begin our discussion by introducing a one-electron Green's function [1] in a semiconductor which will later be used to study interface matching. The definition of Green's function in quantum theory is quite general. If $|x>$ and $|y>$ are state vectors and $\mathbf{L}$ is a linear operator, and

$$\mathbf{L}|x> = |y> \qquad (2.1)$$

then we can formally write

$$|x> = \mathbf{L}^{-1}|y> \qquad (2.2)$$

The operator $\mathbf{L}^{-1}$ is defined as Green's operator for the operator $\mathbf{L}$ and is independent of choice of basis. Therefore, for the time-dependent Schödinger's equation

$$(i\hbar\frac{\partial}{\partial t} - \mathbf{H})\,|\Phi> = 0 \qquad \mathbf{G} = (i\hbar\frac{\partial}{\partial t} - \mathbf{H})^{-1} \qquad (2.3)$$

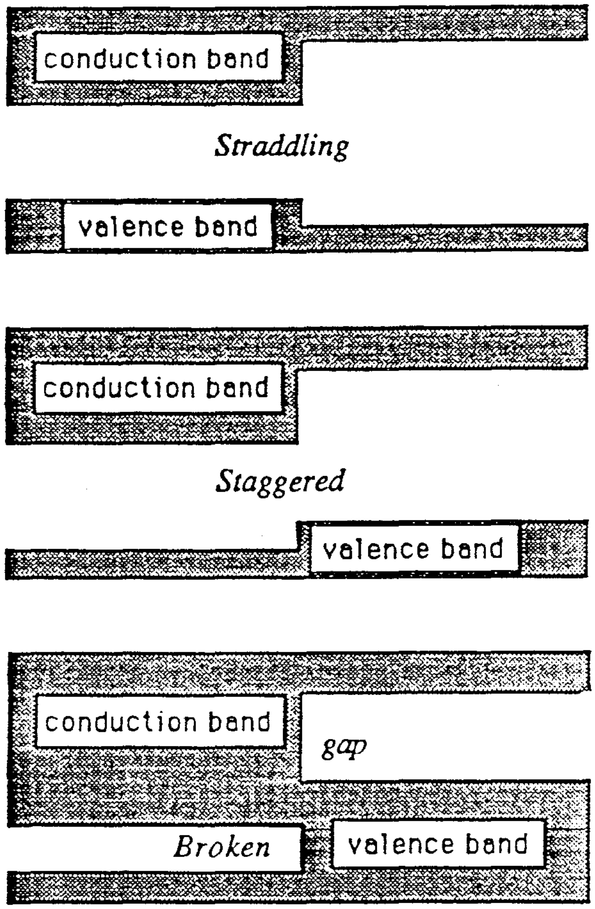

**Figure 2.1** *Schematic drawing of the three possible band line-ups : straddling, staggered, or broken-gap.*

and for the time-independent Schödinger's equation

$$(E - \mathbf{H})\,|\Phi> = 0 \qquad \mathbf{G} = (E - \mathbf{H})^{-1} \tag{2.4}$$

At this point, we want to choose a basis and obtain the spectral representation of the Green's function. Let $|n,\vec{k}>$ be any eigenstate; then by virtue of the unity operator we can write for the time-independent Schrödinger equation

$$\mathbf{G} = \mathbf{1}\,(E - \mathbf{H})^{-1} = \sum_{n,\vec{k}} \frac{|n,\vec{k}><n,\vec{k}|}{E - E_{n\vec{k}}} \tag{2.5}$$

One particular representation, the space coordination, is obtained by projecting **G** onto the coordinate eigenbasis $|\vec{r}>$. The matrix elements are obtained:

$$G(\vec{r},\vec{r'},E) = <\vec{r}|\mathbf{G}|\vec{r'}> = \sum_{n,\vec{k}} \frac{<\vec{r}|n,\vec{k}><n,\vec{k}|\vec{r'}>}{E - E_{n\vec{k}}} \tag{2.6}$$

where $<\vec{r}|n,\vec{k}>$ is the Bloch's wavefunction for a single electron

$$\psi_{n\vec{k}}(\vec{r}) = <\vec{r}|n,\vec{k}> = e^{i\vec{k}\cdot\vec{r}}u_n(\vec{r}) \tag{2.7}$$

and $E_{n\vec{k}}$ is the energy band $E_n(\vec{k})$.

## § 2.3 Physical significance of Green's function

A Green's function can be obtained in two ways. In the above, we followed a formal eigenfunction expansion method that is purely mathematical. Now we look at the Green's function from another angle: the response to a stimulus [2].

Consider two different semiconductors separated by an interface $\Sigma$. The quantum mechanical approach to solving for the wavefunctions and energy eigenvalues is the following:

1. *obtain a state $\psi$ that belongs to each bulk semiconductor with a decreasing magnitude toward the bulk, and*
2. *match these two states as well as their derivatives at the interface $\Sigma$.*

To carry out this procedure using Green's functions, some of the general features of Green's functions are recalled. If we have a linear operator **L**, a response $R$, and a stimulus $S$ satisfying

$$\mathbf{L}\,R = S \tag{2.8}$$

then Green's function $G$ is defined by

$$\mathbf{L}\, G \; = \; \delta(\vec{r}-\vec{r}')\delta(t-t') \tag{2.9}$$

plus the usual boundary conditions. The Green's function $G(\vec{r},\vec{r}',t,t')$ represents the quantum mechanical response at the point $(\vec{r},t)$ to a stimulus at the point $(\vec{r}',t')$.

It is especially important to realize this because we are studying an interface problem and we want to know how the bulk states and the surface states are related. In practice, $\vec{r}$ can be restricted to the surface $\Sigma$.

To obtain a state which is just inside a bulk semiconductor and decaying away from the interface $\Sigma$, let's use the Green's function for the time-independent problem $G(\vec{r},\vec{r}',E)$ and an unknown stimulus $S(\vec{r},E)$ on the interface $\Sigma$. The wavefunction is then

$$\psi(\vec{r},E) \; = \; \int_{\vec{r}'\in\Sigma} G(\vec{r},\vec{r}',E)S(\vec{r}',E)d\vec{r}' \tag{2.10}$$

The matching of wavefunctions across the interface gives:

$$\left\{ \begin{array}{rcl} G^1(\vec{r},\vec{r}',E)S^1(\vec{r}',E) & = & G^2(\vec{r},\vec{r}',E)S^2(\vec{r}',E) \\ \frac{\partial}{\partial z}G^1(\vec{r},\vec{r}',E)S^1(\vec{r}',E) & = & \frac{\partial}{\partial z}G^2(\vec{r},\vec{r}',E)S^2(\vec{r}',E) \end{array} \right. \tag{2.11}$$

Where both $\vec{r}$ and $\vec{r}'$ are on the surface $\Sigma$. Note that the integration has been dropped. From this system we get the secular equation for non-trivial $S(\vec{r},E)$

$$det \begin{pmatrix} G^1(\vec{r},\vec{r}',E) & G^2(\vec{r},\vec{r}',E) \\ \frac{\partial}{\partial z}G^1(\vec{r},\vec{r}',E) & \frac{\partial}{\partial z}G^2(\vec{r},\vec{r}',E) \end{pmatrix} \; = \; 0 \tag{2.12}$$

for all the energy states.

This result has been simplified by Garcia-Moliner and Rubio and Flores [2,3], if there is a planar interface in which case we can write

$$S^1(\vec{r}_s,E) \; = \; -S^2(\vec{r}_s,E) \tag{2.13}$$

then the first of the two matching conditions will give

$$det \mid G^1(\vec{r}_s,\vec{r}_s',E) \; + \; G^2(\vec{r}_s,\vec{r}_s',E) \mid \; = 0 \tag{2.14}$$

In what follows, we will use this result to examine the existing theories and develop a new one to predict the heterojunction band discontinuity.

## § 2.4 Quantum dipole theory

Based completely on another line of reasoning, J. Tersoff has proposed a theory [4] that treats *both* Schottky barriers and semiconductor heterojunctions. Tersoff argues that for both "Fermi-level pinning" and band line-up, there is a single energy level $E_B$ for each material, that will minimize the interface dipole when aligned at the interface. To find this $E_B$, he has proposed to calculate the zero of a spatially averaged Green's function

$$G(\vec{R},E) = \int d\vec{r}\, G(\vec{r},\vec{r}+R,E) = \sum_{n\vec{k}} \frac{exp(i\vec{k}\cdot\vec{R})}{E-E_{n\vec{k}}} \tag{2.15}$$

To do this, it is convenient to decompose $G$ into conduction and valence band contributions $G_c$ and $G_v$, which are obtained when the sum over states is carried out for conduction and valence bands separately. Since $E_B$ is usually in the bandgap (the only exception presented by Tersoff is InAs when $E_B$ is well above $E_c$), $G_c$ and $G_v$ have opposite signs and cancel each other, and when $|G_c| = |G_v|$ the value $E_B$ is obtained. **Figure 2.2** shows the positions of $E_c$, $E_v$, and $E_B$ and how one should use the value of $E_B$ relative to the valence band edge to line up the two bands.

The value of $E_B$ has been calculated and published by Tersoff for a number of important semiconductors [4]. The agreement with experiment, usually within 0.15 eV, is better than any other theory. This so called "quantum dipole theory," however, has raised some questions [5]. First, as has been pointed out by many authors, the zero of Green's function is not the energy at which the dipoles vanish or are minimized; second, as Tersoff has acknowledged, the zero for $G(\vec{R},E)$ often depends on $\vec{R}$, especially in the case of GaAs/AlAs line-up. Although all the measurements have been performed on the (100) oriented substrates, Tersoff's theory can only work for $\vec{R}$ along (110).

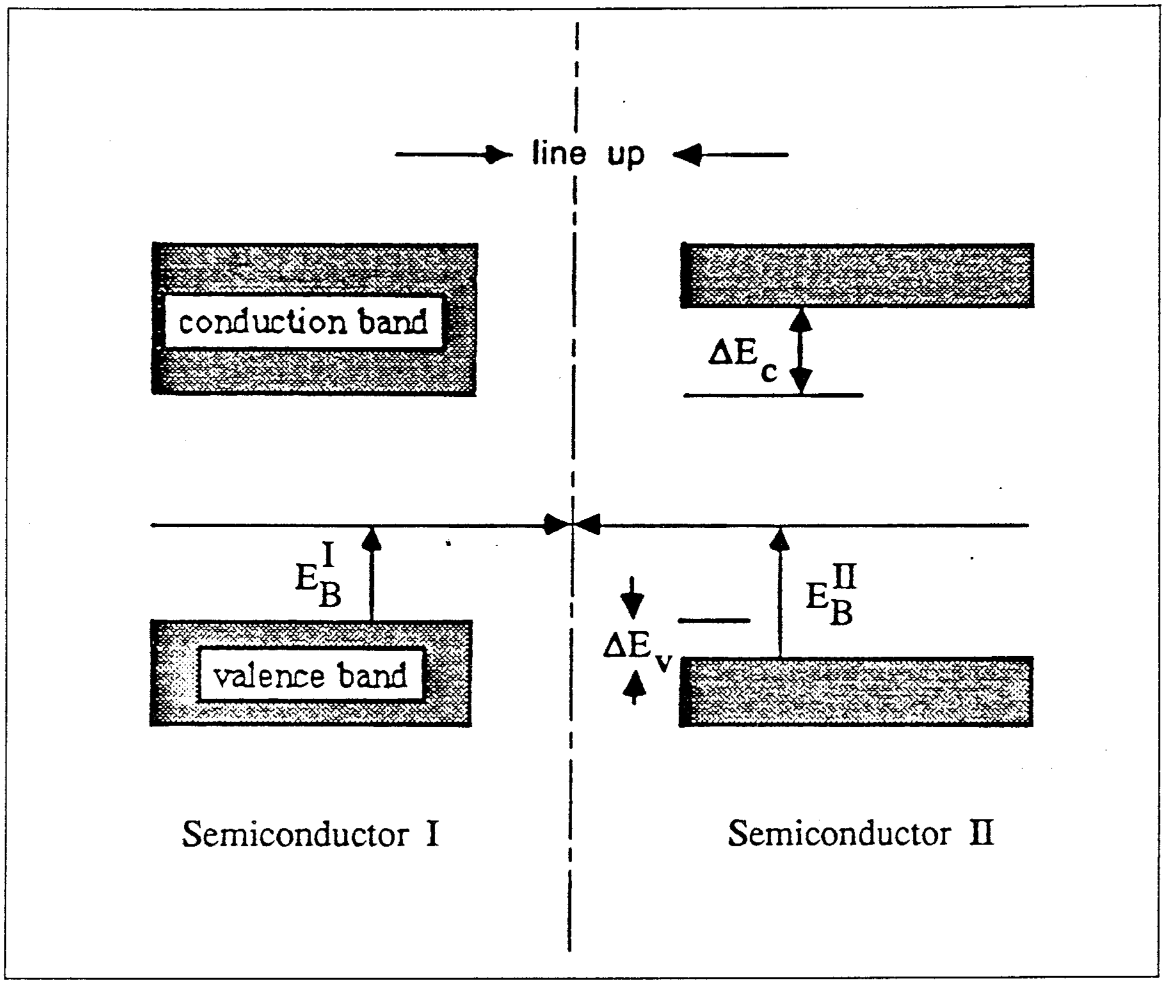

**Figure 2.2** *The line-up of two energy bands by a single energy level $E_B$, and the relative positions of $E_c$, $E_v$, and $E_B$.*

Third, in many cases, there is more than one energy for which $G(\vec{R}, E)$ goes to zero, making the calculation procedure ***arbitrary***. This theory also demands a reasonably good knowledge of the bulk energy structure $E_n(\vec{k})$, which is itself a very challenging topic.

Nevertheless, since the problem of heterojunction band line-up is so extremely difficult, no other theory (people have been studying this problem for over 30 years) has come even close to Tersoff's. This theory in a broader sense, as we will see later, can also be justified by the discussions presented before based on Garcia-Moliner and Rubio and Flores's framework on Green's function matching,

$$det \mid G^1(\vec{r_s}, \vec{r_s'}, E) \; + \; G^2(\vec{r_s}, \vec{r_s'}, E) \mid \; = 0 \tag{2.16}$$

Tersoff's approach is simply a special case (each element of the above matrix being zero) that is *spatially averaged* in the volume enclosing the interface of the above condition on the interface and does meet the requirement of wavefunction matching. Equation (2.16) illustrates the tremendous difficulty involved in interface matching calculations, and approximations have to be made in order to see some general trends.

## § 2.5 A proposed model for band alignment

At this point, it is very tempting to develop a simplified model which is based on Tersoff's original theory, but which does not require any specific knowledge of the band structure, and furthermore, does not depend on the orientation of the interface. Such a model would be very useful for experimentalists. Note that Tersoff's model can be defined if we choose

$$\underbrace{G_c^1(\vec{R}, E_B) \; + \; G_v^1(\vec{R}, E_B)}_{=0} + \underbrace{G_c^2(\vec{R}, E_B) \; + \; G_v^2(\vec{R}, E_B)}_{=0} \; = \; 0 \tag{2.17}$$

Recall that $G_{c,v}$'s are summed over conduction and valence states.

$$G_c(\vec{R}, E) \; = \; \sum_{\vec{k}_c} \frac{exp(i\vec{k} \cdot \vec{R})}{E - E_c(\vec{k})} \quad and \quad G_v(\vec{R}, E) \; = \; \sum_{\vec{k}_v} \frac{exp(i\vec{k} \cdot \vec{R})}{E - E_v(\vec{k})} \tag{2.18}$$

We may further require that when the contributions to the Green's function from conduction states cancel those from valence states, only contributions with the same $\vec{k}$ cancel. In other words, if a contribution to Green's function from $\vec{k}_c$ is $G_c(\vec{k}_c)$ and from $\vec{k}_v$ is $G_v(\vec{k}_v)$, then

$$|G_c(\vec{k}_c)| \; = \; |G_v(\vec{k}_v)| \qquad if \; and \; only \; if \qquad \vec{k}_c \; = \; \vec{k}_v \tag{2.19}$$

This imposed selection rule can be justified since $G(\vec{r},\vec{r}',E(\vec{k}))$ is the transition amplitude measured at $\vec{r}'$, given a stimulus and $E(\vec{k})$ at $\vec{r}$. In the framework of the one-electron theory, electrons with different $\vec{k}$'s do not interact, at least in the zeroth order. Therefore we can drop the summation over $\vec{k}$ in equation (2.18), and solve it for any given $\vec{k}$ in the first Brillouin zone. In particular, it should be true at the $\Gamma$ point ($\vec{k}$=0) of the Brillouin zone. While it may work at any other point, the $\Gamma$ point can eliminate the dependence of Green's function on $\vec{R}$ which seriously weakens the proposed Tersoff theory.

For most tetrahedral semiconductors, Kane's four-band $\vec{k}\cdot\vec{p}$ model [6] applies. There exist a total of four bands, namely, the conduction band, the light hole band, the heavy hole band, and the split-off band

$$\begin{aligned} &conduction\ band: && E(\vec{k}) = E_g + \frac{\hbar^2 k^2}{2m_c}, && if\ \ E \geq E_g; \\ &light-hole\ band: && E(\vec{k}) = -\frac{\hbar^2 k^2}{2m_{lh}}, && if\ \ E \leq 0; \\ &heavy-hole\ band: && E(\vec{k}) = -\frac{\hbar^2 k^2}{2m_{hh}}, && if\ \ E \leq 0; \\ &split-off\ band: && E(\vec{k}) = -\Delta - \frac{\hbar^2 k^2}{2m_{so}}, && if\ \ E \leq -\Delta. \end{aligned} \tag{2.20}$$

where $E_v$ is taken to be the zero of energy. At $\vec{k}$=0, $G_c + G_v = 0$ takes a simple form

$$\frac{1}{E_B - E_g} + \frac{2}{E_B} + \frac{1}{E_B + \Delta} = 0 \qquad if\ \ E_B < E_g \tag{2.21}$$

and

$$\frac{1}{E_g - E_B^*} + \frac{2}{E_B^*} + \frac{1}{E_B^* + \Delta} = 0 \qquad if\ \ E_B > E_g \tag{2.22}$$

The case of $E_B > E_g$ does not make the Green's function go to zero because $G_c$ and $G_v$ have the same sign. Nevertheless, we will simply regard it as a empirical rule for

| Compound | Eg(eV) | Δ(eV) | $E_B$(eV) | Comment |
|---|---|---|---|---|
| Si | 1.11 | 0.044 | 0.83 | Group IV |
| Ge | 0.67 | 0.290 | 0.48 | GroupIV |
| AlAs | 2.15 | 0.29 | 1.59 | Group III-V |
| AlSb | 1.60 | 0.66 | 1.16 | Group III-V |
| GaN | 3.4 | 0.065 | 2.54 | Group III-V |
| GaP | 2.25 | 0.11 | 1.68 | Group III-V |
| GaAs | 1.43 | 0.34 | 1.05 | Group III-V |
| GaSb | 0.69 | 0.71 | 0.49 | Group III-V |
| InP | 1.28 | 0.20 | 0.94 | Group III-V |
| InAs | 0.36 | 0.44 | 0.59 | $E_B$ > Eg |
| InSb | 0.17 | 0.80 | 0.31 | $E_B$ > Eg |
| ZnSe | 2.58 | 0.50 | 1.90 | Group II-VI |
| ZnTe | 2.28 | 1.06 | 1.65 | Group II-VI |
| CdS | 2.53 | 0.135 | 1.88 | Group II-VI |
| CdSE | 1.74 | 0.52 | 1.27 | Group II-Vi |
| CgTe | 1.50 | 1.09 | 1.07 | Group II-VI |

**Table 2.1** *A list of bandgap energy $E_g$, spin-orbit splitting $\Delta$, and $E_B$ calculated using equations (2.23) and (2.24) for most common IV, III-V, and II-VI semiconductors.*

estimating some strange situations. It is easy to calculate $E_B$ (and $E_B^*$ as an empirical estimate) from the above equations

$$E_B = \frac{3(E_g - \Delta) + \sqrt{9(E_g - \Delta)^2 + 32E_g\Delta}}{8} \qquad if \;\; E_B < E_g \tag{2.23}$$

and

$$E_B^* = \frac{(3E_g - \Delta) + \sqrt{(3E_g - \Delta)^2 + 16E_g\Delta}}{4} \qquad if \;\; E_B > E_g \tag{2.24}$$

The values of $E_g$ and $\Delta$ for most semiconductors and the calculated values of $E_B$ (or $E_B^*$) using equation (2.23) and (2.24) are listed in **Table 2.1**.

The valence band discontinuity $\Delta E_v$ for any pair of semiconductors can easily be obtained by taking the difference between the two respective $E_B$'s:

$$\Delta E_v^{I,II} = E_v(I) - E_v(II) = E_B(II) - E_B(I) \tag{2.25}$$

| heterojunctions | Tersoff | Harrison | This Theory | Experiment | mismatch |
|---|---|---|---|---|---|
| AlAs/GaAs | 0.35 | 0.04 | 0.54 | 0.50[b] | 0.8% |
| ZnSe/GaAs | N.A. | 1.05 | 0.85 | 0.96[b] | 0.0% |
| Ge/ZnSe | N.A. | -1.46 | -1.42 | -1.40[a] | 0.4% |
| GaAs/Ge | N.A. | 0.41 | 0.57 | 0.56[b] | 0.4% |
| Ge/Si | -0.18 | -0.38 | -0.35 | -0.20[a] | 3.8% |
| InAs/Ge | 0.32 | 0.09 | 0.11 | 0.0[a] | 6.9% |
| InAs/GaSb | 0.43 | 0.52 | 0.10 | 0.46[b] | 1.5% |
| InP/Ge | 0.58 | 0.52 | 0.46 | 0.50[a] | 4.0% |
| CdP/Ge | N.A. | 2.00 | 1.40 | 1.85[a] | 3.6% |
| GaSb/Ge | -0.11 | -0.43 | 0.01 | 0.15[a] | 8.6% |
| GaAs/InAs | 0.20 | 0.32 | 0.46 | 0.17[b] | 6.5% |
| InSb/Ge | N.A. | -0.71 | -0.17 | 0.10[a] | 15.2% |

a. G. Margaritondo, et. al., Solid State Comm. 43, 163 (1982).

b. W.A. Harrison and J. Tersoff, J. Vac. Sci. Technol. B4, 1068 (1986).

N.A. Not available at this time.

Table 2.2 *The valence band discontinuity $\Delta E_v$ calculated by Tersoff, Harrison, and equation (2.23) and (2.24) are compared to experimental data for several common semiconductor heterosystems.*

The values of $\Delta E_v$ calculated by this method, by Tersoff's quantum dipole model, by Harrison's LCAO (Linear Combination of Atomic Orbitals) model [7], and obtained from experiments are all listed in **Table 2.2.** for comparison.

## § 2.6 Experimental data for theory testing

To assess the validity of a theory of band line-ups, it is very important to compare its predictions with the band offsets that have already been experimentally measured. Because of the technological difficulties involved in sample preparation and measurement, few data among the large number that have been published can be considered reliable enough to test theories. For example, in the case of Ge/GaAs system, the published conduction band offset $\Delta E_c$ has a range of 0.09 - 0.54 eV, indicating that there must be gross errors in some of the measurements.

In general, there are three categories of techniques:

1. *spectroscopic measurements such as infrared optical absorption and photoluminescence of a single or multiple quantum well heterostructure*
2. *electrical measurements such as I-V and C-V*
3. *photoemission measurements such as UPS and XPS*

and they suffer from some well-known difficulties. First, the spectroscopic techniques are not direct: they are sensitive to some other parameters such as effective mass $m^*$ in a quantum well, the exciton binding energy in a quantum well, and well width; unless the quantum well is thin enough they also depend on band-bending. When R. Dingle (see discussion in [9]) first used the optical absorption technique to measure $\Delta E_c$, he was actually measuring the transition energy and treating the hole effective mass as an adjustable parameter. This approach is purely adhoc and has led to the 85:15 rule for GaAs/AlGaAs ($\Delta E_c$:$\Delta E_v$ = 85:15), which was used for several years but which was found later to be incorrect by overwhelming experimental data. Second, the electrical or charge transfer techniques are also indirect in the sense that they only measure the energy difference between conduction band edge and dopant ionization energy level which is sometimes unknown (e.g., Si doping concentration in AlGaAs is still a subject of controversy), or they demand a numerical algorithm to calculate the true carrier distribution across the interface. Despite these difficulties, electrical measurements and especially photoelectric measurements [8] have achieved remarkable success recently in GaAs/AlGaAs system, and have settled down the new 60:40 rule. UPS and XPS on clean surfaces can generate very good data; however, they are difficult to perform.

### Photoelectric measurement of $\Delta E_c$

It is not possible to discuss the details of all the measurements on the GaAs/AlGaAs

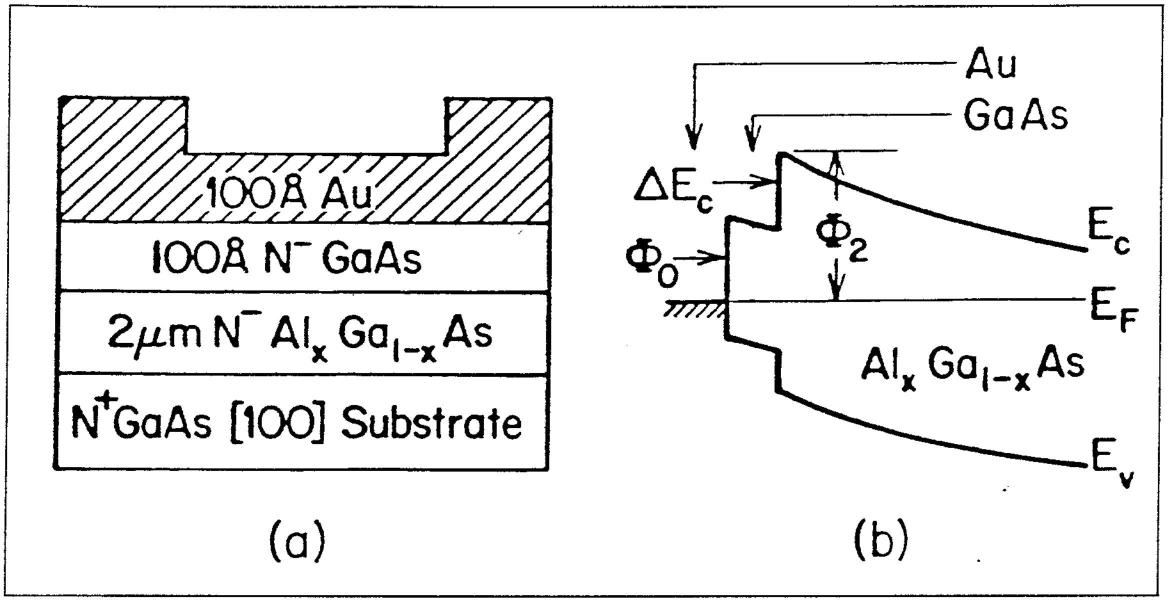

**Figure 2.3** *Schematic drawing of (a) the device structure and (b) associated energy band.*

system. Instead, a careful photoelectric measurement [8] is presented in the following. This study is motivated by the conceptual simplicity that a heterojunction can be obtained by shrinking a layer of metal between the two semiconductors.

Shown in **Figure 2.3** (a) is the device structure and (b) associated band diagram of Au/GaAs/Al$_x$Ga$_{1-x}$As hetero-Schottky barrier used in our study. The structure consists of a 100 Å Au layer, on top of a 100 Å GaAs layer which is grown on a $2\mu m$ Al$_x$Ga$_{1-x}$As layer on a [100] Si-doped ($\sim 3\text{x}10^{18}\text{cm}^{-3}$) GaAs substrate.

All the layers grown were doped nominally with Si to $\sim 2\text{x}10^{16}\text{cm}^{-3}$ to achieve a thick depletion layer. $\Phi_0, \Phi_2$ are the heights of the Au/GaAs, and Au/GaAs/Al$_x$Ga$_{1-x}$As barriers, respectively. The structure was grown at 600°C at a $1\mu m$/hour rate by MBE. Each sample was cut into two pieces: a 100 Å Au film was evaporated on one of the pieces in a vacuum of $1\times10^{-7}$ torr at a rate of 0.3-0.5Å per second; on the other, the GaAs layer was removed by 1:3:40 ($H_2O_2$ : $H_3PO_4$ : $H_2O$) then rinsed in deionized water and was blown dried. A layer of Au was subsequently evaporated on the

$Al_xGa_{1-x}As$. Thick Au dots ( ~1500Å) were deposited on top of the thin Au layer for probe contact. There was no need for the ohmic contact on the backside, since indium forms ohmic contact to the $n^+$ GaAs during the MBE growth. Au was evaporated on the backside for a better electrical contact, but no thermal annealing was performed to avoid any possible inter-atomic diffusion.

Current-voltage (I-V) characteristics were measured to confirm that these were high quality Schottky barriers. The reverse saturation current was on the order of 1nA with a reverse bias of 3~4 V for an junction area of $1.5 \times 3.5$ mm$^2$. Next, photoelectric measurements [23] were performed to determine the barrier heights $\Phi_1$ and $\Phi_2$ in the Au/$Al_xGa_{1-x}As$ and Au/GaAs/$Al_xGa_{1-x}As$ junctions respectively. A beam of light from a tungsten lamp was chopped, filtered by a spectrometer, and focused onto the Schottky contact. Photoelectric current was measured by a lock-in amplifier at room temperature. The square root of photocurrent per incident photon, was plotted against h$\nu$, and the intercept at zero photocurrent was taken as the barrier height. Image force lowering ($\approx$ 0.04eV) in the Au/GaAs/$Al_xGa_{1-x}As$ structure reduces the heterojunction interface band-bending ($\approx$ 0.04eV) , therefore errors due to band-bending were small ($\leq$ 0.01eV). Since the sample is lightly doped and has a wide depletion region, quantum mechanical tunneling is negligible. The aluminum concentration was determined from a photoluminescence measurement of the direct bandgap $E_g$(x), and from the measured growth rate. Both methods were in good agreement ($\Delta x \leq 0.01$). The Au/GaAs barrier height $\Phi_0$ was determined separately on Au/GaAs junctions with the same doping resulting in a value of 0.89eV. This value was then subtracted from $\Phi_1$ and $\Phi_2$, separately, to determine the conduction band offset $\Delta E_c$ of GaAs/$Al_xGa_{1-x}As$ heterojunction. The results for both cases are given in **Table 2.3**. As can be seen in **Table 2.3**, $\Delta E_c$ and $\Delta E_c/\Delta E_g$ ratios determined from $\Phi_1 - \Phi_0$ and $\Phi_2 - \Phi_0$ are the same for aluminum mole fraction $x \leq 0.3$, but different above this value. The discrepancy between the conduction band discontinuity $\Delta E_c$ and the difference of barrier heights $\Phi_1$ - $\Phi_0$ seems to increase linearly in aluminum composition. This is in relatively good agreement with the recent measurements [12,13,14,15,16,19] and the deformation potential theory [24]. We attribute the lowering of $\Delta E_c = \Phi_1 - \Phi_0$, and $\Phi_2 - \Phi_0$, to the influence of the L and X bands at higher aluminum mole fractions. An GaAs/Al$_x$Ga$_{1-x}$As structure with a heterojunction is expected to have more strain, and at higher aluminum mole fractions lattice and thermal mismatch-induced strain effects lower the Al$_x$Ga$_{1-x}$As conduction band offset [16]. Measured Au/Al$_x$Ga$_{1-x}$As barrier heights listed in **Table 2.3** are slightly higher than those obtained previously [25] using liquid phase epitaxy samples. The ratio of $\Phi_1/E_g$ is $\approx$ 63%, close to the $2/3E_g$ empirical law value [26].

Finally, we plot the conduction band discontinuity $\Delta E_c = \Phi_2$ - $\Phi_0$, against $\Phi_1$ - $\Phi_0$ using data in **Table 2.3** in **Figure 2.4**(a). As can be seen, for aluminum mole fraction $x \leq 0.3$, $\Delta E_c = \Phi_1 - \Phi_0$, for x above 0.3, the agreement is less certain. This implies that in a double Schottky barrier such as illustrated in **Figure 2.4**(b), the band-bending on either side of the Au layer is independent of the gold thickness and we can consequently think of the band offset $\Delta E_c$ as the value of $\Phi_1 - \Phi_0$ in the limit of zero gold thickness, for small aluminum mole fractions $x \leq 0.3$. It also confirms the predicted quasi-linear correlation by Tersoff [4] and Margritondo [22] for small aluminum mole fractions and suggests a relatively large discrepancy for large aluminum mole fractions. Our study does not imply however, that this result can be applied to any metal.

Without commenting on the details of their measurements, we cite a few heterojunction system measurements [9] considered reliable by H. Kroemer, who is an authority on this.

1. *GaAs/AlGaAs system.* This is the most heavily studied system thus far. All the measurements now are converging onto the 60:40 rule. It has been widely agreed that the valence band discontinuity is

| $X$ | 0.15 | 0.30 | 0.44 | 0.48 |
|---|---|---|---|---|
| $\Phi_1$ | 1.02±0.01 | 1.13±0.02 | 1.23±0.02 | 1.27±0.02 |
| $\Phi_2$ | 1.02±0.01 | 1.12±0.02 | 1.22±0.02 | 1.24±0.02 |
| $\Delta E_c{}^a$ | 0.13±0.01 | 0.24±0.02 | 0.34±0.02 | 0.38±0.02 |
| $\Delta E_c{}^b$ | 0.13±0.01 | 0.23±0.02 | 0.33±0.02 | 0.35±0.02 |
| $\frac{\Delta E_c{}^a}{\Delta E_g}$ | 0.69±0.05 | 0.64±0.05 | 0.62±0.05 | 0.63±0.05 |
| $\frac{\Delta E_c{}^b}{\Delta E_g}$ | 0.69±0.05 | 0.61±0.05 | 0.60±0.05 | 0.58±0.05 |

*a:* $\Delta E_c = \Phi_1 - \Phi_0$ *b:* $\Delta E_c = \Phi_2 - \Phi_0$

**Table 2.3** *The conduction band discontinuity $\Delta E_c$ obtained from Schottky barrier heights for different aluminum mole fractions.*

$\Delta E_v$[AlAs/GaAs]=0.50eV

2. *Ge/ZnSe, ZnSe/GaAs, and GaAs/Ge.* These three pairs provide a test of transitivity, i.e.,

$$\Delta E_v[A \rightarrow B] + \Delta E_v[B \rightarrow C] + \Delta E_v[C \rightarrow A] = 0$$

substituting in the experimental data obtained by different people, we actually get

$$\Delta E_v[Ge \rightarrow ZnSe] + \Delta E_v[ZnSe \rightarrow GaAs] + \Delta E_v[GaAs \rightarrow Ge] = 0$$

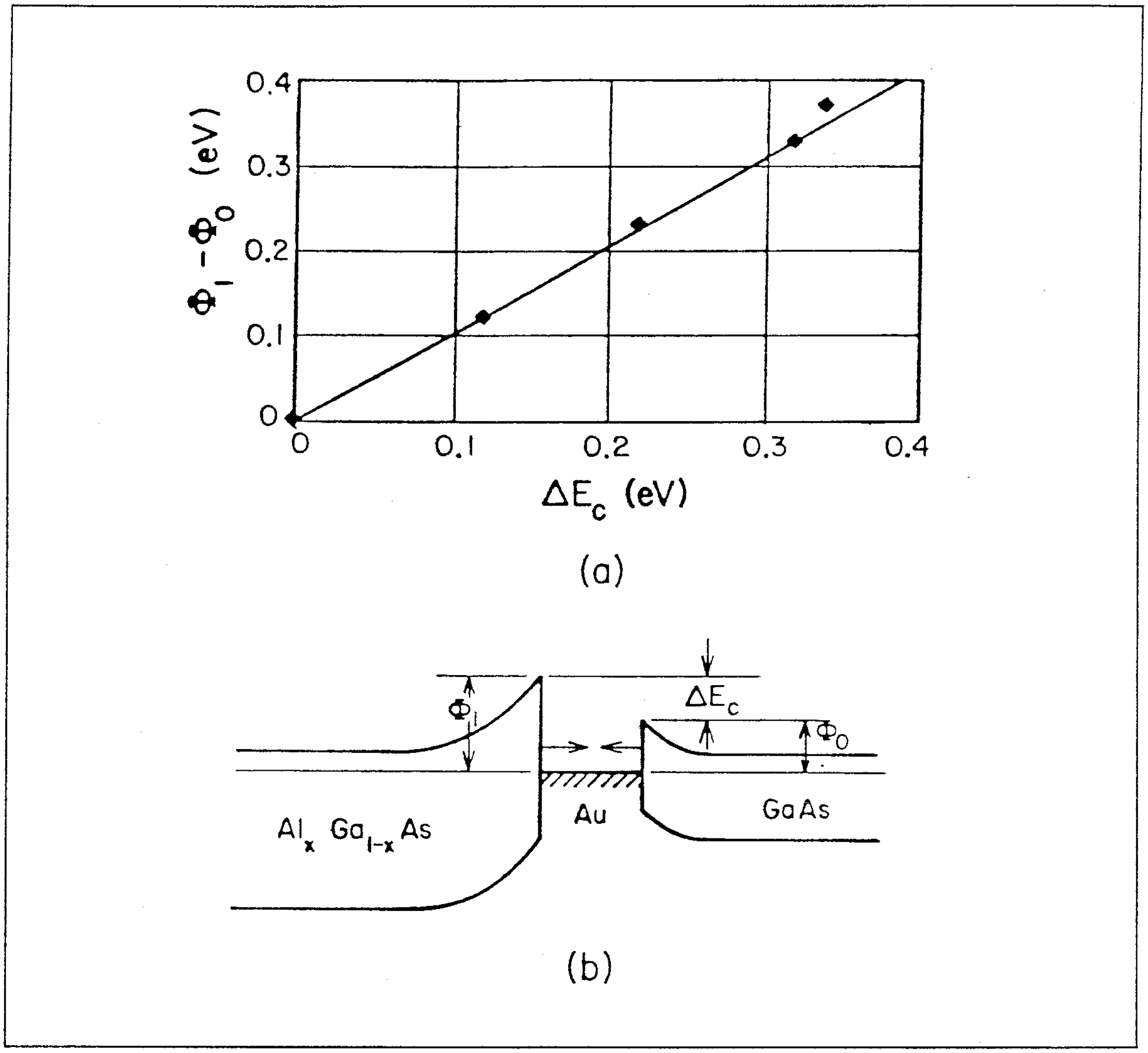

**Figure 2.4** *(a) The conduction band offset $\Delta E_c$ can be obtained by $\Phi_1$ - $\Phi_0$, and (b) the two energy bands can be properly aligned by shrinking the thickness of gold in between.*

3. *InAs/GaSb system.* This is a very unusual line-up, the conduction band edge of InAs is above 150meV below the valence band edge of GaSb, an example of broken-gap line-up. The available experimental data seem to indicate that

   $\Delta E_v[InAs/GaSb] = 0.51\text{eV}.$

The above five heterosystems together can verify the validity of a band line-up theory since they include group IV, III-V, and II-VI elements all together. The newly proposed theory presented earlier, performs very well under these tests. Notice that GaAs/AlAs is the most reliable system today and the only one whose numerical band offset has been experimentally determined beyond any doubt. The experiment value of 0.50eV is very close to my calculated value of 0.54eV. Even the recent Tersoff theory does not meet this test: it predicts a value of 0.35eV. As in **Table 2.2**, the proposed theory also works very well with other experimental data collected so far.

The only exception is for InAs/GaSb system. A possible reason is the following: First, InAs/GaSb has a lattice constant mismatch of 8%. Whenever there is a large lattice mismatch, the line of reasoning we have followed so far, which assumes a perfect termination of a infinite lattice, will fail. Green's function calculation can not be performed since we do not know the potential near the interface caused by lattice mismatch, and we do not know how to expand the inverse Hamiltonian (Green's operator). Second, it maybe similar to the history of the GaAs/AlAs system, which was first believed to have almost a zero valence band offset (85:15 rule) that was changed later, and therefore the current experimental data may not be reliable. More careful measurements will clarify this issue and ascertain the value of experimental band line-up of InAs/GaSb system.

## § 2.7 Conclusions

In this chapter, we have given Tersoff's quantum dipole theory a theoretical basis using Green's function technique, since the wavefunction matching can be done by a secular equation of Green's functions on the interface. It is further noticed that the secular equation when spatially averaged, gives rise to the Tersoff model previously based only on some qualitative physical arguments. Furthermore, we have imposed a $\vec{k}$-selection rule on the Tersoff theory, and successfully applied it to the $\Gamma$ point ($\vec{k}$ $=0$) to eliminate the uncertainty of Tersoff's model due to the dependence on $\vec{R}$. This simplified theory works better than the Tersoff theory when compared with experiments, especially; it predicts the band offset of AlAs/GaAs system correctly. A photoelectric measurement is made on both the Schottky barrier height of Au/AlGaAs and the conduction band offset $\Delta E_c$ between GaAs and AlGaAs as a function of aluminum mole fraction $x$.

## § 2.8 References

[1] T. Lukes, *Solid State Theory*, ed. P. T. Landsberg, John Wiley & Sons, London, 1969, part F, and references therein.

[2] F. Flores, Nuovo Cimento, **14B**, 11(1973).

[3] F. Garcia-Moliner and J. Rubio, J. Phys. C (Solid State), **2**, 1789(1969).

[4] J. Tersoff, Phys. Rev. , **B30**, 4874(1984) ,Phys. Rev. **B32**, 6968 (1985).

[5] W. A. Harrison, J. Vac. Sci. Technol. , **B3(4)**, 1231(1985).

[6] E. O. Kane, J. Phys. Chem. Solids, **1**, 83(1956).

[7] W. A. Harrison, J. Vac. Sci. Technol. , **14**, 1016(1977).

[8] H. Z. Chen, H. Wang, A. Ghaffari, H. Morkoç, and A. Yariv, Appl. Phys. Lett. , **51**, 990(1987), and references therein.

[9] H. Kroemer, *VLSI Electronics: Microstructure Science*, **10**, 121(1985).

[10] R. Dingle, Advances in Solid-State Physics, H. J. Queisser, ed. , **15**, 21 (1975).

[11] H. Kroemer, J. Vac. Sci. Technol. , **B2**, 433 (1984).

[12] D. Arnold, A. Ketterson, T. Henderson, J. Klem, and H. Morkoç, J. Appl. Phys. **57**, 2880 (1985).

[13] T. W. Hickmott, P. M. Solomon, R. Fischer and H. Morkoç, J. Appl. Phys. **58**, 2853 (1985).

[14] J. Batey, S. L. Wright, and D. J. DiMaria., J. Appl. Phys. **58**, 484 (1985).

[15] W. I. Wang and F. Stern, J. Vac. Sci. Technol. **B3**, 1280 (1985).

[16] M. A. Haase, M. A. Emanuel, S. C. Smith, J. J. Coleman, and G. E. Stillman, Appl. Phys. Lett. **50**, 404 (1987).

[17] C. A. Mead, Solid-State Electon. **9**, 1023 (1966).

[18] W. Mönch, Surf. Sci. **132**, 92 (1983).

[19] H. Kroemer, Conference Workbook of 2nd International Conference on Modulated Semiconductor Structures, Sept. 9-13, Kyoto, Japan, 1985, Supplement p. 797.

20] W. A. Harrison and J. Tersoff, J. Vac. Sci. Technol. **B4**, 1068 (1986).

21] H. Hasegawa and H. Ohno, J. Vac. Sci. Technol. **B4**, 1130 (1986), Jpn. J. Appl. Phys. 25, L265 (1986).

22] G. Margaritondo, Surf. Sci. **168**, 439 (1986).

23] C. R. Crowell, W. G. Spitzer, L. E. Howarth, and E. E. LaBate, Phys. Rev. **127**, 2006 (1962).

4] H. Unlu and H. Morkoç, Bull. of American Physical Society **32**, No. 3, (1987).

5] J. S. Best, Appl. Phys. Lett. **34**, 522 (1979).

6] C. A. Mead and W. G. Spitzer, Phys. Rev. **134**, A713 (1964).

# Chapter 3

## MBE Growth of GaAs-on-GaAs Quantum Well Lasers

### § 3.1 An introduction

In this chapter, techniques to optimize crystal growth in an MBE system and our basic understanding of how a quantum well laser operates are combined as we try to grow low-threshold quantum well lasers. Details of MBE growth of GaAs/AlGaAs quantum well lasers on GaAs substrate (the work on Si is discussed in the next two chapters) are presented. The main purpose of this chapter is to discuss various useful techniques (dirty tricks) used in MBE growth that were developed in this research and eventually enabled us to grow the lowest threshold lasers in the world. Emphasis is made on how to experimentally optimize growth conditions and minimize the effect of minor instrument failures. Results obtained from quantum well lasers are also analyzed to provide a simple experimental procedure for growing low-threshold lasers. Topics such as the basic growth processes, mathematical models for the growth, etc., have been thoroughly covered by many authors in many excellent articles [1], and will not be discussed here.

## § 3.2 Substrate preparation

It is self-evident for any materials scientist that a clean substrate is the single most important thing for any epitaxial growth. Contaminated substrates can lead to mistakes that are regrettable. Not long ago, the most common macroscopic defects on (100) GaAs layers grown by MBE, the "oval defects," were attributed to the effect of Ga "spitting" from the Ga effusion cell. Condensed Ga at the orifice of the Ga crucible can roll back, splash into the Ga melt, and cause eruption and ejection of Ga droplets, and were believed to form "oval defects." Therefore, many users of MBE kept the Ga crucible filled as close to the orifice as possible, or provided additional heating to Ga to eliminate "oval defects." But their success was very limited. More careful investigations by many groups have now revealed that the "oval defects" are *not* at all related to any Ga "spitting." Instead, gallium oxide in the melt, and *especially* carbon on the GaAs substrate surface are the true causes of this defect [2]. A good cleaning procedure would have prevented all these unnecessary troubles.

### Cleaning procedure

The procedure we have been using is the same one used by Morkoç group at the University of Illinois, and it is shown in **Appendix II.**

### Substrate mounting

At this point, we have a clean GaAs substrate with perhaps a very thin layer of some unknown compound (a few atomic layers, and the layer is so thin that a clear RHEED pattern from the sample inside the MBE growth chamber can be observed without heating the substrate). We should immediately transfer the substrate to a clean fume hood where it can be In-mounted to a Mo block. Since the mounting is done at 250°C, a thin layer of oxide is grown as a result of the reaction of GaAs with oxygen in air (**Figure 3.1**). A common misconception is that this protective oxide layer is grown in the last water rinsing. The substrate after the chemical cleaning can be recontaminated by dirty air in the room. A protective thin oxide layer has to be grown in the air inside a clean fume hood in a clean room. Furthermore, this layer blocks RHEED pattern below 580°C and provides the *only* reliable calibration of substrate temperature for GaAs substrate (oxide on GaAs desorbes at 580°C). A GaAs substrate directly mounted (see Chapter 6 for Si substrate mounting) on a Mo block without use of In, does not have this thermally grown oxide layer, and consequently a RHEED pattern can be observed even at room temperature (the solution of course, is to put the mounted substrate in a heated oven to grow this oxide layer). The In mounted substrate is now safe, and it can wait for some time to be loaded into MBE, although it should be done as quickly as possible.

## § 3.3 Growth of GaAs/AlGaAs quantum well lasers

Most of the lasers used in this thesis research employ a graded refractive index separate confinement heterostructure (GRINSCH) single quantum well (SQW) structure. The details of the growth are described in the following.

### Pregrowth preparation of MBE

After the substrate is mounted on a Mo block and loaded into the MBE system, it is first heated to 300°C in the loading chamber (first of the three chambers) to remove any water vapor condensed on it. The pressure in the loading chamber may briefly rise, but it will come down quickly. Then the substrate is transferred to the analysis chamber where the vacuum is about two orders of magnitude higher than that in the loading chamber. After waiting for some time until the pressure is as low as before, the substrate is transferred to the growth chamber.

At this time, the growth chamber, which contains a liquid nitrogen cooled shroud surrounding it, has reached a high vacuum of about $5 \times 10^{-9}$ torr or lower. When the base pressure in the growth chamber goes down to $10^{-9}$ torr, the outgasing of all the

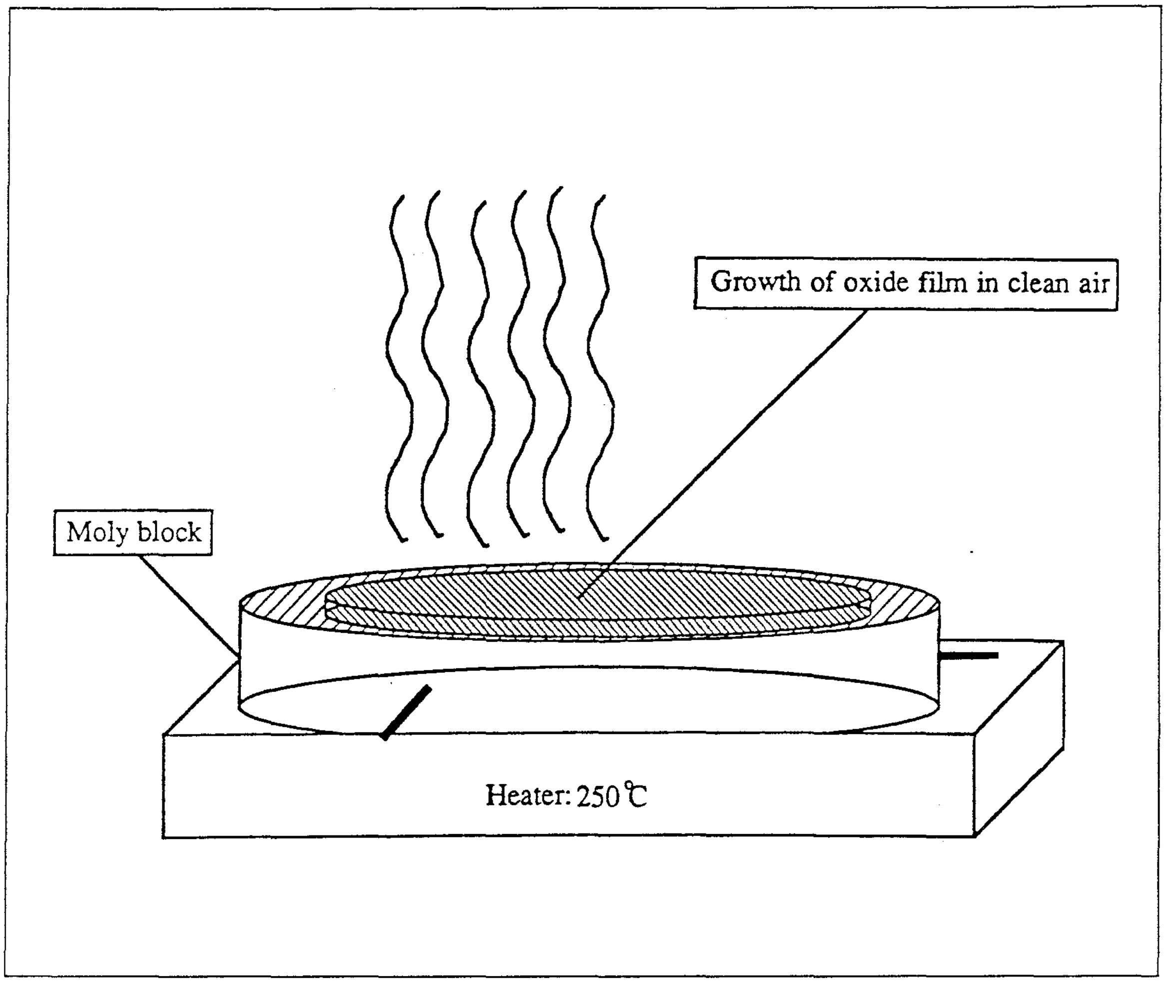

**Figure 3.1** *Thermal growth of a thin protective oxide film in clean air.*

source materials in effusion cells to be used in growth should be started. This is done by heating the cells to a temperature slightly higher than the growth temperature to blow off any condensations accumulated on the surface of source materials. The arsenic cell is heated up very slowly because any excess heating can result in large amount of arsenic loss, so it should be started with shroud cooling at the same time. When all the materials have been outgased and reset to their growth temperatures (from here on we use a computer program to control their temperatures), and the As cell has reached its set temperature, we can start the growth procedure.

## Thermal cleaning of GaAs substrate

The temperature of the GaAs substrate is controlled manually by a power supply. At each increase of heating power, both current $I$ and voltage $V$ going into heating filaments under the Mo block are recorded. The power $P = IV$ is increased when the thermal couple reading stops rising (usually this takes a few minutes with In-mounted substrate, and a few seconds with In-free mounting). When the heating power reaches a certain level (this has to be based on previous growth records and is usually when the substrate temperature is about 500°C), the RHEED instrument and pyrometer are turned on to start monitoring the substrate surface. At about 580°C, the (2×4) and C(2×8) surface reconstruction patterns appear clearly on the RHEED screen, which indicates the desorption of the thin oxide layer. A brief temperature increase is used to assure the complete desorption of oxide. The As shutter is opened at the same time to prevent any loss of As atoms from the GaAs substrate. When the RHEED pattern becomes sharp, an atomically clean surface is obtained and ready for growth.

## RHEED pattern and surface reconstruction

A RHEED pattern appears when the substrate surface becomes clean. The identification of a RHEED pattern requires knowledge of the surface reconstructions. The following notations are often used [3]:

1. *GaAs (100) - (m×n) means that a GaAs crystal is orientated with the (100) direction normal to the surface, and has a surface structure whose unit mesh is m×n times larger than the underlying bulk unit cell.*
2. *If the mesh is centered, the notation would be GaAs (100) - C(m×n). If the mesh is rotated, the notation would be specified by the angle of rotation, e.g., GaAs (111) -* $(\sqrt{19} \times \sqrt{19})R23.4^\circ$*. If the surface reconstruction is an As-stabilized surface, we denote it by, e.g., GaAs (100) - C(4×2)As. GaAs (100) - C(4×2)Ga is likewise used for an Ga-stabilized surface.*

As an example, **Figure 3.2** shows two of the most commonly observed surface structures, (2×4) and C(2×8), in real and reciprocal space. Experimentally, it has been known that [4] surface structures depend on three things: the background pressure, whether the substrate is cooling down or heating up, and the temperature at which the substrate is cooling down or heating up. For our laser growth, the substrate is heating up, at 580°C, in a pressure of about $1\times10^{-7}$Torr in an As-rich environment. According to Cho [4], for a GaAs (100), (2×4)As(Ga) and C(2×8)As(Ga) reconstruction patterns should be observed under normal growth conditions. It is very difficult to distinguish these two patterns. The reason is illustrated in **Figure 3.3** which shows reciprocal lattice sections for both (2×4) and C(2×8) and their expected RHEED patterns in different azimuthal angles. For all practical purposes, one should rotate the substrate manually and observe all the above patterns as a sign of a clean GaAs (100) surface, just after the oxide protection layer is desorbed at 580°C.

### $As_2$ pressure

It is known [1] that $As_2$ molecules (not $As_4$) are responsible for the MBE growth of GaAs. Arsenic molecules from a standard Knudsen cell are predominantly $As_4$. A subsequent "cracking" of $As_4$ which occurs when they arrive at GaAs surface, produces $As_2$ molecules which participate in GaAs growth. In practice, a $P_{As_4} = 10^{-7}$ torr is needed from a conventional $As_4$ cell that has no cracking effect at all and a $P_{As_2} = 10^{-8}$ torr is needed from an arsenic cracker cell that has a high cracking-efficiency of about 90%. Arsenic pressure below this level will produce Ga-stabilized growth, which is inconsistent with the As-terminated (100) substrate used.

### GaAs buffer layer

When the oxide layer is desorbed, the substrate temperature is usually at 620-640°C which is slightly higher than what is optimum. Therefore, we lower the temperature to about 580-600°C and start the growth by opening the Ga shutter and desired dopants.

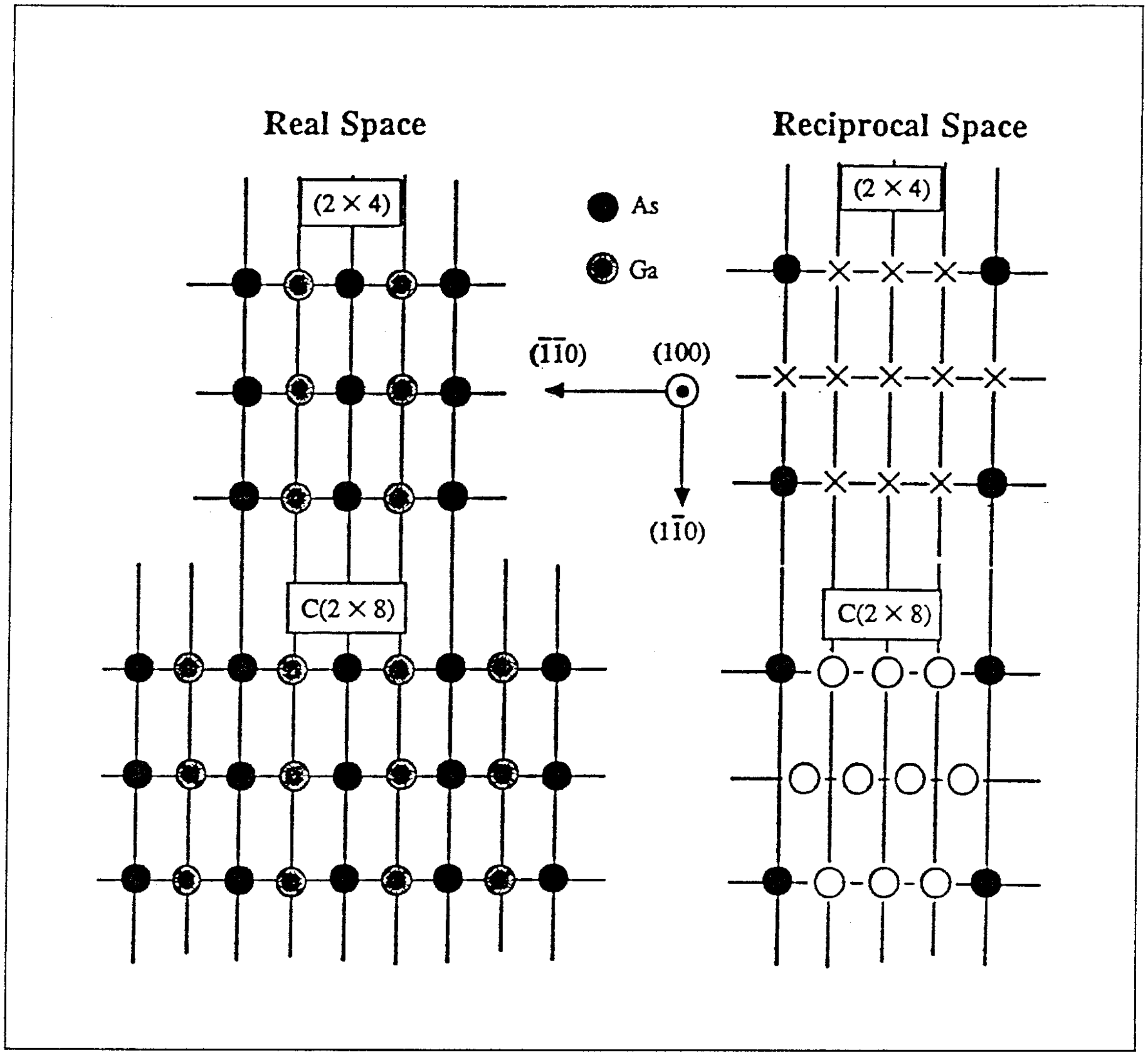

**Figure 3.2** *The (2 × 4) and C(2 × 8) surface structures in real and reciprocal space.*

Since we usually use $n^+$ GaAs substrates, Ga and Si shutters are opened. At the opening of Ga shutter, a sudden drop of total pressure is observed on the ion gauge indicating Ga atoms are combining with As atoms.

A few minutes into the growth the RHEED pattern should be checked again. A good start of the growth usually shows sharp and streaky lines in RHEED patterns which indicate a typical two-dimensional surface reconstruction.

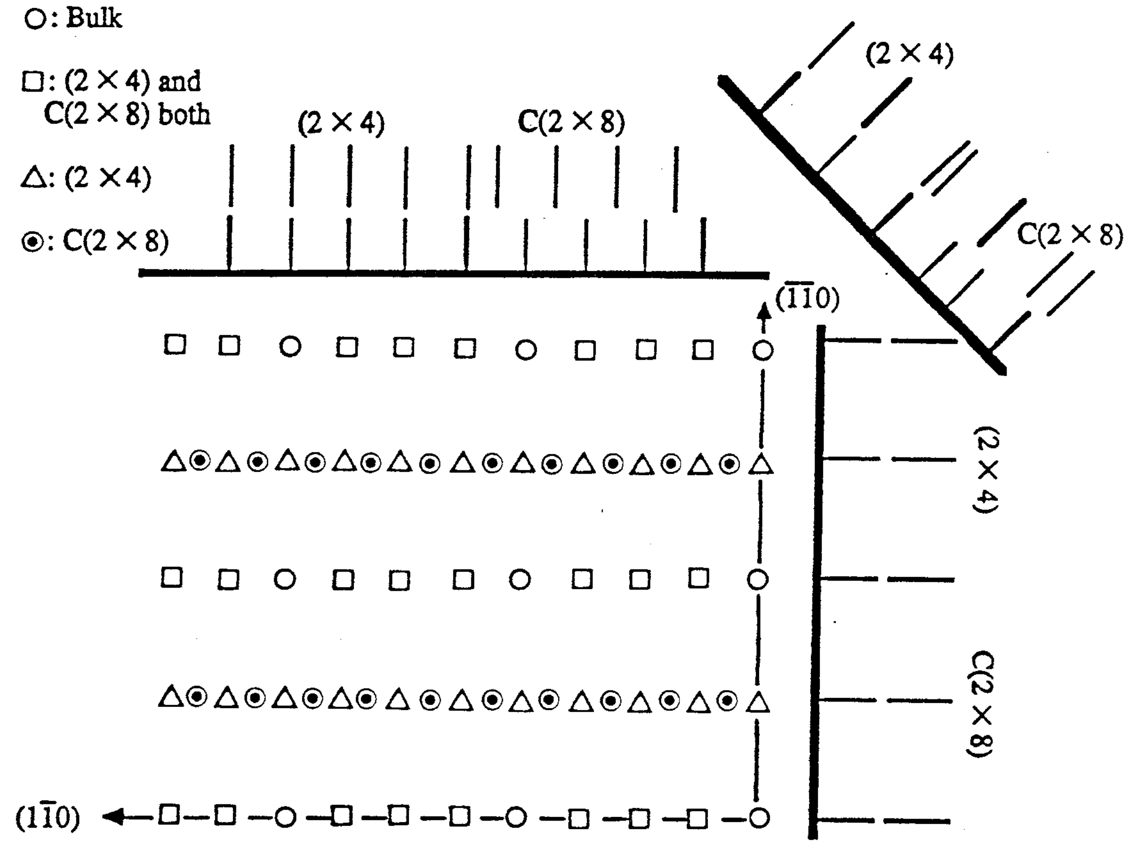

**Figure 3.3** *The (2 x 4) and C(2 x 8) surface structures in reciprocal space and the associated RHEED patterns in different azimuth in real space.*

The GaAs buffer layer growth takes about an hour before the growth of AlGaAs is started. Some believe that a thicker buffer layer will improve the quality of later AlGaAs growth since AlGaAs will be farther away from the first interface where there might be some defects and/or impurities. However, there has been no convincing evidence. The best lasers that we have grown have a 1.5$\mu$m GaAs buffer layer. Thicker buffer layers have not resulted in any noticeable improvement in this study. This is because inside an

MBE's growth chamber, everything reaches thermal equilibrium quickly. Furthermore, the residual impurities can not be removed by one more hour of growth anyway.

The As cell temperature should be kept low as long as the growth is still in an As-stabilized environment (which can be observed on the RHEED screen).

Some researchers believe that the use of a superlattice region in the buffer layer will improve the quality of growth. This is simply a misunderstanding of the dynamic nature of an MBE growth. Although the use of a superlattice may temporarily trap some impurities and stop defects from propagating for the time being, as soon as the superlattice is finished, the growth returns to its previous condition quickly. The correct moment to use a superlattice is just *before* the quantum well growth, to smooth the interface and stop impurities and defects. Such is the case of our laser growth where 5 quantum wells have been used just before the active quantum well, to smooth the interface and prepare it for the next quantum well growth [5].

### AlGaAs cladding layer

Near the end of the GaAs buffer layer and when the growth approaches the beginning of the AlGaAs cladding layer, the As cell temperature is raised by 2 degrees to raise the As pressure since the growth rate of AlGaAs is normally $1.5\mu m/h$, compared to $1.0\mu m/h$ for GaAs, and consumes more As. At the moment the Al shutter opens, the substrate temperature is suddenly raised to 720°C by increasing the heating power. From our experience over several hundred growths, $P = 110W$ for low temperature ($\approx 600°C$) and $P = 225W$ for high temperature ($\approx 720°C$) should be used. This is very important since high substrate temperature can improve the optical quality of AlGaAs dramatically [6], while the low temperature growth gives best crystal uniformity and electrical properties. The two keys to a high quality AlGaAs growth are (a) high substrate temperature, and (b) minimum As to Ga ratio [6]. The substrate temperature throughout the entire growth of a GRINSCH laser is shown in **Figure 3.4.**

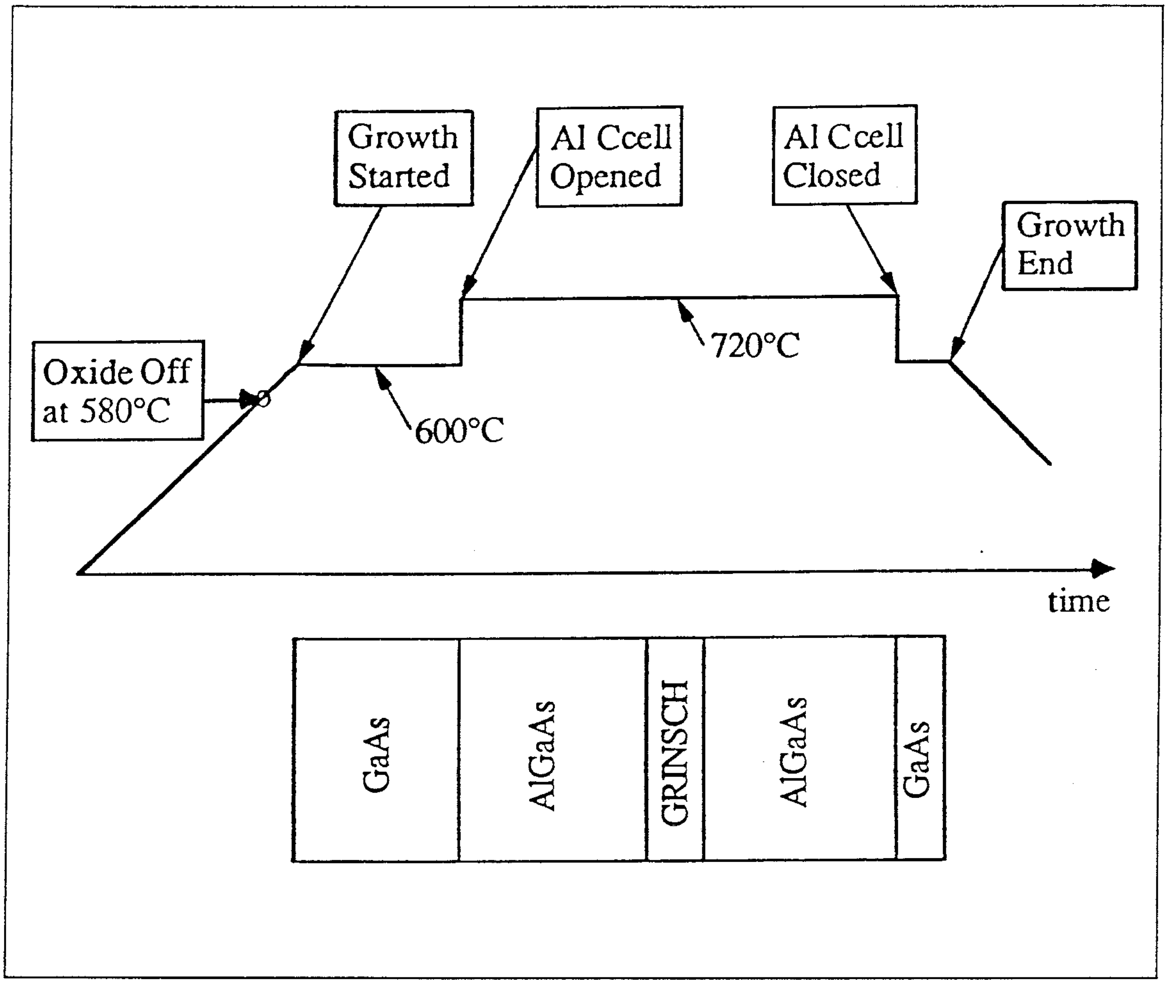

**Figure 3.4** *The temperature profile for an entire laser growth.*

## Laser structure

After 1.5$\mu$m of AlGaAs cladding layer growth, the growth of the GRIN region starts. The refractive index can be changed by varying the Al mole fraction according to a prewritten computer program, to create a parabolic-like optical waveguide. The control parameters of the Al cell temperature regulator have to be set so that it can respond as quickly as possible to the temperature setting commands. The Si cell temperature is reduced gradually for a doping level from $1.0\times10^{18}\text{cm}^{-3}$ in AlGaAs outside the GRIN, down to $1.0\times10^{17}\text{cm}^{-3}$ when it is closed just before the quantum well. Three to five

5Å wide smoothing quantum wells 1000 Å away from the active quantum well are grown to improve surface quality. The Si shutter is closed about 100 Å away from the quantum well since Si atoms diffuse in AlGaAs. The Be shutter is opened after the quantum well is grown, and its temperature is gradually raised for a doping level from $1.0\times10^{17}\mathrm{cm}^{-3}$ up to $1.0\times10^{18}\mathrm{cm}^{-3}$, while the Al mole fraction is increased to form the second half of GRIN. **Figure 3.5** shows the above structure schematically.

The upper 1.5$\mu$m of AlGaAs cladding layer was grown after this, followed by a p-GaAs capping layer doped by Be to $5.0\times10^{19}\mathrm{cm}^{-3}$. The substrate temperature of the last GaAs layer growth is dropped abruptly to 600°C.

## Al profile: a technological issue

Ever since the first GRINSCH laser, it has been assumed that a parabolic GRINSCH structure is fundamentally superior [7]. From a simple analysis, however, the profile of the Al concentration does not appear important. A carefully designed variation in Al mole fraction creates an optical waveguide that greatly reduces light scattering losses. The exact shape of this index waveguide, though, is not important, nor is it possible to obtain due to random fluctuations of Al effusion cell. As long as the waveguide has a lateral dimension that is comparable to the size of fundamental optical mode, its purpose is well served. Different waveguide shapes which are created either intentionally or unintentionally by fluctuations of Al cell from time to time should give different threshold current, yet no sign of such effect has ever been reported. What has been consistently observed, however, is that the threshold current is always low when an MBE system is clean and working well, regardless the shape of the waveguide; and when the MBE is not working well, no structure can achieve a low-threshold current. Therefore, there seems to be a discrepancy between our analysis and the experiment. The answer, as is always the case, lies in the technological aspect of growth. It has been well established experimentally that the growth of an “inverted” GaAs (GaAs

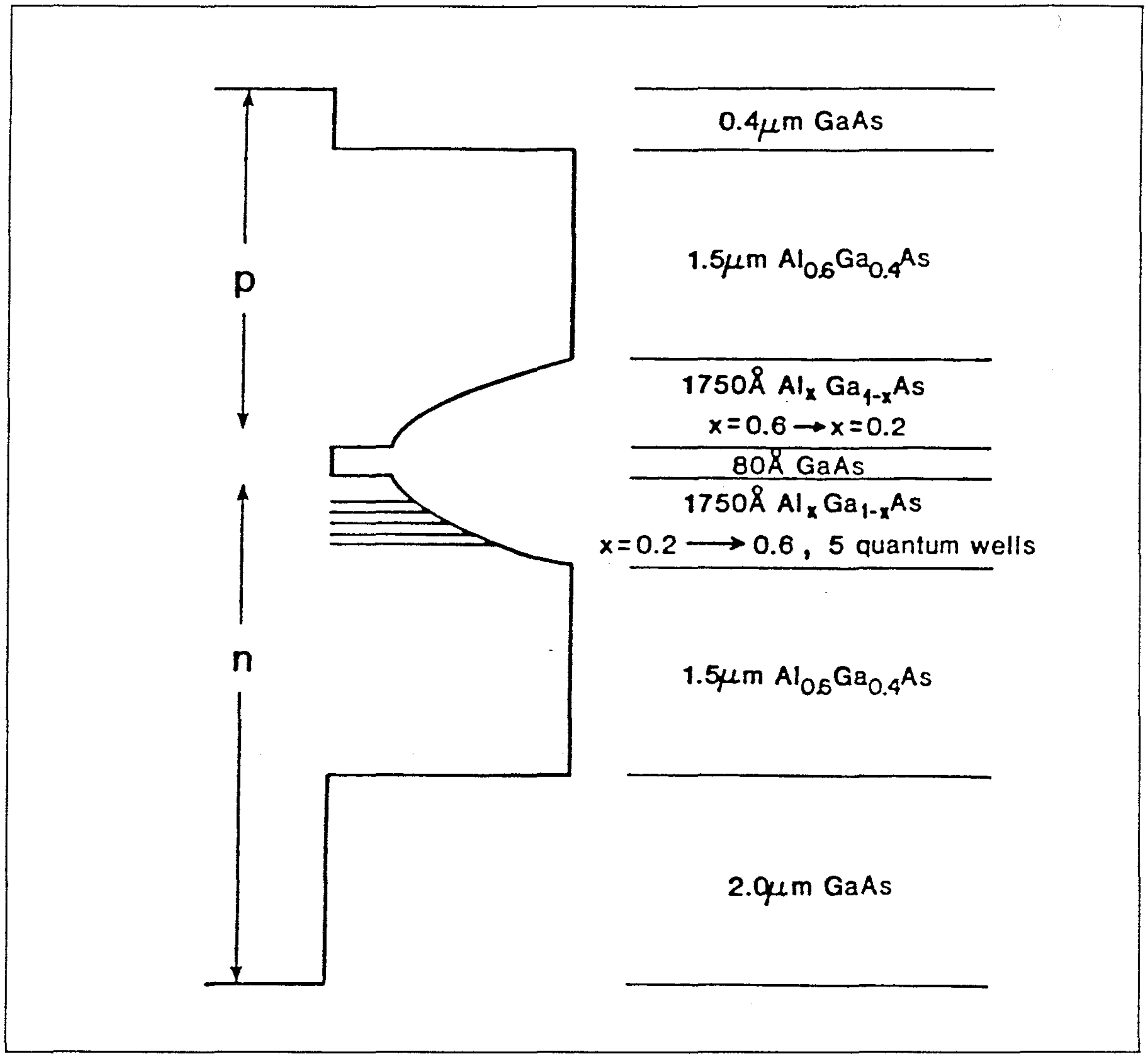

**Figure 3.5** *Schematic drawing of the conduction band edge of a GRINSCH laser.*

on AlGaAs) is often of poor quality [8]. The higher the Al concentration in AlGaAs, the poorer GaAs on it. Therefore, it is possible that a GRINSCH laser has a better GaAs quantum well since the Al concentration is gradually reduced, giving the surface enough time to reconstruct. Moreover, if one simply grows a step index waveguide (**Figure** 3.6) where the Al mole fraction is changed abruptly, the quality of the "inverted" GaAs quantum well is not good. Clearly, the difference between a GRINSCH

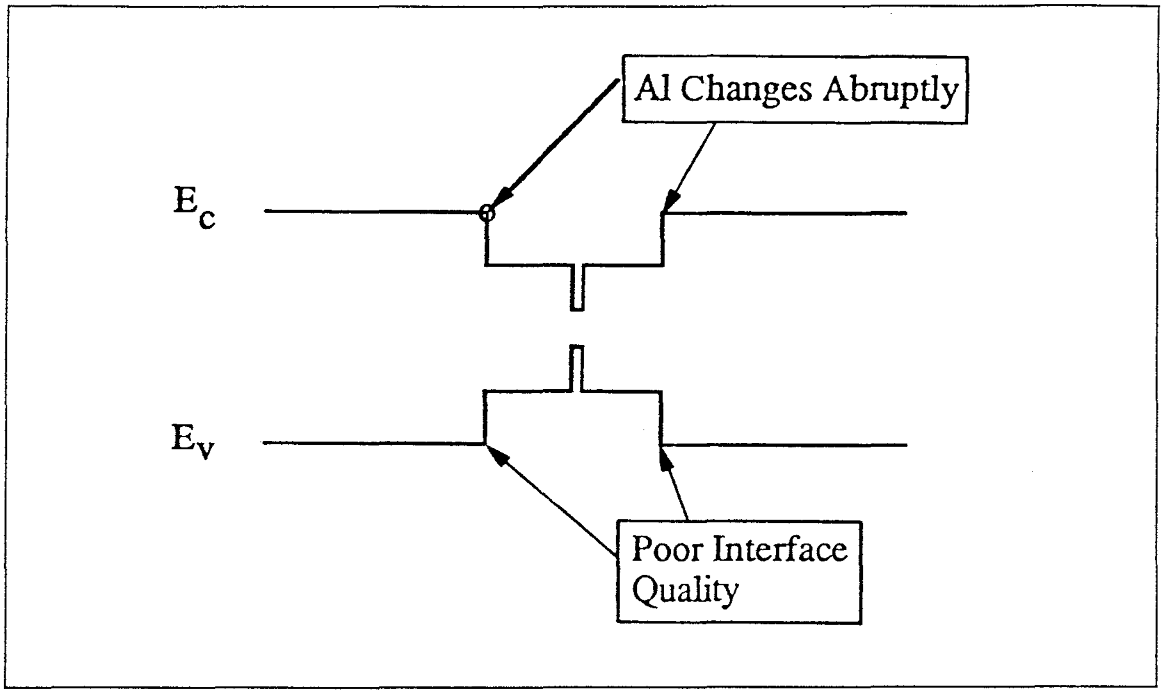

**Figure 3.6** *The band edge diagram of a step-indexed laser. The abrupt aluminum mole fraction changes result in a poor MBE growth of the following layer.*

and a step-index laser is mainly technological. Once the technological difference is eliminated, the two should produce similar results. This, has been recently confirmed by a distinguished Russian research group at Leningrad Institute led by Dr. Garbusov [9], totally unaware of our record threshold current density of 80 A/cm$^2$. They have succeeded using the very difficult LPE technique, to grow a step-index single quantum well (100 Å) laser and obtained a threshold current density of 98 A/cm$^2$. Their result confirms the above analysis very convincingly.

### Technique of growth interruption

It has become increasingly popular in the MBE community to apply growth interruption techniques to improve interface quality. The purpose of a growth interruption is to allow the ongoing interface to relax (or to reconstruct) following a change in atomic composition (such as Al grading in AlGaAs). Such a technique can improve the quality of "inverted" GaAs on AlGaAs. The procedure for the (Ga,Al)As system is shown in **Appendix III.**

This technique has been used in the GaAs-on-Si growth, and it improves the surface morphology noticeably.

## § 3.4 Fabrication and measurement of broad area lasers

### Fabrication

Each time a sample is grown, measurements are performed to obtain the threshold current density, $J_{th}$, and the lasing wavelength $\lambda$. A low-threshold current density is very important since it is a universally accepted measure of MBE growth quality: the lower the threshold, the better the crystal growth. The fabrication procedure of broad area lasers is shown in **Appendix IV.**

### Measurement of threshold current density

The measurement of threshold current of a broad area laser device is done with a pulsed power supply since continuous wave (CW) operation is impossible without mounting the laser upside down on a heat sink. Typical current pulses are 100 ns wide and are at a 50 kHz rate. The laser diode is forward biased in front of a Si p-i-n photodiode. The pumping current signal (converted to voltage by a current probe) and p-i-n diode signal are fed into an oscilloscope. Light power vs. pumping current is plotted for the laser until well above threshold. The intercept of the linear portion of the $L-I$ curve with current axis is the threshold current $I_{th}$, which is then divided by the surface area ( measured by an optical microscope ) of the laser to obtain $J_{th}$. The slope of the $L-I$ curve gives the quantum efficiency: $\eta = slope(W/A)/E_g$.

The measurement of lasing wavelength is done with an optical fiber bundle replacing the p-i-n detector to collect light from the laser, which is then fed into a monochrometer and collected by an optical signal multichannel analyzer which displays 90 - 100 Å of the entire spectrum of the optical signal. When the laser is biased just below threshold, a large number of Fabry-Perot cavity modes are visible on the analyzer (**Figure 3.7**). At threshold, one such cavity mode spikes up suddenly atop the spontaneous emission background. The lasing wavelength and the threshold current can thus be determined simultaneously. This threshold is then compared with the value obtained form $L-I$ measurement. The spectrum measurement often gives a threshold value slightly higher than given by the $L-I$ method and is believed to be more reliable.

## § 3.5 The effect of substrate misorientations

The previous discussions do not involve the type of substrate used in the MBE growth. In practice, however, they do make a significant difference. The various crystal orientations are shown in **Figure 3.8**.

The surface of a commercially available substrate is not atomically flat. It contains microscopic steps that expose mini-surfaces along different orientations. For example, on a primarily (100) oriented substrate, there exist (111)Ga, (111)As, (211)Ga, etc., mini-surfaces, although most surface area is covered by (100) oriented mini-surfaces. Since atomic adsorption depends on the surface structure, some substrate orientations are energetically favored during an MBE growth. On the other hand, the impurity trapping rate is relatively independent of the substrate orientation. Therefore, a slight substrate tilt can expose a considerable amount of atomic steps that will help the crystal growth without increasing impurity trapping.

To study the effect of substrate tilting on laser performance, we have very often used in this thesis work (100) substrates tilted toward the nearest (111)Ga plane by 4°. The substrate tilting creates microscopic steps (**Figure 3.9**) on the surface. The ratio of the height of the steps to the separation of steps determines the angle of tilting. The growth rate of (Al,Ga)As along these steps is believed higher than that on a

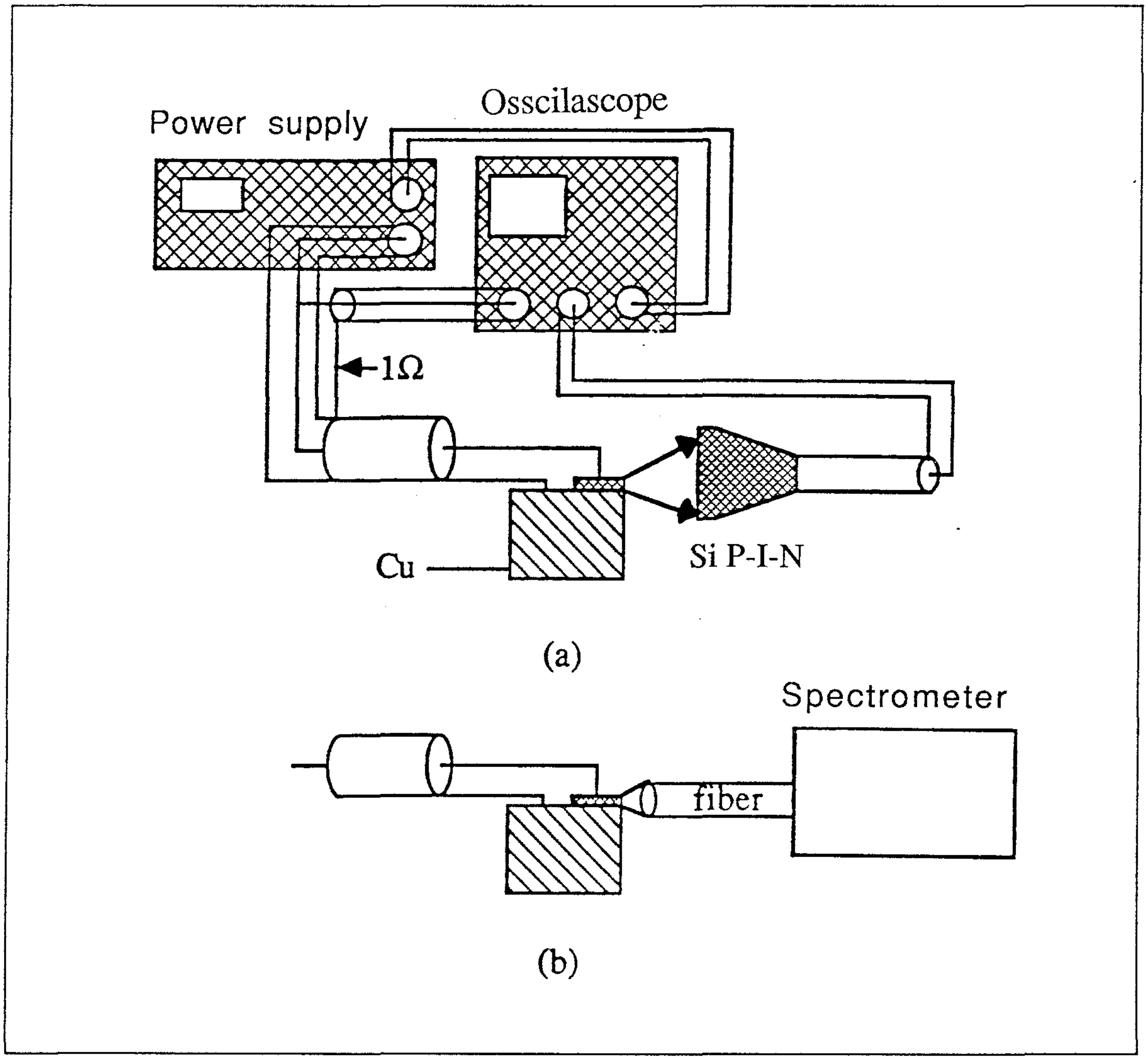

**Figure 3.7** *Schematic drawing of the experimental set-up used to measure (a) threshold current and (b) optical spectrum.*

straight (100) surface and may be responsible for the improved surface morphology and reduced impurity trapping. Furthermore, at these steps, open Ga bonds are exposed, and as a result, arsenic molecules can make additional bonds to these extra Ga atoms, thereby increasing the effective arsenic sticking coefficient. Consequently, the impurity incorporation rate is lowered because of higher arsenic incorporation.

The effect of substrate misorientation has been used successfully to improve the

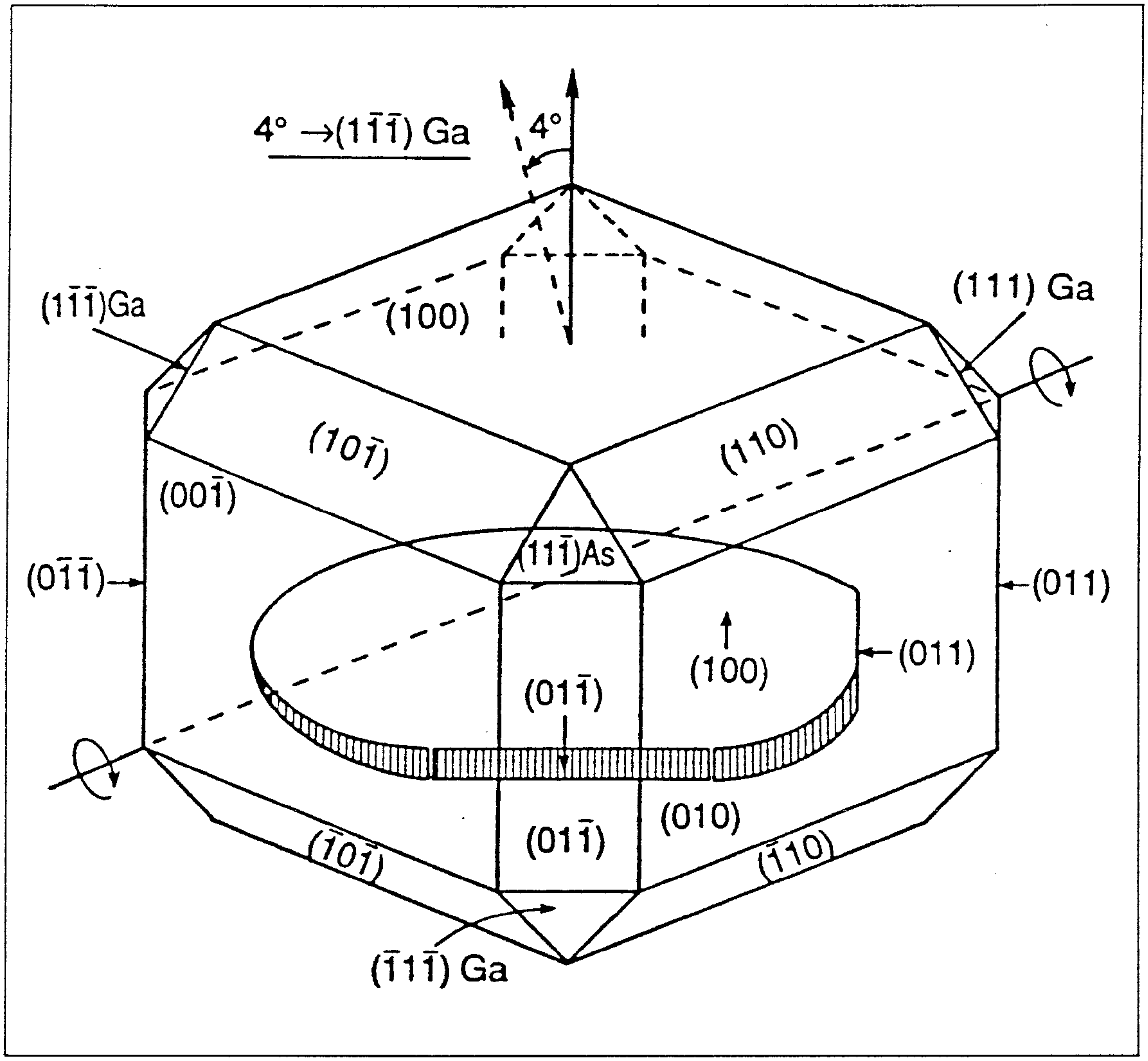

**Figure 3.8** *Schematic drawing of the various crystal orientations of GaAs. At the center of the drawing is a GaAs (100) substrate tilted 4° toward the Ga plane.*

quality of "inverted" layer growth where GaAs is grown on AlGaAs in a standard HEMT structure [10]. The tilting also improves photoluminescence (higher light intensity and narrower linewidth) from a quantum well [11]. Therefore, we further investigated the effect of substrate tilting on quantum well laser performance and the possibility of replacing all untilted substrates we were using with the tilted ones.

4° tilted and straight (100) substrate are chemically cleaned in the same process.

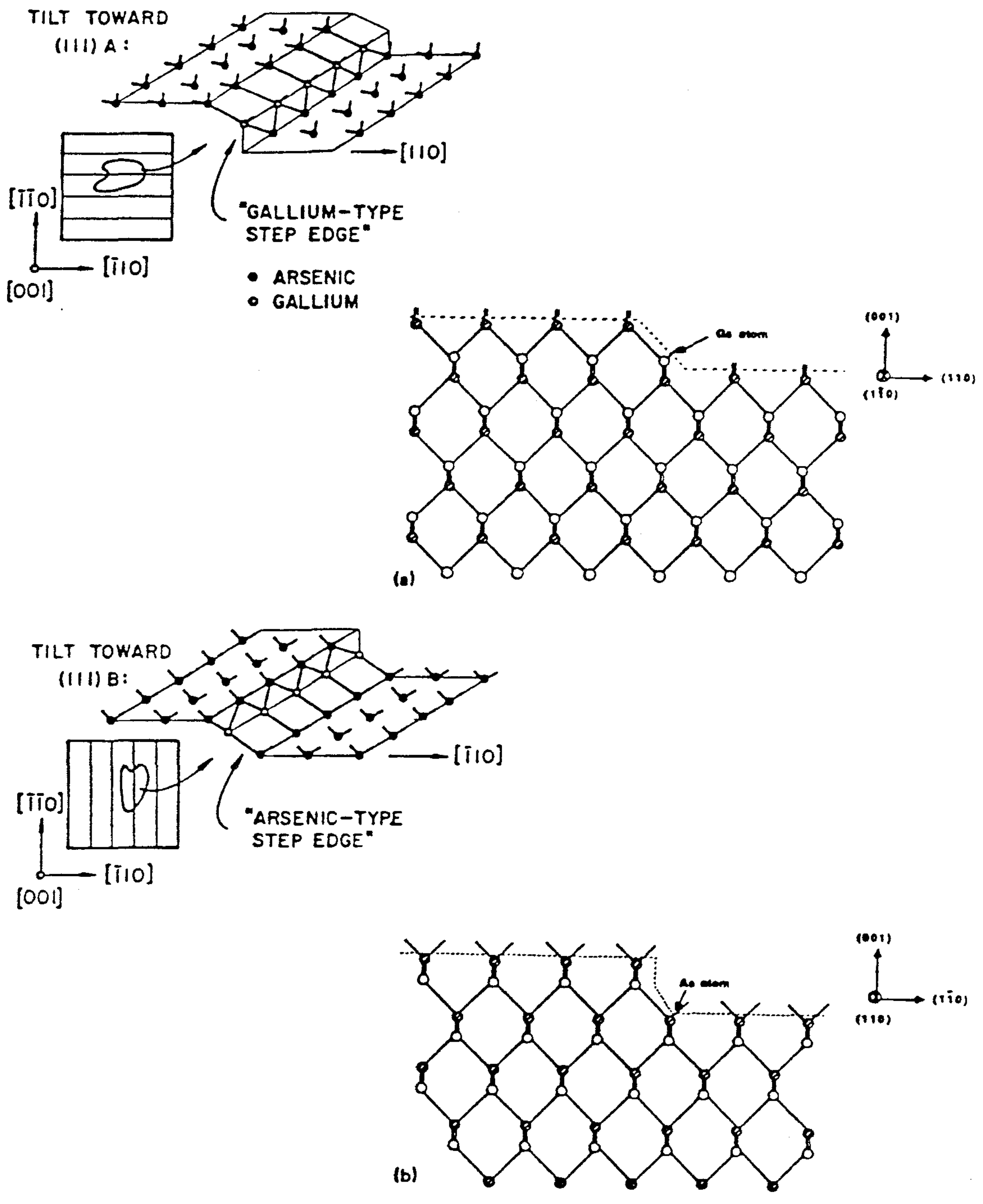

**Figure 3.9** *Schematic drawing of the atomic steps caused by substrate tilting in (a) tilted toward the (111) Ga plane, and (b) tilted toward the (111) As plane.*

Then they are In-mounted side by side on the same Mo block. The two substrates receive exactly the same treatment throughout the entire growth.

The MBE growths have revealed very dramatic differences. First, when the growth condition is optimum, e.g., the substrate temperature for AlGaAs growth is 720°C, the two substrates have produced nearly identical surface morphologies which only slightly favor the tilted one and they produce similar threshold current densities in broad area lasers, with the tilted one slightly lower. When the growth condition is not optimum, however, the tilted substrate always shows better surface morphology, even when the surface of the straight one appears so bad that it would normally prompt us to abort the growth. On several occasions, for example, when the substrate temperature was purposely set at 660-680°C (in the "forbidden window" of AlGaAs growth between 640°C and 700°C), the straight substrate could not produce any lasing device, while the tilted one produced lasers with moderately higher threshold current densities (see **Table 3.1**). **Table 3.2** shows the experimental data on lasers obtained from straight and tilted substrates at optimum growth temperature of 720°C.

Appropriate use of substrate tilting has proven effective in improving crystal quality and device performance. The use of substrate tilting, however, is not limited to improving the quality of large area crystal growth alone; it can also be used to fabricate devices such as quantum wire lasers [12] using a modified version of MBE which is called "enhanced mobility epitaxy" that deposits Ga and As atomic layers alternately. Furthermore, under optimum conditions, it helped to grow the world's lowest threshold current density lasers ($J_{th}$ of 80 A/cm$^2$). Now it has become a common practice to use tilted substrates to improve MBE growth quality in many laboratories.

### Effect of quantum well thickness on threshold current density

Quantum well thickness has been considered important to low-threshold current density because of its effect on transition energy. Calculations on the *optimum* quan-

| Substrate | Temperature(C°) | $J_{th}$(A/cm$^2$) |
|---|---|---|
| (100) | 680 | 472 |
| tilted | 680 | 163 |
| (100) | 660 | not lasing |
| tilted | 660 | 403 |

**Table 3.1** *Laser characteristics versus substrate temperature.*

tum well thickness for laser performance are common in the literature. Many of our early experimental results, however, suggest that the thickness of the quantum well should have very little effect on threshold current density. To clarify this issue, lasers with different quantum well thickness are grown under optimum conditions. **Table 3.2** shows the results of threshold current densities versus quantum well thicknesses. The threshold current density is almost constant in the range of 65-125 Å. The small fluctuations are caused by the order of growth: 65Å, 125Å, 35Å, and 95Å (later growth should be better since MBE is cleaner). This contradicts the previously accepted conclusion that at 70 Å , a noticeable drop in threshold current density can be observed [13]. We attribute their result to the relatively low quality of laser materials used in their study. Higher threshold current densities must contain *unknown* and *undesirable* effects which might be larger than the effect under investigation, and therefore can not be used to check theory. The observed relationship between $J_{th}$ and $L_z$ becomes apparent if a correct threshold condition is adopted.

| Substrate | L (Å) | L(mm) | $J_{th}$(A/cm$^2$) |
|---|---|---|---|
| (100) | 165 | 3.20 | 130 |
| tilted | 165 | 3.29 | 115 |
| (100) | 125 | 3.26 | 114 |
| tilted | 125 | 3.21 | 93 |
| (100) | 95 | 3.18 | 148 |
| tilted | 95 | 3.09 | 120 |
| (100) | 65 | 3.19 | 124 |
| tilted | 65 | 3.24 | 117 |

**Table 3.2** *Laser characteristics versus quantum well width at substrate temperature of 720° C for both tilted and straight (100) substrates.*

Physically, when the quantum well thickness is very small, for example, $L_z \leq 30$Å, the ratio of well depth to well width increases, and so does the transition energy from the electron ground state to the hole ground state $E_{1c} - E_{1hh}$. (**Table 3.3** shows the energy levels of the electron, the heavy hole and light hole, the transition energy, and the measured lasing wavelength of quantum well lasers with $L_z$ from 35 Å to 480 Å. The calculation uses a self-consistent model detailed in [8].) As a result, two things happen: first, the transparency condition that requires the separation of Fermi levels $\Delta\phi$ to be larger than the transition energy $\hbar\omega$, requires an increase in the separation between the Fermi levels to balance the increase in transition energy; second, more unbounded bulk states outside the quantum well are being filled as the Fermi levels move closer

| $L_z$(Å) | $E_{1c}$(meV) | $E_{1hh}$(meV) | $E_{1lh}$(meV) | $E_{gap}$(meV) | $E_{ph}^{mea}$(meV) |
|---|---|---|---|---|---|
| 35 | 91 | 29 | 51 | 1536 | 1536 |
| 65 | 50 | 13 | 30 | 1479 | 1485 |
| 95 | 31 | 7 | 19 | 1454 | 1445 |
| 125 | 20 | 4 | 13 | 1440 | 1433 |
| 165 | 13 | 3 | 9 | 1432 | 1423 |
| 300 | 4 | 1 | 3 | 1421 | 1401 |
| 480 | 2 | 1 | 1 | 1419 | 1400 |

☐ exciton binding energy is assumed to be 8meV

**Table 3.3** *The energy levels of the electron, the heavy hole and light hole, the transition energy, and the measured lasing wavelength of quantum well lasers with $L_z$ from 35 Å to 480 Å.*

to conduction and valence band edges, thereby increasing the recombination current in the GRIN region substantially.

If we denote the necessary increase in the Fermi level difference by $\delta\phi$, then the excess recombination current density $J_{excess}$ will have to be increased by a factor of $exp(\beta\delta\phi)$ according to the standard p-n junction theory, where $\beta$ is a constant depending on temperature. Using the calculated energies of $E_{1c}$ and $E_{1hh}$, it can easily be verified that $J_{excess}$(35Å) is 40 times of $J_{excess}$(125Å) and 100 times of $J_{excess}$(480Å). This is why it does not pay to use a very thin quantum well as active layer. The gain from reducing the quantum well volume is offset by the effective reduction of quantum well depths $\Delta E_c$ and $\Delta E_v$ through $exp(\beta\Delta E_c)$ and $exp(\beta\Delta E_v)$. In other words, there is a trade-off between quantum well volume and carrier confinement. On the other hand, an individual carrier can experience yet another effect that only concerns the behavior of a single electron known as the real space electron transfer effect in which case the electron wavefunctions in a quantum well will tail into the higher bandgap AlGaAs region, thereby reducing the number of carriers in the well. However, this effect is only important when $L_z < 30$Å. 30Åis a borderline also because the fluctuation in $L_z$ is about two atomic layers, $\sim$ 10 Å.

On the other hand, when $L_z \rightarrow \infty$, two things can also happen to increase the threshold: first, the condition under which two-dimensional bimolecular recombination occurs in a two-dimensional plane is changed, and carriers now recombine in a three-dimensional space with a higher density of states; second, the nature of electron wavefunctions begin to change so that the differential gain coefficient $g^{2D}$ (usually larger than $g^{3D}$) has to be replaced by $g^{3D}$.

The transition from 2D to 3D is a gradual process. As far as device performance is concerned, it occurs when $J_{th}$ begins to increase linearly with $L_z$, which has been observed (**Figure 3.10**) experimentally. Physically, the transition from 2D to 3D represents a process in which carriers in the ground state of a 2D system begin to occupy the second and higher quantized energy levels. To estimate the transition quantum well width, we can define (this is somewhat subjective) the quantum well width $L_z^{trans}$ to be one for which the total number of electrons in ground state (i=1) equals to the total number of electrons in second and higher (i=2,3……) quantized states, $n_1 = n_2 + n_3 + ......$, and solve it numerically. The result, 160Å, is very close to the experimental turning point that is shown in **Figure 3.10**.

### A more rigorous treatment

The well width dependence of gain and threshold current in a quantum well laser can be deduced from a treatment given by Yariv [14] on the gain in a quantum well

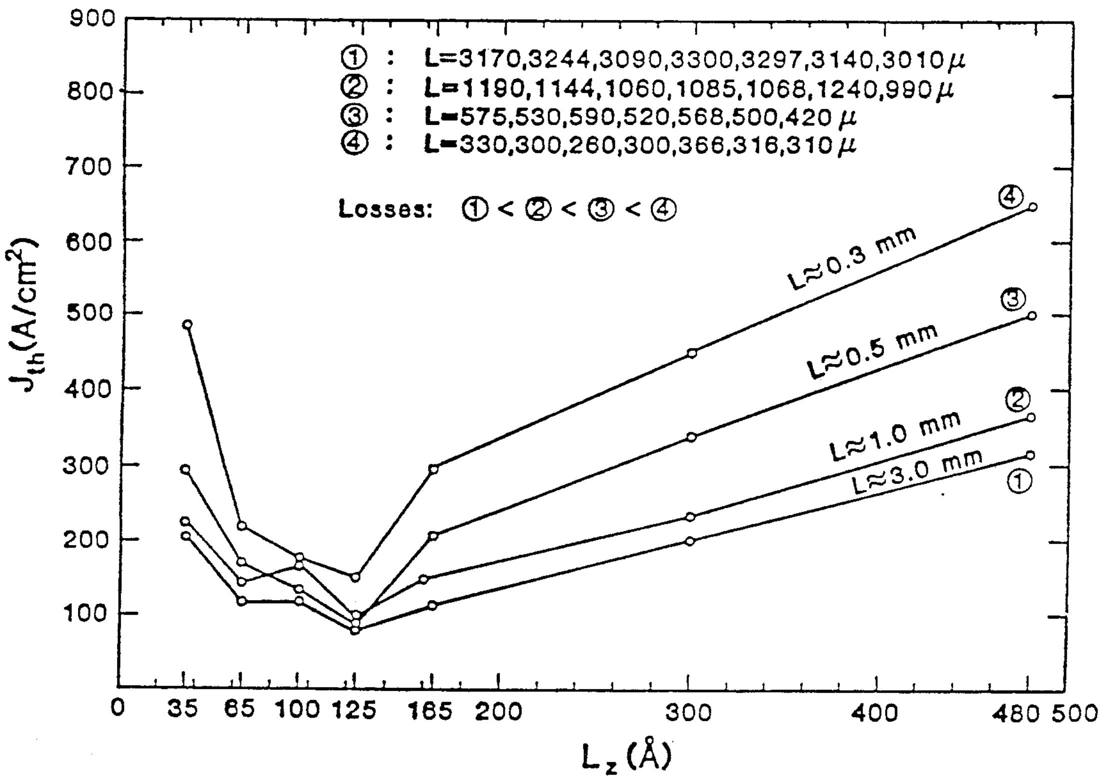

**Figure 3.10** *Experimental data showing the relationship between threshold current density* $J_{th}$ *and quantum well width* $L_z$. *The four curves represent four different cavity lengths, 0.3mm, 0.5mm, 1.0mm, and 3.0mm.*

laser which is based on a rigorous density matrix formalism [15]. This treatment also includes the effect of gain broadening not discussed here.

We start with the expression for the complex susceptibility of an electronic material well below optical gain saturation [14]

$$\chi(\omega) \;=\; (N_2 - N_1) \times \frac{\mu^2 T_2[(\omega_0 - \omega)T_2 - i]}{\epsilon_0 \hbar[1 + (\omega - \omega_0)^2 T_2^2]} \tag{3.1}$$

and the gain is given by

$$\gamma(\omega) \;=\; -\,\frac{k}{n_r^2}\chi''(\omega) \tag{3.2}$$

The calculation involves the counting of $N_2 - N_1$ in (3.1). Since a single electron state in a crystal is characterized by its wave vector $\vec{k}$, the counting of $N_2 - N_1$ is translated into an integration over $\vec{k}$'s satisfying certain conditions. The first condition is the $\vec{k}$-selection rule. In a perfect crystal, the electronic momentum $\hbar\vec{k}$ is much larger than the photon momentum $\hbar\vec{k}_{photon}$; therefore, in the independent electron approximation [16], $\vec{k}_c = \vec{k}_v$ holds for an optical transition. In a crystal containing a large number of lattice mismatch or impurity defects, the $\vec{k}$-selection rule is likely to be violated since the impurities can take up an appreciable amount of electronic momentum and as a result, $\vec{k}_c \neq \vec{k}_v$. This situation has been analyzed by Landsberg et al. [17], and used by Saint-Cricq et al. [18], to calculate the gain and the threshold current in quantum well lasers.

In a real laser, the situation is somewhat in between the two limiting cases. In the following, we will try to apply both rules in the gain calculations and then compare them to experimental data. The difference is in the counting of the number of electrons that will make a transition from the conduction band to the valence band with $\vec{k}$ value between $\vec{k}_c$ and $\vec{k}_c + d\vec{k}_c$ in conduction band, and between $\vec{k}_v$ and $\vec{k}_v + d\vec{k}_v$ in valence band.

In the case of $\vec{k}$-selection rule,

$$d(N_2 - N_1)^{\vec{k}=\vec{k}'} = \frac{1}{L_z}\rho_r(E_c)[f_c(E_c) - f_v(E_c - \hbar\omega_0)]dE_c \tag{3.3}$$

but in the case of non-$\vec{k}$-selection rule, each electron in the conduction band has the additional possibility of recombining with *any* hole in the valence band. And there are a total of

$$V \times \int \frac{\rho_v(E)}{L_z} f_v(E)dE \tag{3.4}$$

holes for each electron in the conduction band. Furthermore, the non $\vec{k}$-selection rule results in a modification of the transition probability [19,40] by a factor of $\mu_{env}$. So the combined effect gives for the non-$\vec{k}$-selection case,

$$d(N_2 - N_1)^{\vec{k}\neq\vec{k}'} = \int dE_v \; V\frac{1}{L_z}\rho_c(E_c)\frac{1}{L_z}\rho_v(E_v) \times [f_c(E_c) - f_v(E_v)] \; |\mu_{env}|^2 dE_c \tag{3.5}$$

The exponential gain coefficient is thus

$$\gamma(\omega)^{\vec{k}=\vec{k}'} = \frac{2\pi\mu^2 m_r}{\lambda_0\epsilon_0 n_r\hbar^2 L_z}\int d\omega_0 \sum_{n=1}^{\infty} H[\hbar\omega - (E_g + E_{nc} + E_{nv})] \times [f_c(\hbar\omega_0) - f_v(\hbar\omega_0)]\frac{T_2}{\pi[1+(\omega-\omega_0)^2T_2^2]} \tag{3.6}$$

for $\vec{k}$-selection, and

$$\gamma(\omega)^{\vec{k}\neq\vec{k}'} = \frac{2\mu^2 m_c m_v}{\lambda_0\epsilon_0 n_r\hbar^4 L_z^2}\int d\omega_0 \int dE_v \sum_{n=1}^{\infty} H[\hbar\omega - (E_g + E_{nc} + E_{nv})] \times [f_c(\hbar\omega_0) - f_v(\hbar\omega_0)]\frac{T_2}{\pi[1+(\omega-\omega_0)^2T_2^2]}V \; |\mu_{env}|^2 \tag{3.7}$$

for non-$\vec{k}$-selection rule.

The well width dependence is simply

$$\begin{aligned} \gamma(\omega)^{\vec{k}=\vec{k}'} &\sim \frac{1}{L_z} \\ \gamma(\omega)^{\vec{k}\neq\vec{k}'} &\sim \frac{1}{L_z^2} \end{aligned} \tag{3.8}$$

where

$$\begin{aligned}
\hbar\omega_0 &= E_g \;+\; E_c \;+\; E_v \\
E_c &= \frac{\hbar^2}{2m_c}(k^2 \;+\; n^2\frac{\pi^2}{L_z^2}) \\
E_v &= \frac{\hbar^2}{2m_v}(k^2 \;+\; n^2\frac{\pi^2}{L_z^2}) \\
\rho_{r,c,v} &= \frac{m_{r,c,v}}{\pi\hbar^2} \\
m_r &= \frac{m_c m_v}{m_c + m_v} \\
\lambda_0 &= \frac{c}{2\pi\omega_0} \\
f_c(E) &= \frac{1}{1+e^{(E-\phi_n)/kT}} \\
|\mu_{env}|^2 &= \frac{1}{V}64\pi \times (\frac{\epsilon m_e a_0}{m_c})^3 \times (1 + a_0^2k^2)^{-4} \\
k &= \sqrt{\frac{2mE(k)}{\hbar^2}} \\
a_0 &= 0.52810^{-8} cm \\
H(x) &= 1 \; if \; x > 0, \; H(x) \;=\; 0 \; if \; x < 0
\end{aligned}$$

and $\hbar\omega$ = photon energy, $\mu$ = dipole matrix element, $T_2$ = intraband relaxation time, and $n_r$ = refractive index. All the quantities are in CGS units.

The difference between the $\vec{k}$-selection and non-$\vec{k}$-selection rules on the gain can be estimated as follows

$$\frac{\gamma(\omega)^{\vec{k}=\vec{k}'}}{\gamma(\omega)^{\vec{k}\neq\vec{k}'}} \approx \frac{\rho_r}{V\rho_c\rho_v|\mu_{env}|^2\Delta E} \tag{3.9}$$

taking

$$\begin{aligned}\Delta E &\approx \hbar/\tau \\ m_c &= 0.067\ m_e \\ m_v &= 0.48\ m_e \\ |\mu_{env}|^2 &\approx \frac{1}{V}64\pi \times (\frac{\epsilon m_e a_0}{m_c})^3\end{aligned}$$

we get

$$\begin{aligned}\frac{\gamma(\omega)^{\vec{k}=\vec{k}'}}{\gamma(\omega)^{\vec{k}\neq\vec{k}'}} &\approx \frac{\hbar L_z \tau}{(m_c+m_v)64(\epsilon m_e a_0/m_c)^3} \\ &\approx 30[\frac{L_z}{100\mathring{A}}][\frac{\tau}{1ns}]\end{aligned} \tag{3.10}$$

A rigorous numerical calculation yields a ratio of 6.02 instead of 30.

The gain calculated using non-$\vec{k}$-selection rule, therefore, is significantly lower than using $\vec{k}$-selection. This agrees with the general prediction made by other authors [17,18] that the advantage of a quantum well laser is only apparent when $\vec{k}$-selection is assumed.

### Transparency sheet carrier density

To reach lasing, the quantum well material has to become optically transparent, that is, $\gamma(\omega)$=0. According to (3.2), this happens when $f_c(E_c) - f_v(E_c - \hbar\omega_0)$=0. In two dimensions, the density of states for i-th subband is given by

$$\rho_i = \frac{m_i}{\pi\hbar^2} \tag{3.11}$$

where $m_i$ is the effective mass of the carrier in i-th subband. The total carrier density is thus

$$\begin{aligned} n &= \sum_i \int \rho_i \; f_c(E_{ci}) dE_{ci} \\ &= kT \sum_i \rho_i \; ln[1 + e^{(\phi_n - E_{ci})/kT}] \\ &= \frac{m_c kT}{\pi \hbar^2} \sum_i \; ln \; \frac{1}{1 - f_c(E_{ci})} \end{aligned} \tag{3.12}$$

for electrons, and a similar expression for holes.

Since the energy separation between the first (i=1) and the second (i=2) levels is larger than $3kT$ for a typical quantum well ($L_z \leq 150Å$) used in GRINSCH lasers, and the main contribution to the Fermi functions $f_c$ and $f_v$ are from the ground states, only the ground states (i=1) will be considered. Therefore,

$$f_c(E_{c1}) \;=\; 1 \;-\; e^{-(\pi\hbar^2/m_c kT)n} \tag{3.13}$$

and similarly

$$f_v(E_{v1}) \;=\; e^{-(\pi\hbar^2/m_v kT)p} \tag{3.14}$$

Since $n = p$, the transparency condition $f_c - f_v = 0$ becomes

$$e^{-(\pi\hbar^2/m_c kT)n} \;+\; e^{-(\pi\hbar^2/m_v kT)n} \;=\; 1 \tag{3.15}$$

Notice that the equation does not depend on $L_z$ and this is why the transparency current density for a ideal quantum well laser is independent of the well thickness. Using the following values for GaAs, $m_c = 0.067m_e$, $m_v = 0.48m_e$, and $T = 300K$, the sheet carrier density $n$ can be determined from (3.15)

$$n(m_c, m_v, T) \;=\; 1.15 \times 10^{12} cm^{-2} \tag{3.16}$$

## Recombination lifetime

Both theory [20,21] and experiment [22,23] indicate that the recombination rate as well as lifetime are constant; furthermore, Christen et al. [22], have measured the lifetime $\tau$: $\tau$ = 7.0 ns for an undoped 110 Å quantum well, and $\tau$ = 3.25 ns for a p-doped 1.0× $10^{16}$cm$^{-3}$ quantum well. Matsusue et al. [24] have found the lifetime in undoped quantum wells to be 5 ns. The background doping in our MBE system was measured to be 1.0× $10^{16}$cm$^{-3}$ of p type. Therefore, we take $\tau = 3$ ns as given by Christen [22].

Thus the transparency current density for an ideal 2D GaAs is

$$J_0 = ne/\tau \tag{3.17}$$

and $\tau = 3$ ns, $J_0 = 63A/cm^{-2}$.

This value of $J_0 = 63A/cm^{-2}$ is in good agreement with the transparency current density calculated by Thomphoson [25] for bulk GaAs using a strict $\vec{k}$-selection rule (Thomphoson obtained $J_0 = 4000A/cm^2\mu m^{-1}$, which would give for 100 Å $J_0 = 40A/cm^2$). This illustrates the major advantage of quantum well lasers: a large reduction of the transparency current. And this advantage is not offset by the confinement factor $\Gamma_{QW}$ discussed below since the optical field is very weak below the transparency.

### Above transparency

So far it is shown that a $J_0$ which only depends on the material parameters, is required to make the quantum well transparent. Above the transparency, optical field becomes strong in the cavity, and the modal gain experienced by an optical mode propagating along the junction plane is modified by a confinement factor

$$\gamma_{mode}(\omega) = \gamma(\omega)\Gamma_{QW} \tag{3.18}$$

where the confinement factor $\Gamma_{QW}$ is given by

$$\Gamma_{QW} = \frac{\int_{-L_z/2}^{L_z/2} |E|^2 dz}{\int_{-\infty}^{\infty} |E|^2 dz} \approx \frac{L_z}{W_{mode}} \tag{3.19}$$

The modal gain $\gamma_{mode}^{\vec{k}=\vec{k}'}$ is therefore independent of well width $L_z$; however, the modal gain $\gamma_{mode}^{\vec{k}\neq\vec{k}'}$ depends on $L_z$

$$\gamma_{mode}^{\vec{k}\neq\vec{k}'}(\omega) \sim \frac{1}{L_z^2} \times \frac{L_z}{W_{mode}} \propto \frac{1}{L_z}. \tag{3.20}$$

To obtain the threshold current density, the modal gain $\gamma_{mode}(\omega)$ is multiplied by a factor $g$ that is independent of $L_z$ [24]. The factor $g$ can be easily measured from $J_{th}$ versus $L_z$ curve for quantum well lasers of different width. Our measurements yielded a single value of $g = 0.7\ A/cm$ which is roughly independent of $L_z$.

The total threshold current density for both $\vec{k}$-selection and non $\vec{k}$-selection cases are plotted in **Figure 3.11** and compared to experiment. It is clear that the $\vec{k}$-selection rule fits experimental data and should be observed. This calculation differs from the one by Saint-Cricq [18] which does not use the correct matrix element that includes the effect of envelope wavefunction. It is also in qualitative agreement with the calculations assuming a $\vec{k}$-selection rule [26,27,28,29,30,31,32]. The most striking feature of the non-$\vec{k}$-selection rule is a linear increase of the threshold current density with quantum well width. This, however, has not been observed in our measurements. And since all the lasers used in this study have a undoped quantum well, it is safe to conclude that the non-$\vec{k}$-selection rule does not hold for undoped materials.

### Higher order corrections due to band-mixing

The previous calculation can be regarded as a first order approximate theory which is valid in the *two-dimensional* and *perfect crystal* limit. A rigorous theory, however, has to take into account the effect of band-mixing as a result of realistic band structures [33]. Recently, more basic studies [34,35,36,37] have shown that with more detailed analysis, the band structure and optical matrix elements of the quantum well can be quite different from the ones used in the previous calculations (equations (3.6),(3.7)). The dispersion relationship $E(\vec{k})$ can be numerically computed from a more fundamental $\vec{k} \cdot \vec{p}$ method [32,36,37], and the density of states can be obtained by

$$\rho_i(E) = \int_{S_i(E)} \frac{dS}{4\pi^3 |dE(\vec{k})/d\vec{k}|} \tag{3.21}$$

where $S_i(E)$ is the surface in $\vec{k}$ space obeying the equation $E_i(E) = E$, for the i-th

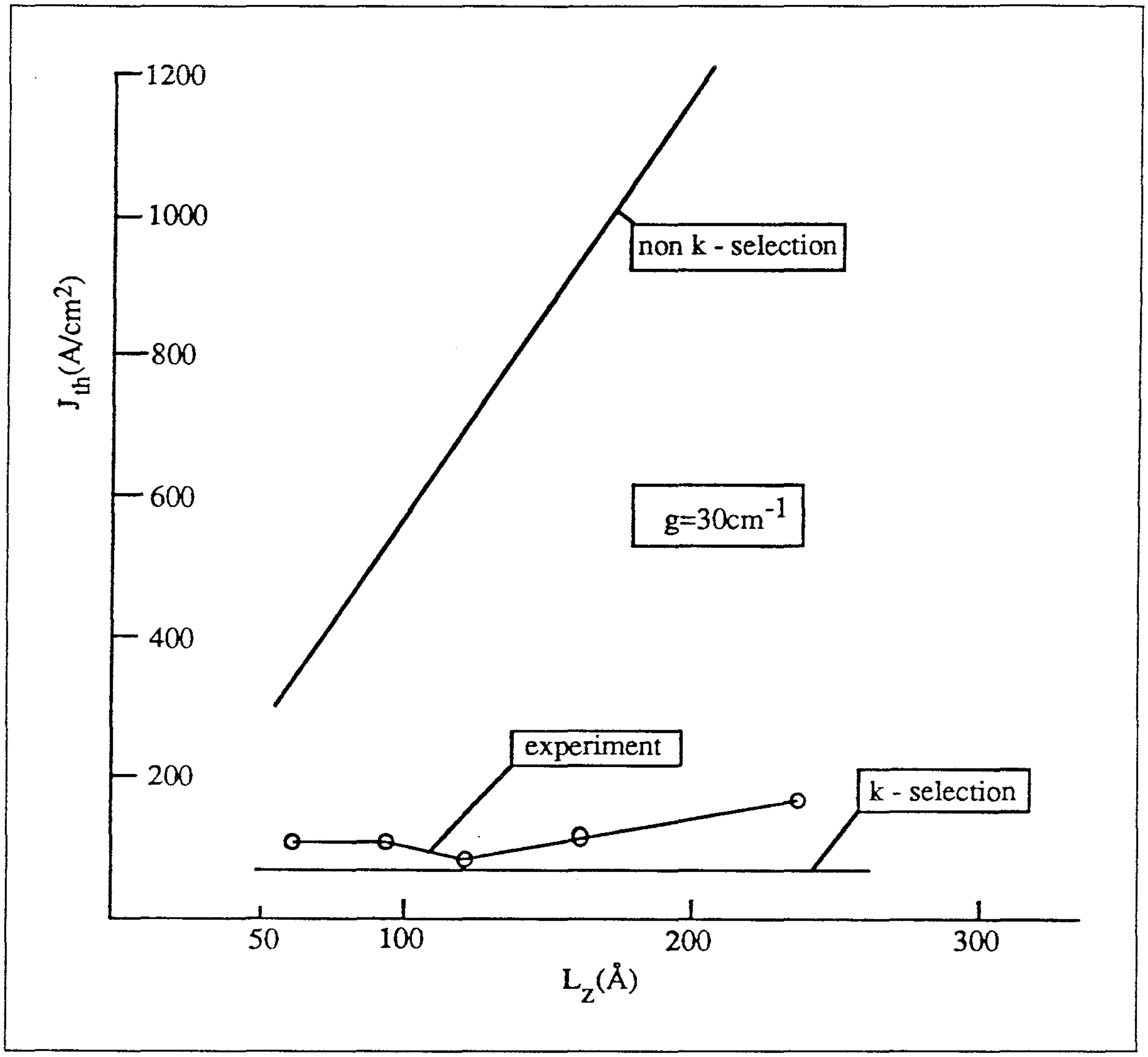

**Figure 3.11** *The calculated threshold current density versus quantum well width for both $\vec{k}$-selection and non-$\vec{k}$-selection cases.*

subband. The surface integral in the limit of $L_z \to 0$, is

$$\begin{aligned} \rho_i(E) &= \frac{2 \times \pi \vec{k}^2 \; + \; 2\pi k \times \frac{2\pi}{L_z}}{4\pi^3 |dE(\vec{k})/d\vec{k}|} \\ &= \frac{k}{\pi L_z} \left| \frac{d\vec{k}}{dE_i(\vec{k})} \right| \end{aligned} \tag{3.22}$$

This density of states can be substituted into equations (3.3), (3.5), (3.6) and (3.7) to calculate gain.

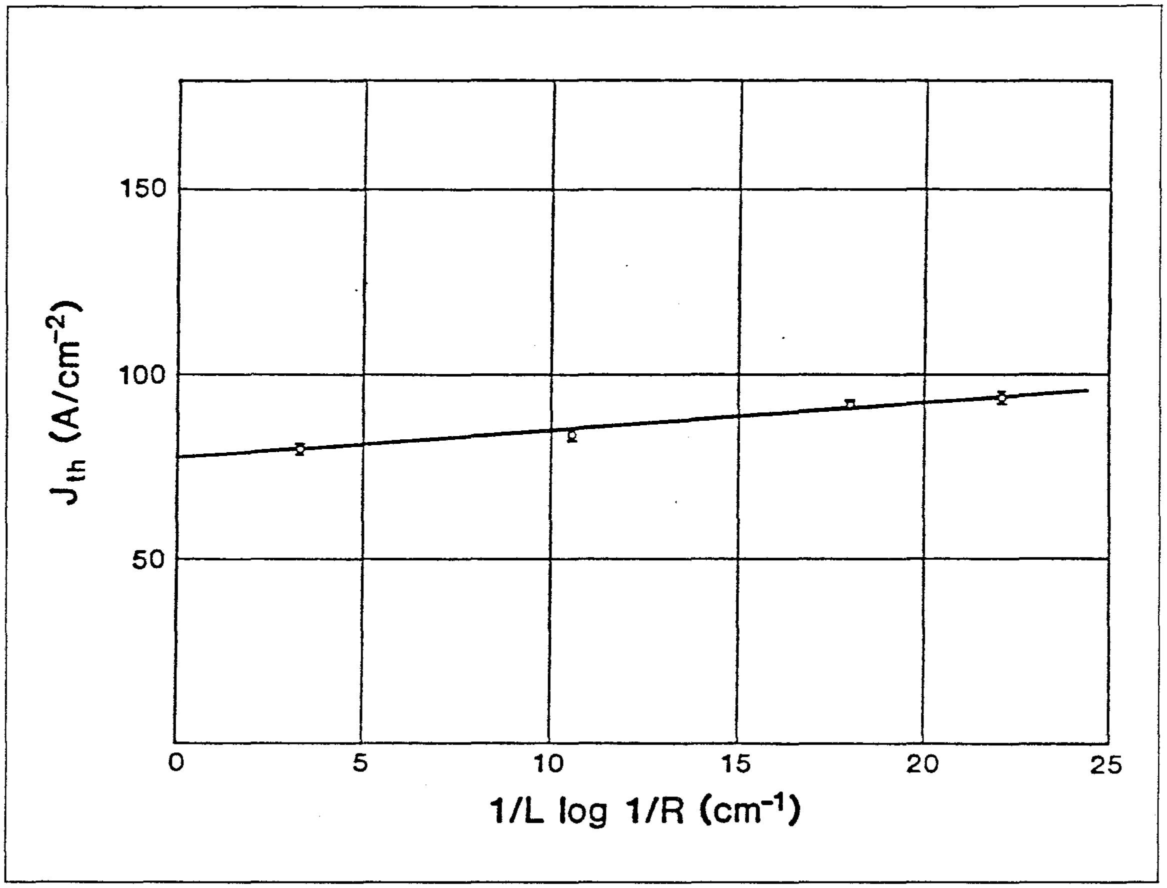

**Figure 3.12** *The plot of threshold current density versus inverse cavity length for one of the best GRINSCH lasers obtained in this research. The threshold current density is well below 100 A/cm$^2$.*

### Experimental determination of $J_0$

If the cavity length is long enough, the mirror loss will be small, and the threshold current density will approach the transparency current density. During this study, the lowest threshold current density ever obtained in any semiconductor laser has been demonstrated. **Figure 3.12** shows the threshold current density versus reciprocal cavity length for the best laser device obtained in this study:

$$\begin{aligned} J_{th} &= 98A/cm^2 \qquad L = 520\mu m \\ &= 80A/cm^2 \qquad L = 3300\mu m \end{aligned} \tag{3.23}$$

and an external quantum efficiency of 85%.

The portion of current density due to mirror loss and free carrier absorption can be estimated

$$J \;=\; g(\alpha + \frac{1}{L} ln \frac{1}{R}) \tag{3.24}$$

The gain coefficient $g$ was measured to be 0.7 A/cm, $\alpha$=15/cm, and $R$=3.6. For $L$=3.3mm, $J$=20A/cm$^2$. The measured transparency current density is 60 A/cm$^2$, agrees well with the calculated value of 63 A/cm$^2$.

Another indication that our quantum well material is of very high quality, is demonstrated by the fact that when mounted upside down on a diamond heat sink, one such laser can put out nearly 3 Watts of CW power from a 100 $\mu$m stripe, and it can also be biased to a record high of 130 times above its threshold.

## Other substrate orientations

Recently, Hayakawa et al.[38], have used (111)As 0.5° → (100) substrates to grow quantum well lasers and obtained threshold current density as low as 120 A/cm$^2$. They attributed the good result to heavier hole effective mass along (111)As and concluded that the differential gain can be improved. This argument presents some problems, since the ideal situation for a high differential gain coefficient is to have the conduction band and valence band with similar effective masses. This is explained in the following:

$$n \;=\; N_c \; e^{-\beta(E_c - \phi_n)} \qquad and \qquad p \;=\; N_v \; e^{-\beta(\phi_p - E_v)} \tag{3.25}$$

where $N_{c,v} \;\propto\; m_{c,v}^{3/2}$ are effective density of states. We require that first, $\phi_n - \phi_p = \hbar\omega$, and second, $|\phi_n - E_c| \;+\; |\phi_p - E_v|$ be minimized. Furthermore, $p \approx n$ at threshold. The second requirement will give a minimum current density. Using equation (3.1) and treating $m_c$ and $m_v$ as parameters, it is easy to show that:

$$m_c \; m_v \;= Const. \tag{3.26}$$

$$\frac{1}{m_c} + \frac{1}{m_v} \;=\; minimum \tag{3.27}$$

will happen only when $m_c = m_v$.

Physically, when a laser is forward biased, the separation of electron and hole quasi-Fermi levels $\phi_n$ and $\phi_p$ reaches the value of transition energy as soon as $\phi_n$ and $\phi_p$ move into the conduction and valence band, respectively. A very large hole effective mass slows down the movement of $\phi_p$, so that $\phi_n$ has to move significantly into the conduction band to satisfy transparency condition $\phi_n - \phi_p = \hbar\omega$. The electron Fermi level located deep in the conduction band can give rise to a large threshold current, which is exactly what we don't want. Therefore, the success of (111) substrate must be due to the improved MBE growth of AlGaAs crystal on (111) oriented facets [39] in general.

The possibility of many other tilting orientations is under investigation currently.

### Keys to a low-threshold laser growth

Here we summarize the key factors to a low-threshold laser growth (it also applies to any other device).

**First, the quantum well width $L_z$ should be small enough so that two dimensional effects dominate, but large enough so that the interface quality is not affected. A working range from 30 to 150 Å is available depending on the choice of lasing wavelength.**

**Second, the substrate temperature $T_{ST}$ should be kept at 600°C for GaAs growth and 720°C for AlGaAs growth. An indium-free direct heating mount can be used to further improve the required rapid change in substrate temperature.**

**Third, there are now at least two other types of substrate that produce lower threshold current density results than the conventional (100) oriented substrate:**

**(i) (100) 4° → (111)Ga**

**(ii) (111)As 0.5° → (100)**

## § 3.6 Conclusions

In this chapter, we have described the details of GaAs/AlGaAs quantum well laser growth, the fabrication and measurement of broad area lasers, and the effect of substrate misorientation. It is shown that a proper substrate tilting can greatly improve the MBE growth of GaAs and AlGaAs under all circumstances, especially when the growth condition is not optimum. The use of tilted substrates has resulted in the lowest threshold current density ever reported for any semiconductor lasers. The experimental value of 80 A/cm$^2$ for a 3.3mm long laser is an improvement of a factor of 3 over the previous record.

The effect of quantum well width on threshold current density is analyzed using both the $\vec{k}$-selection rule and the non-$\vec{k}$-selection rule. It is found that in an undoped material, the $\vec{k}$-selection rule gives a very good fit of the experimental data. Furthermore, $\vec{k}$-selection rule gives a modal gain that is independent of $L_z$, compared to the non-$\vec{k}$-selection result that shows a $L_z^{-1}$ dependence.

The transparency current density $J_0$ is calculated using $\vec{k}$-selection rule, which compares very favorably with experimental results (5% difference).

## § 3.7 References

[1] C. T. Foxon, B. A. Joyce, and M. T. Norris, J. Cryst. Growth, **49**, 132(1980), also J. H. Neave, B. A. Joyce, P. L. Dobson, and N. Norton, Appl. Phys. , **A31**, 1(1983), and references therein.

[2] Y. G. Chai and R. Chow, Appl. Phys. Lett. , **38**, 796(1981).

[3] E. A. Wood, J. Appl. Phys. , **35**, 1306(1963).

[4] A. Y. Cho, J. Appl. Phys. , **47**, 2841(1976).

[5] H. Z. Chen, A. Ghaffari, H. Morkoç, and A. Yariv, Appl. Phys. Lett. , **51**, 1094(1987).

[6] G. W. Wicks, W. I. Wang, C. E. C. Wood, L. F. Eastman, and L. Rathbun, J. Appl. Phys. , **52**, 5792(1981).

[7] W. T. Tsang, Appl. Phys. Lett. , **39**, 134(1981).

[8] H. Morkoç, T. J. Drummond, and R. Fisher, J. Appl. Phys. , **52**, 1030(1982).

[9] D. Z. Garbusov, I. N. Arsentyev, A. V. Ovchinnikov, and I. S. Tarasov, CLEO procedings, THU4, 1988.

[10] D. C. Radulescu, G. W. Wicks, W. J. Schsff, A. R. Calawa, and L. F. Eastman, J. Appl. Phys. , **62**, 854(1987).

[11] P. N. Uppal, J. S. Ahearn, and J. W. Little, J. Vac. Sci. Technol. , **B6**, 597(1987).

[12] M. Tsuchiya, J. M. Gaines, R. H. Yan, R. J. Simes, P. O. Holtz, L. A. Coldren and P. M. Petroff, unpublished.

[13] T. Fujii, S. Yamakoshi, K. Nanbu, O. Wada, and S. Hiyamizu, J. Vac. Sci. Technol. , **B2**, 259(1984).

[14] A. Yariv, *Quantum Electronics*, 3rd Ed, John Wiley & Sons, New York, 1989.

[15] Loudon, *The Quantum Theory of Light*, Oxford University Press, London, 1973.

[16] N. Ashcroft and N. Mermin, *Solid State Physics*, Holt-Saunders, Philadelphia, 1976.

[17] P. T. Landsberg, M. S. Abrahams, and M. Osinski, IEEE J. Quantum Elec-

tron. **QE – 21**, 24 (1985).

[18] B. Saint-Cricq, F. Lozes-Dupuy, and G. Vassilieff, IEEE J. Quantum Electron. **QE–22**, 625 (1986).

[19] G. Lasher and F. Stern, Phys. Rev. **133**, A553 (1964), and W. P. Dumke, Phy. Rev. **132**, 1998 (1963).

[20] A. Sugimura,IEEE J. Quantum Electron. **QE – 20**, 336 (1984).

[21] R. J. Nelson and R. G. Sobers, Appl. Phys. Lett. **49**, 6103 (1978).

[22] J. Christen and D. Bimberg, Surface Science, **174**, 261 (1986).

[23] J. E. Fouquet and R. D. Burnham, IEEE J. Quantum Electron. **QE – 22**, 1799 (1986).

[24] T. Matsusue and H. Sakaki, Appl. Phys. Lett. , **50**, 1429(1987).

[25] M. G. H. Thomphoson, *Physics of Semiconductor Laser Devices*, John Wiley & Sons, New York, 1980.

[26] Y. Arakawa and A. Yariv, J. Quantum Electron. **QE – 22**, 1887 (1986).

[27] H. Z. Chen,J. Paslaski,A. Yariv, H. Morkoç, and G. Ji, unpublished.

[28] M. Asada, Y. Miyamoto, and Y. Suematsu, J. Quantum Electron. **QE – 22**, 1915 (1986).

[29] M. Asada, A. Kameyama, and Y. Suematsu, J. Quantum Electron. **QE – 20**, 745 (1984).

[30] E. Zielinski, H. Schweizer, S. Hausser, R. Stuber, M. H. Pilkuhn, and G. Weimann,IEEE J. Quantum Electron. **QE – 23**, 969 (1987).

[31] S. P. Cheng, F. Brillouet, and P. Correc, J. Quantum Electron. **QE – 24**, 2433 (1988).

[32] S. R. Chinn, P. S. Zory, and A. R. Reisinger, IEEE J. Quantum Electron. **QE – 24**, 2191 (1988).

[33] S. Colak, R. Eppenga, and M. F. H. Schuurmans, IEEE J. Quantum Electron. **QE–**

**23**, 960 (1987).

[34] J. N. Schulman and Y-C. Chang, Phy. Rev. **B31**, 2056 (1985).

[35] D. Nino, M. A. Gell, and M. Jaros, J. Phys. C. 1986.

[36] G. Bastard, in *Molecular Beam Epitaxy and Heterostructures*, L. L. Chang and K. Ploog, Eds. , Dordrecht, Boston, 1985.

[37] R. Eppenga, M. F. H. Schuurmans, and S. Colak, Proc. Int. Conf. Phy. Semi. , Stockholm, Sweden, 453 (1986).

[38] T. Hayakawa, T. Suyama, K. Takahashi, M. Kondo, S. Yamamoto, and T. Hijikata, Appl. Phys. Lett. , **52**, 339(1987).

[39] M. Hoenk, H. Z. Chen, K. Vahala, and A. Yariv, very recent results show strong luminescence from AlGaAs layer grown by MBE on etched (111) surface, Appl. Phys. Lett. , **54**, 1347(1989).

[40] Casey and M. Panish, *Heterostructure Lasers*, Academic Press, New York, 1978.

[41] E. P. O'Reilly, K. C. Heasman, A. R. Adams and G. P. Witchlow, Superlattices and Microstructures, **3**, 99(1986).

# Chapter 4

## Potentialities and Limitations of GaAs-on-Si Technology

### § 4.1 An introduction

The amount of research on GaAs growth on Si by MBE and MOCVD has soared world wide from near zero in 1984 to now include most major III-V research groups [1]. The potential applications have been so attractive that "everyone is trying it," so to speak. In the beginning, most of the effort is directed at using GaAs for MESFET's and HBT's in electronic circuitry [2]. Recently, the success of room temperature continuous wave operation of GaAs quantum well lasers on Si has opened way to a entirely new class of optoelectronic devices [3]. high-speed modulation of GaAs-on-Si lasers [3] and high-speed GaAs-on-Si p-i-n photodiodes have also been reported for the first time [4].

In this chapter, some general questions concerning GaAs-on-Si research are answered. The advantages and limitations are discussed.

### § 4.2 GaAs versus Si

The large share of enthusiasm for GaAs and other III-V semiconductors is based on their high electron mobilities and optoelectronic properties. III-V materials have electron mobilities from 2 to 20 times greater than that of Si. More importantly, Si is not a direct bandgap material suitable for optoelectronics.

In electronics, the search for physical limits to miniaturization reveals the reason why GaAs and other III-V compounds have not replaced Si in integrated circuit applications: the limits have little to do with mobility; they are basically determined by (i) avalanche breakdown fields, and (ii) thermal problems. It is necessary to have a large bandgap to prevent intrinsic thermal excitation of carriers giving rise to a large intrinsic conductivity. It is also favorable to have a large bandgap which allows the temperature of a device to rise by a certain amount. On the other hand, high breakdown fields are also associated with large bandgaps.

But the most important reason for the dominance of Si is the processing technology developed around $SiO_2$, which can be formed on Si with remarkable ease and stability. No III-V compound has a surface oxide layer that compares to $SiO_2$ as an insulator, as a diffusion mask, and as a neutralizer of surface effects.

GaAs and III-V compounds therefore, can only have an impact in areas where Si can not compete: their larger bandgaps, higher breakdown fields, and higher mobilities make them attractive candidates for high performance microwave FETs, HBTs, lasers, detectors, and novel heterojunction devices. In the lucrative digital electronics and VLSI fields, however, GaAs is very unlikely to replace Si, since one or a few fast devices can not improve system performance. The speed of a digital system is determined by such things as delays in packaging (see Chapter 1). Low cost and high reproducibility are essential to a large system, and for that reason Si will not be replaced easily.

## § 4.3 Advantages of GaAs-on-Si

Having been called a "system designer's dream" and a "material scientist's nightmare," GaAs-on-Si is both bitter and sweet: its promises are so attractive, yet its problems so enormous. But first, we take a look at the positive side of it and list in the following several obvious advantages of GaAs-on-Si technology based on today's technology and our current understanding. There are certainly many more that one can include.

### Wafer size

GaAs wafers are currently available with diameters up to 3 inches. For many applications related to discrete devices, 3-inch wafers are large enough; however, LSI logic and memory applications require larger chips. Monolithic microwave integrated circuits (MMICs) are inherently large-area chips which should be processed on the largest possible wafers. The task of developing large size GaAs wafers is under way; however, the low thermal conductivity of GaAs imposes fundamental limitations on the wafer parameter without sacrificing crystal perfection. Si on the other hand is available in diameters up to 8 inches in high uniformity as well as purity.

### Wafer cost

At today's price, a 2-inch GaAs wafer can cost about $250, while a Si wafer of same size costs about $2, a difference of more than 100 times. For an epitaxially grown GaAs wafer, however, the cost of growth is much higher than that of the substrate. As a result, the use of GaAs-on-Si saves only a small fraction of the total wafer cost after epitaxy. For some applications such as MESFETs, the devices can be fabricated directly on a GaAs substrate by ion implantation without any epitaxial growth. In these cases, GaAs-on-Si is much more expensive because of the high cost of epilayer growth. As is often the case, significant savings of cost by using Si substrates can only be realized when the GaAs-on-Si technology can benefit from the use of larger Si wafer sizes unavailable in GaAs.

### Wafer strength

GaAs is much more fragile compared to Si. A standard comparison of semiconductor hardness shows that Si is about 50% stronger than GaAs. Hardness is a rough indication of the tendency of a wafer to break. A better measure is fracture strength. An analysis of wafer fracture strength shows that Si is 2.5 times more resistant to fracture. The handling losses during processing should be significantly reduced using GaAs-on-Si material.

### Wafer thermal conductivity

The thermal conductivity of Si is about 3 to 4 times better than that of GaAs. This is an advantage for heat dissipation in the operations of high-power FETs and lasers.

## § 4.4 Limitations of GaAs-on-Si

Current limitations of GaAs-on-Si are mainly due to the poor quality of the crystal growth. It is understandable that the crystal quality of GaAs deposited on Si will never be as good as single crystal GaAs. Experience accumulated over the past 4 years, however, shows that crystal perfection has greatly exceeded previous expectations considering the large mismatch in both lattice constants and thermal expansion coefficients. The quality of GaAs-on-Si has been steadily improved by new techniques and even better material is expected in the future.

### Thermal expansion mismatch

A serious problem for device application is wafer-bowing that results from different thermoelastic properties of GaAs and Si. On cooling from the epitaxial growth temperature of 720°C, the free contraction of GaAs is 2.6 times greater than that of Si. The postgrowth wafer is bowed with usually a concave GaAs surface and very high tensile stresses. Depending on the growth technique, the wafer bow may range from an acceptable 5 $\mu$m to greater than 50$\mu$m over a 2-inch wafer. In some cases as we have observed, the tensile stresses exceed the elastic limits of GaAs and resulted in surface cracks.

The extent of wafer bowing depends on the growth temperature, which should be minimized whenever possible. For a typical laser growth, the substrate temperature is as high as 720°C for AlGaAs, so alternative means have to be found to alleviate this problem. Recently, according to some unpublished early reports, researchers at NTT in Japan have used "modulated beam epitaxy" that deposits Ga and As layers alternately, to grow bowing-free GaAs-on-Si. Additional techniques such as growth on patterned substrate may be used to reduce bowing in future.

### Process incompatibilities

Difficulties are encountered in the processing of GaAs-on-Si devices when wafer cutting is required. GaAs cleaves preferentially along (110) planes while Si cleaves along (111) planes. A GaAs-on-Si laser, therefore will have additional problems due to the cleaving of two facets. If the two facets are not perfectly parallel, photon loss due to scatterings will be high. This problem, as will be shown later, can be minimized if the Si substrate is lapped down to a very small thickness. Techniques called "microcleaving" for on-wafer cleaving of GaAs lasers can be used to avoid the difficulty of cleaving Si along (110) planes.

## § 4.5 Current status of discrete devices and integrated circuits

Over the past few years most kinds of discrete microwave devices have been demonstrated in GaAs-on-Si. The more successful ones are the devices whose operations involve majority carriers. For example, GaAs field effect transistors (FETs) on Si. FETs are majority carrier devices and are not sensitive to defects in the crystal. This is why FETs were among the first devices fabricated in GaAs-on-Si with performances comparable to similar devices on GaAs substrates. They have the advantage of reduced wafer breakage due to the more robust Si wafer, reduction in substrate cost, and increased wafer size and yield. The best GaAs FET on Si has a 360mS/mm transconductance for a 0.25$\mu$m gate length, 55 GHz cutoff frequency, and a noise figure of 2.8dB at 18 GHz [5]. This is comparable to the best data on GaAs substrates.

Other such devices like modulation-doped field effect transistors (MODFETs) also known as HEMTs have also been reported with transconductances of 170ms/mm at room temperature and 275ms/mm at 77K for a 1$\mu$m gate length, and a gain cutoff frequencies as high as 23 GHz [6].

Heterojunction bipolar transistors (HBTs) are minority carrier devices, they are very sensitive to material defects. The first reported GaAs bipolar transistor on Si showed a current gain of 10, and current densities up to 105 kA/cm$^2$, and very good performances at microwave frequencies as high as 40 GHz have been reported [7]. Light emitting diodes (LEDs) are another minority carrier device that have been reported [8].

Solar cells [9] and focal plane arrays [10], as well as ring oscillators [11] have attracted much attention and have been reported.

### Lasers and optoelectronic integrated circuit applications

They are the main topics of the next chapter. Major breakthroughs and advances have been made in the past two years; many happened in this laboratory.

## § 4.6 Conclusions

In this chapter, we have presented both advantages and limitations of GaAs-on-Si technology based the limited experience, and summarized the short history this young research field has had. The GaAs-on-Si technology has already been used to fabricate most common microwave and optoelectronic devices with rather surprising successes. Future research in this field will overcome current technological barriers and push this promising technology to a state-of-the-art production stage for many exciting applications.

## § 4.7 References

[1] R. Houdre and H. Morkoç, in *CRC Critical Review*, 1988.

[2] T. Nonaka, M. Akiyama, Y. Kawarada, and K. Kaminishi, Japn. J. Appl. Phys. , **23**, L919(1984).

[3] H. Z. Chen, J. Paslaski, A. Yariv, and H. Morkoç, *Research and Development*, Jan. , 61(1988).

[4] J. Paslaski, H. Z. Chen, H. Morkoç, and A. Yariv, Appl. Phys. Lett. , **52**, 1410(1988).

[5] R. J. Fisher, N. Chand, W. F. Kopp, C. K. Peng, H. Morkoç, K. R. Gleason, and D. Scheitlin, IEEE Trans. Electron Devices, **ED – 33**, 206(1986).

[6] R. J. Fisher, T. Henderson, J. klem, W. T. Masselink, W. F. Kopp, H. Morkoç, and C. W. Litton, Electron. Lett. , **20**, 945(1984).

[7] R. J. Fisher, N. Chand, W. F. Kopp, H. Morkoç, L. P. Erickson, and R. Youngman, Appl. Phys. Lett. , **49**, 397(1985).

[8] R. M. Fletcher, D. K. Wagner, and J. M. Ballantyne, Mater. Res. Soc. Symp. Proc. , **25**, 417(1984).

[9] B-Y. Tsaur, J. C. C. Fan, G. W. Turner, F. M. Davis, and R. P. Gale, Proc. IEEE. Photovolt. Spec. Conf. , 1143(1982); J. C. C. Fan, B-Y. Tsaur, and B. J. Palm, Proc. 16th IEEE Photovolt. Spec. Conf. , 692(1982).

[10] R. C. Bean, K. R. Zanio, K. A. Hay, J. M. Wright, E. J. SAller, R. Fisher, and H. Morkoç, J. Vac. Sci. Technol. , **A4**, 2153(1986).

[11] H. Shichijo, J. W. Lee, W. V. McLevige, and A. H. Taddiken, Proceed. Int. Symp. GaAs and Related Compounds, Inst. Phys. Conf. Ser. , **83**, 489(1987).

# Chapter 5

## MBE Growth of GaAs-on-Si Quantum Well Lasers

### § 5.1 An introduction

The most attractive application of GaAs-on-Si material is the integration of the high-speed and optoelectronic properties of GaAs and the state-of-the-art processing technology of Si VLSI on a single chip. The high-speed on-chip GaAs lasers and detectors can increase the signal fan-in and fan-out (see Chapter 1) and interconnect a complex multi-chip supercomputer system.

The key to GaAs-on-Si optoelectronics is the quality of GaAs grown on Si. Currently, the quality of GaAs-on-Si is still low. A typical GaAs-on-Si crystal has a defect density of $N \approx 10^6\ cm^{-2}$ and surface tension of $\sigma \approx 10^8\ dyn\ cm^{-2}$, mainly due to the lattice constant mismatch between GaAs and Si. The high density of defects does *not* affect the performance of majority carrier devices such as FETs; however, it drastically degrades the performance of minority carrier devices such as lasers. For nearly 4 years, researchers worldwide have been working intensely to improve the electronic and optical quality of GaAs-on-Si, with the eventual goal of achieving the room temperature continuous wave (CW) operation of a GaAs-on-Si laser. The technological barriers have been the high density of defects in GaAs grown on Si. In this chapter, we will present the MBE growth of a single quantum well GRINSCH GaAs/AlGaAs laser on Si that achieved the world's first room temperature CW operation. Difficulties of GaAs-on-Si growth are discussed. Methods employed to overcome them are described in detail. After the CW operation, stripe geometry GaAs-on-Si lasers were fabricated and modulated by high frequency microwave signals. High-speed GaAs-on-Si p-i-n detectors were also grown with a similar procedure.

## § 5.2 Special problems associated with GaAs-on-Si growth

When a polar semiconductor (GaAs) is grown on a nonpolar semiconductor (Si), special problems arise which are not present in the conventional polar-on-polar heteroepitaxy growth. They are: (i) the problem of antiphase disorder on the polar (GaAs) side of the interface, (ii) the lack of electrical neutrality at the interface, and (iii) the problem of cross-doping. In addition, the large difference in thermal expansion coefficient and lattice constant mismatch which are not related to polar-on-nonpolar semiconductor growth can cause other severe problems.

### Antiphase disorder

Si has a diamond structure which consists of two interpenetrating face-centered cubic Bravais lattices. GaAs has a similar crystal structure, except the two face-centered cubic lattices are not the same; the first one is occupied by Ga atoms, and second one by As atoms. Because the Si lattice is occupied by only one type of atom, the crystal is invariant to a $\pi/2$ rotation along $(100)$ and the $(011)$ and $(01\bar{1})$ directions are equivalent. However, this is not so for GaAs. Therefore, when the growth of GaAs-on-Si is started, the orientation of GaAs (there are two orientations possible) is not completely defined for the entire wafer but may be defined locally in some small domains which are known as antiphase domains (APDs). Antiphase boundaries (APBs) occur when these small regions with defined orientations $\pi/2$ different, are joined (**Figure 5.1**).

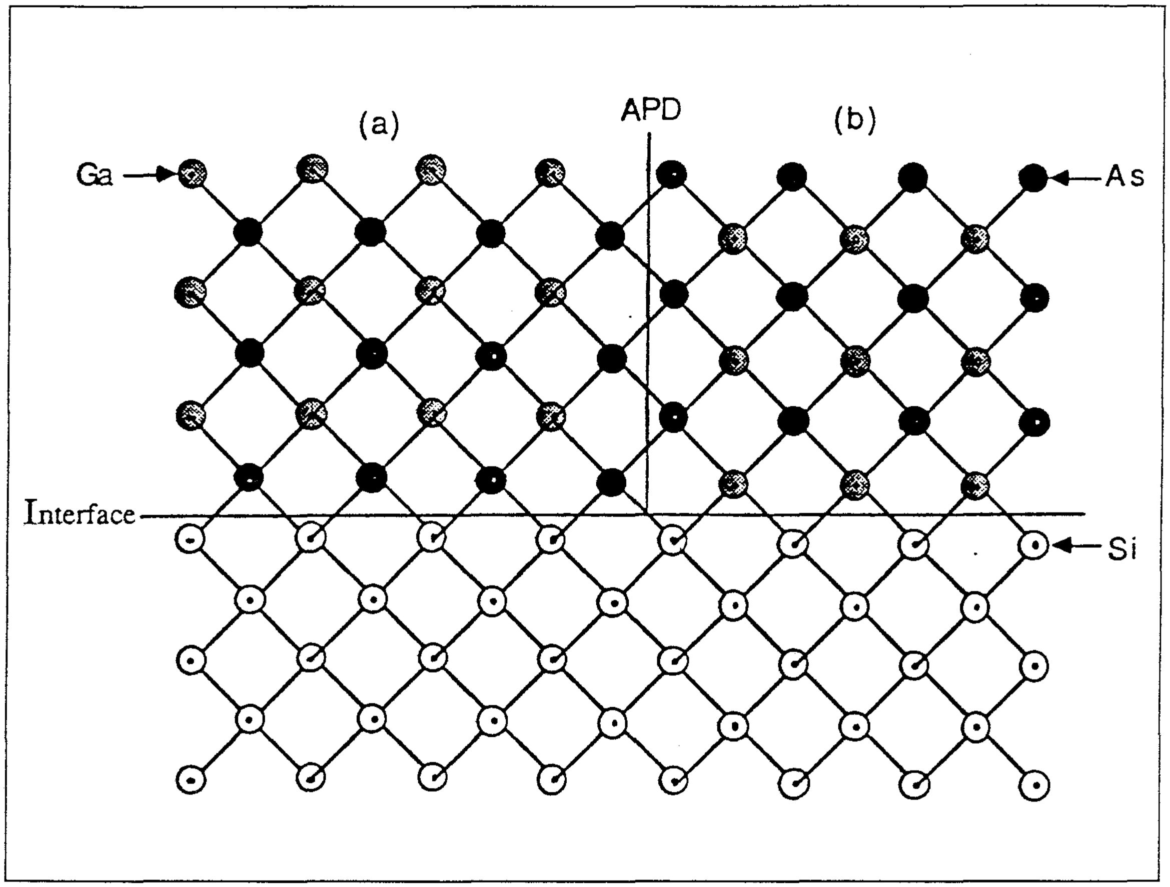

**Figure 5.1** *Schematic drawing the antiphase domain boundary formed by two regions with (a) an As prelayer and (b) a Ga prelayer.*

Microscopically, on an exact (100) Si substrate, there is no distinction between Ga and As sites and the first monolayer may be randomly occupied by Ga and As atoms. A (100) GaAs is a crystal with alternating Ga and As planes. Therefore, the growth may begin in some regions of the interface with a Ga plane, and in others with an As plane. When this happens randomly, we get high defects of antiphase boundary disorder.

### Electrical neutrality

When both types of domains meet, massive Ga-Ga (or As-As) bonds are created, which are electrically charged and can act as acceptors (or donors).

## Step-doubling and substrate misorientation

Moreover, a real (100) Si surface will always contain atomic steps, and the steps with an *odd number* of atomic layers will confuse the distinction between Ga and As sublattices and then induce APD even if the first atomic plane is occupied by only one type of atom. Fortunately, most steps on (100) Si surface appear to be double steps [4] after the substrate is heated to 1100°C before the growth is started.

## APD free growth of GaAs-on-Si

Numerous studies [3,5,6] indicate that APD is the result of (i) a nonuniform coverage of the first monolayer, and (ii) single (odd number) steps at the Si surface. Therefore, it has been proposed [5] that (i) a uniform coverage with an As (or Ga) prelayer be used, and (ii) tilted substrates which are known to have double steps be used. Using these techniques, APD free (100) GaAs has been grown [6]. All of our laser structures have been grown this way. Qualitatively, an arsenic prelayer helps the crystal define its orientation while double steps eliminate possible confusion resulting from odd numbers of steps. But even if the above conditions cannot be satisfied everywhere on (100) Si surface at the beginning of growth, a subsequent slow growth of a transition layer will allow different islands to form, which will intercross and finally grow into one bulk material. There is still, however, no agreement among experts on a quantitative microscopic theory that can explain the strange behavior of transition layer growth which strongly depends on several parameters [7].

## Thermal expansion mismatch

The problem with the difference in thermal expansion coefficients is of intrinsic nature and the only thing we can do is to reduce its effects. One obvious scheme is called "selective area growth," where GaAs is grown on certain isolated areas so that thermal mismatch can be confined to small isolated regions instead of entire wafer. Gradual cooling after the growth is finished is also important. Samples suddenly cooled from 720°C to room temperature often have surface cracks visible under an optical microscope. This problem is potentially serious for long lifetime optoelectronic devices such as lasers and has not been studied carefully.

### Lattice constant mismatch

The 4.1% lattice mismatch requires one type I dislocation for every 25 atomic planes and one type II dislocation for every 18 atomic planes (type I,II dislocations are discussed later). This results in a dislocation density of $10^{12} cm^{-2}$, which is much higher than the practical limit of $10^{4}\mathrm{cm}^{-2}$ which devices can tolerate. To find effective techniques for dislocation density reduction, we must have a good understanding of the nature of these defects. Generally, it is known that there are two ways an epitaxial layer can accommodate a lattice mismatch with the substrate: by introducing strains, and by introducing dislocations. In the first case, the lattice mismatch is accommodated by an elastic deformation of the lattice; however, for GaAs-on-Si system, the critical thickness of GaAs layer is 50 Å [2], and beyond which, the strain energy which is proportional to the thickness of the layer becomes larger than the minimum energy to generate dislocations. In practice, we are always in the second case: dislocations have to be generated to account for the large lattice mismatch. Therefore, *the best we can do* is to confine these dislocations to the GaAs/Si interface so that they will not affect the device operations several microns away from the interface.

Several popular methods have been used to reduce the effect of dislocations. Their main goal is to confine mismatch dislocations to the interface and prevent them from transforming to threading dislocations that will travel through the later growth.

### Substrate misorientation

The two types of misfit dislocations type I and type II that we mentioned earlier have been studied experimentally [8]. The main conclusions are that the type I dislocations are inactive sources for generation of threading dislocations because their

Burgers vectors lie in the (100) plane and are parallel to (011) and (01$\bar{1}$) directions, and the type II dislocations on the other hand, can move through the crystal by gliding along the (110) planes since their Burgers vectors are inclined from the interface by 45° (**Figure 5.2**). The type II dislocations are therefore highly active sources for the generation of threading dislocations which are harmful to device operations. Therefore the goal is to increase the fraction of type I dislocations in the misfit dislocation network and effectively reduce the fraction of type II active sources for the generation of threading dislocations.

In practice, this is accomplished by using a substrate tilt. It has been known [8] that steps at Si surface preferentially induce type I dislocations. Thus it has been suggested [5,9] that a tilted substrate with one step every 25 atomic planes be used. The angle of such tilt is 1.6° for (100) tilted toward (011), and (011) being the direction that the steps run along. If the substrate is tilted toward (001) then the angle would be 2.3°. **Figure 5.3** shows a staircased Si surface with atomic steps. It has been proposed and demonstrated [5,9] that a slightly larger substrate tilt, 4° from (100) toward (011), is more effective. This is because on a *real* Si surface, the steps do not occur at regular intervals. The slightly larger tilt can make sure that there are very few intervals between two steps larger than 25 atomic planes. Using this technique, dislocation density has been greatly reduced to as low as $10^5 cm^{-2}$ to the mid-$10^4 cm^{-2}$ range. This technique has been used throughout our research on GaAs-on-Si devices.

## Strained layer superlattice

GaAs/InGaAs strain layer superlattice (SLS) structures have been successfully used to bend the dislocations [5,9]. The direction of the bending depends on the sign of strain. The use of a material with a larger lattice constant will induce a compressive strain in this layer, which will tend to repulse the dislocations from the strain superlattice.

We have experimented with GaAs/InGaAs strain layer superlattice in the buffer

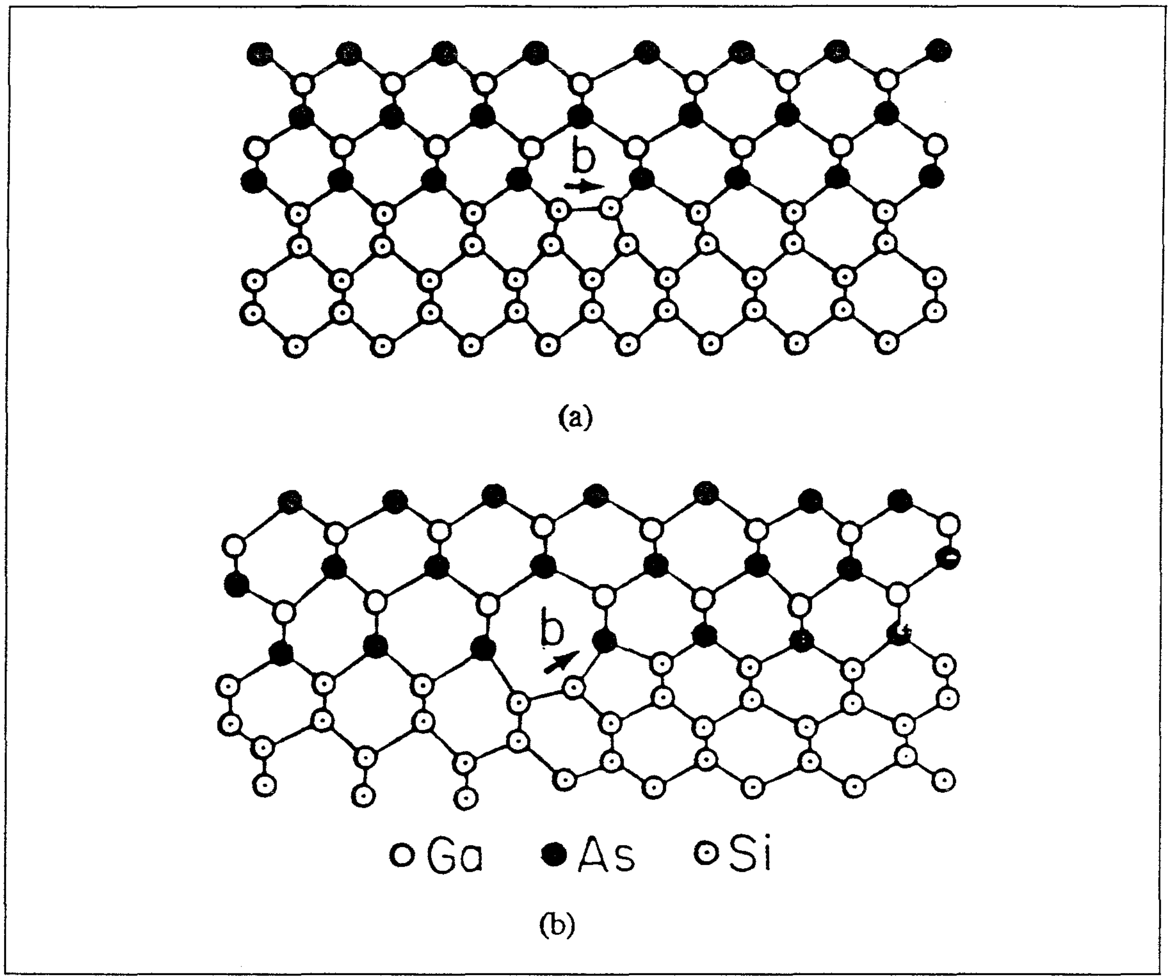

**Figure 5.2** *Schematic drawing of (a) the type I misfit dislocation with the Burgers vector parallel to (100) and (b) the type II misfit dislocation with the Burgers vector inclined from (100) by an angle of 45°.*

layer. Thus far, the results are inconclusive.

## Rapid thermal annealing

Once the laser structure is grown, ex-situ annealing can be performed. If done properly, it can reduce the density of dislocations dramatically. Annealing experiments have been done by several groups and they all report an improvement in the quality of GaAs epitaxial layer [10]. The ex-situ thermal annealing performed on our samples are done at 850°C under an inert gas. The annealed lasers showed no delay in the light

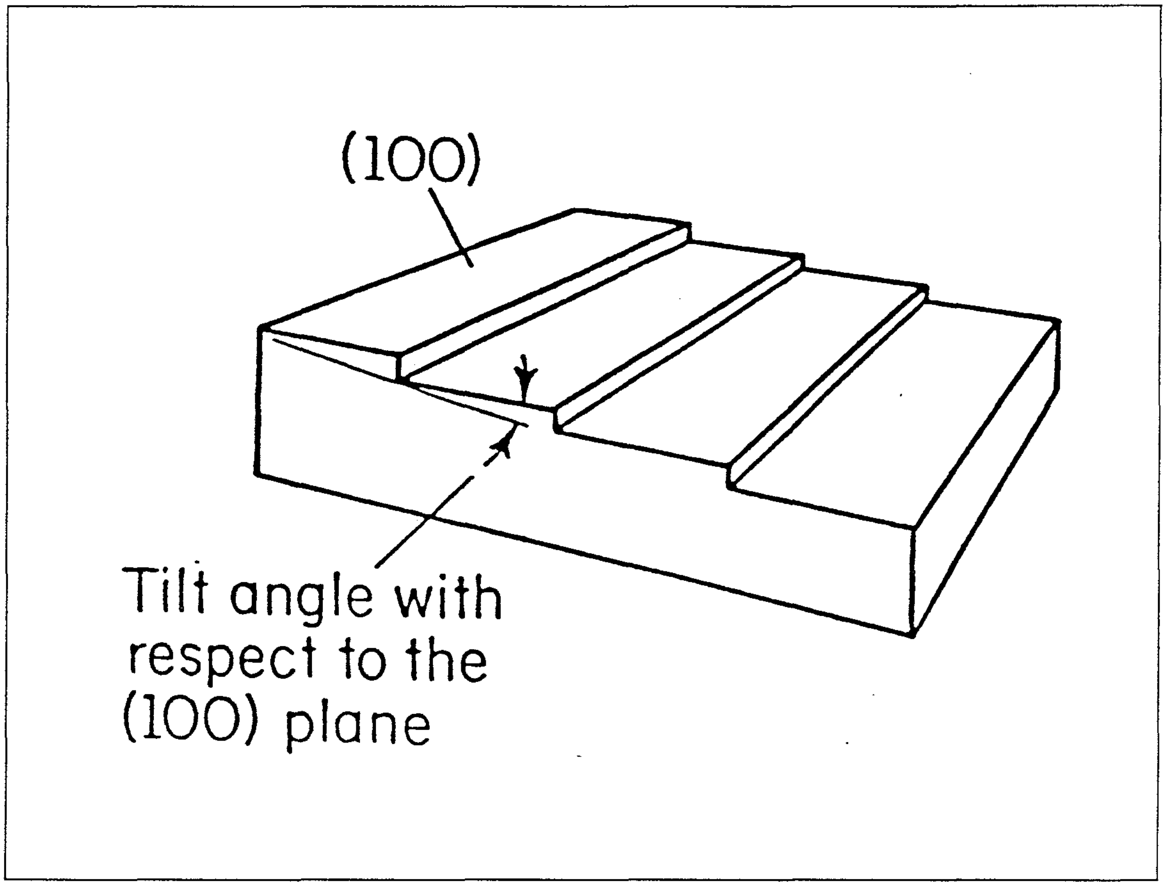

**Figure 5.3** *Schematic drawing of a (100) substrate tilted toward (011).*

response when pumped with electrical pulses (usually a turn-on delay typically of 10-50 ns is observed indicating the presence of defects which must be saturated first by the initial pump pulse). This is a noticeable improvement over the unannealed samples for which a delay of light response is common.

## § 5.3 Substrate preparation

Before GaAs can be grown on Si, a clean Si surface in a ultra-high vacuum MBE environment is required. Classical chemical cleaning techniques of Si often produce a surface with carbon (C) and oxygen (O) contaminants. The oxygen on the surface can be thermally removed by heating the Si substrate to 900 - 1000°C, but the carbon can only be removed partially at 1200°C, which is too high for a standard MBE system where the maximum substrate temperature is limited to 900°C. Moreover, the carbon may react with the Si substrate at 800°C forming SiC. The presence of SiC on the surface is known to have a catastrophic effect on epitaxial growth on Si. These considerations require a surface preparation procedure that can remove the carbon on the surface, and can produce a thin protective layer that can easily be removed inside MBE. This protective layer can also prevent carbon contamination by air during the loading process.

The cleaning procedure we have been using was invented by R.C. Henderson [1] and modified by H. Morkoç [2]: (i) degreasing and removal of a native oxide layer on the surface, (ii) several iterations of growing and stripping of a chemical oxide layer. During this step, any contamination (including C) at the surface will be buried in the oxide layer which is then removed by a subsequent stripping, and (iii) the growth of a thin and volatile oxide layer that will be easily desorbed by heating the substrate inside the MBE's growth chamber. The details of this cleaning procedure are listed in **Appendix V.**

After the cleaning, the substrate is mounted onto a homemade Mo block for direct radiation heating. The mounted substrate is then loaded into the loading chamber of the MBE system where the substrate is gradually heated to 900-1000°C for 2 minutes for oxide desorption. Next, the substrate is transferred to the growth chamber of the MBE system, and the substrate is heated up to about 900°C again, to anneal the surface damage and blow off any impurity condensation on the surface during the transfer. Finally, the substrate is cooled down to an appropriate initial growth temperature to be discussed later. After this oxide desorption and thermal treatment, a clear (2×1) RHEED pattern can be observed, which indicates a clean Si surface with a standard reconstruction.

## § 5.4 Transition layer growth

First, to prevent the antiphase domains when the growth is attempted on a (100) Si surface, it is started with an As preexposure. This is done at the beginning of the growth by opening the As shutter for a sufficiently long time until the Si surface is completely covered by a few monolayers of As atoms. Should a Ga prelayer be used? No. This is because an As prelayer is energetically favored. If a Ga prelayer is put on Si, then As atoms next deposited on top of Ga would always get under the Ga layer and make bonds to Si.

After the preexposure is done, the substrate is exposed to both Ga and As fluxes and the normal growth is started. The As pressure for preexposure as well as for growth should be $P_{As_4} = 1 \times 10^{-7}$ torr using a conventional cell, or $P_{As_2} = 1 \times 10^{-8}$ torr using a cracker cell. At this pressure, a 5 second preexposure of As is enough. It has been discovered experimentally that $As_2$ has a higher sticking coefficient to Si surface, and it can tolerate a higher starting substrate temperature. According to our extensive experience, to obtain a As prelayer, a temperature lower than 200°C is required for an $As_4$ source and a temperature as high as 400°C can be used for an $As_2$ cracker cell.

The growth rate of GaAs in the very beginning is kept lower than $0.1\mu$m/h since the newly grown crystal needs some time to find the best arrangement, or to minimize the free energy, so to speak. A very important trick is that whenever the GaAs growth becomes bad on the RHEED screen, Ga cell temperature should be lowered to let the growth recover. This has been used often in the early stage of a GaAs-on-Si growth.

During this transition layer growth, the RHEED pattern will change from very spotty to streaky. A spotty pattern (typically seen in small angle X-ray scatterings of powdered 3D specimen) indicates a three-dimensional type of growth, and a streaky RHEED pattern (which represents a 2D surface reconstruction, see Chapter 4) is associated with a standard two-dimensional GaAs surface reconstruction. The substrate temperature during this growth is gradually raised to a standard growth temperature of 580°C which normally gives a $1\mu$m/h GaAs growth rate. To obtain good surface morphology, the time of the transition layer growth can be as long as two hours although this period should be as short as possible, since low temperature growth of GaAs is known to have poor optical and especially poor electrical quality. There is a tradeoff between the arsenic sticking coefficient and the quality of the transition layer: a low starting temperature is required for a good arsenic sticking on Si substrate, and a high growth temperature is needed for high crystal quality. To accomplish both, the growth should be initiated at a low substrate temperature at about 200°C, and immediately after the first 1000 Å of growth, the substrate temperature is raised to 580°C. The cell temperatures of Ga and Si are also raised, gradually following the increase of substrate temperature. When the substrate reaches 580°C, the Ga cell temperature is set to what should give a $1\mu$m/h growth rate.

The thickness of the transition layer grown at a slow rate and at a low substrate temperature is usually between 250-2500 Å. This is a layer of amorphous material which can be annealed to become crystalline (hopefully) at 580°C. Because this transition layer is of low quality, the defect density is usually high. As a result, the doping level in this layer can be effectively reduced as we have experienced. What should be an $n^+$ GaAs doping level has produced rather low doping and becomes $n^-$. Furthermore, a large voltage drop across this layer sometimes as large as 10 V, compared to an expected 1.5 V has been observed in current-voltage (I-V) measurement. Use of a "cracker cell" can help solve this problem since the starting growth temperature is above 400°C and can quickly be raised to 580°C, thus making the transition layer very thin and the voltage drop very small. Also, the quality of GaAs grown at $T_s$ between 400 - 580°C is much better than material grown between 200 - 580°C.

At this point, there seem to be three key elements to a successful transition layer growth: (i) a sufficiently long As exposure before Ga shutter is opened, (ii) gradual rise in Ga and dopant cell temperature, and (iii) bringing the substrate temperature to 600°C as soon as possible.

## § 5.5 Room temperature CW operation of GaAs-on-Si lasers

It has been long established that room temperature continuous wave (CW) operation of a GaAs-on-Si current injection laser is a very important step toward eventual realization of commercial OEICs of GaAs-on-Si. For several years, researchers worldwide have been actively seeking ways to obtain at first low-threshold pulsed operations of GaAs-on-Si lasers, and eventually CW operations. What is described in the following is an account of the most important research contribution of this thesis project.

### First step: low-threshold current density pulsed operations

By mid-1987, the lowest threshold current density obtained in a GaAs-on-Si laser under pulsed operation was 3500A/cm$^2$ [11]. This was mainly due to the poor quality of epitaxial growth of GaAs-on-Si. It was obvious that a significant reduction was needed to achieve room temperature continuous wave operations.

Before the work of GaAs-on-Si was started, the growth conditions of GaAs-on-GaAs lasers had been optimized by us to such an extent that we could successfully grow GaAs-on-GaAs GRINSCH lasers with threshold current densities as low as 140 A/cm$^2$ regularly.

The work of GaAs-on-Si, however, was more complicated. First, we had to modify the Mo blocks used for indium mounting for direct heating of Si substrates, because indium-free mounting allows a quick flash of Si substrate at 900°C for oxide desorption, which can not be done with indium mounting (indium evaporates at 900°C and the substrate will separate from the mounting block and drop). This was done by opening a large hole in the middle of a conventional Mo block, of roughly the size of a 2 inch

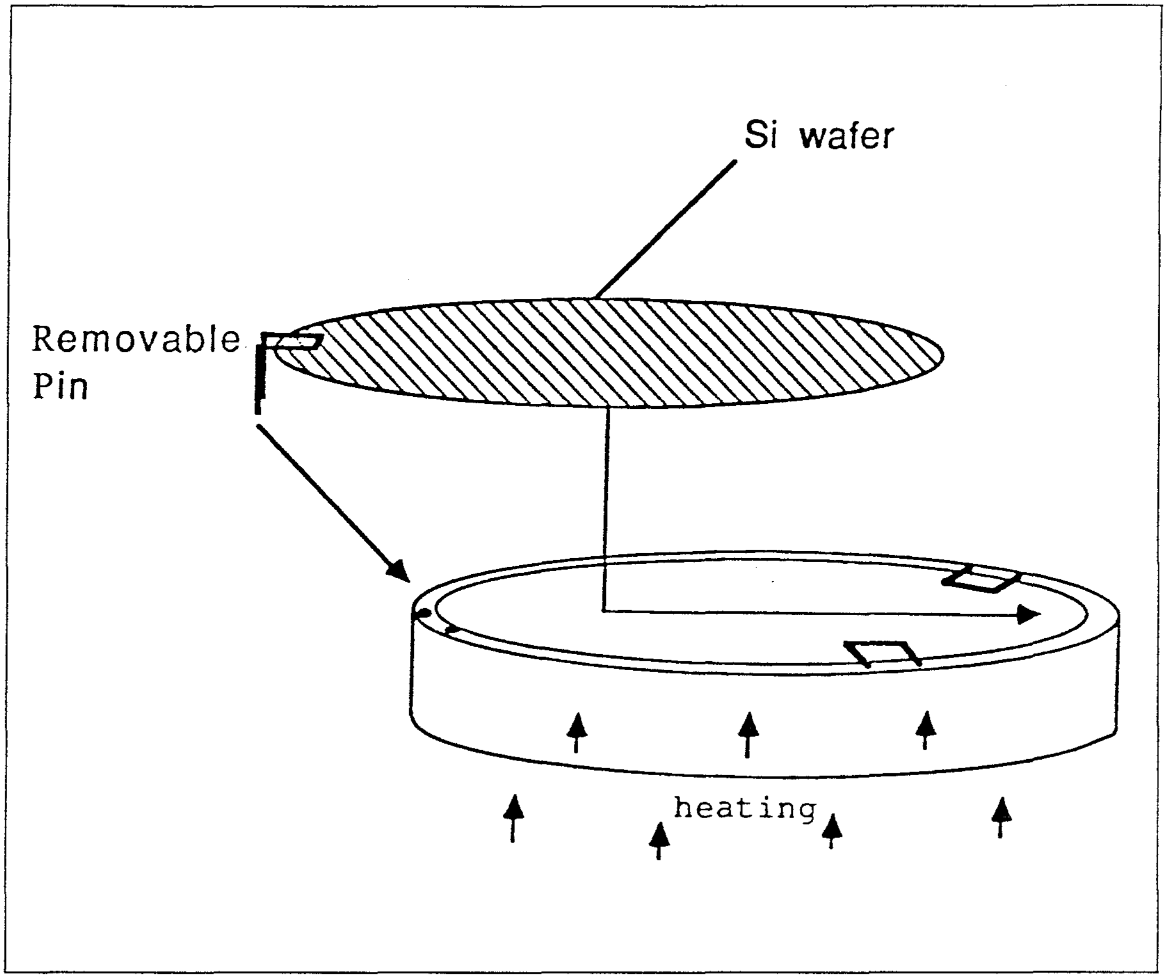

**Figure 5.4** *The indium-free mounting used in the GaAs-on-Si growth.*

Si wafer. Three pins made of tantalum wires were used to clip down the wafer to the now O-ring-shaped Mo block (**Figure 5.4**), with one of them removable after each use.

Inside the MBE's growth chamber, the heating filaments on the sample manipulator can radiate directly toward a Si substrate. This heating method has the distinct advantage over the conventional In mounting heating method where heat is transferred by liquid In on contact, and as a result, the substrate temperature can be changed rapidly.

It was pointed out in Chapter 4 that the quality of AlGaAs growth depends on the substrate temperature, preferably at 720°C. With direct heating, this can easily be accomplished since it takes less than 10 seconds to raise the substrate temperature from 600°C to 720°C, compared with In mounting which requires as long as 2 minutes due to the large thermal capacity of the Mo block material plus an In layer between the heating pads and the substrate. This heating scheme is not only essential for GaAs-on-Si growth, but also good for GaAs-on-GaAs growth.

The starting growth temperature for the first few successful low-threshold lasers was about 300-400°C, which was followed by a 5-second As preexposure. These lasers were used to demonstrate low-threshold current density, and one of them was used to perform CW operation at room temperature.

Later, we have found that with an $As_4$ source and a lower starting temperature (200°C), an O-ring on the edge of wafer (**Figure 5.5**) can be observed. This is because the direct heating allows the middle portion of the wafer facing the heating pads to cool down quickly to 200°C, while the area on the outside not facing the heating pads cools down slowly with the Mo block. Since As atoms only stick to the cooled area (at 200°C), an O-ring is formed which is the boundary between the As-prelayered region in the middle and the (Ga,As)-mixture prelayered region on the outside. The GaAs inside O-ring is also APD free and outside O-ring is APD prone. With an $As_2$ source, however, such an O-ring is not observed since $As_2$ can stick to a surface at a higher temperature. All of the successful GaAs-on-Si wafers grown had the above feature.

Furthermore, the lowest threshold current density reported prior to our work had been 3500 A/cm$^2$, and our lasers achieved a threshold current density as low as 600 A/cm$^2$ [12] almost 6 times lower. **Figure 5.6** shows the light vs. current relationship of lasers made using two cavity lengths. Curve A represents a $(120\mu m \times 520\mu m)$ laser with $I_{th} = 0.6A$ and curve B represents a $(120\mu m \times 1210\mu m)$ laser with $I_{th} = 0.87A$. A threshold current density of $J_{th}^{B} \approx 600A/cm^2$ was obtained, which indicated for the first

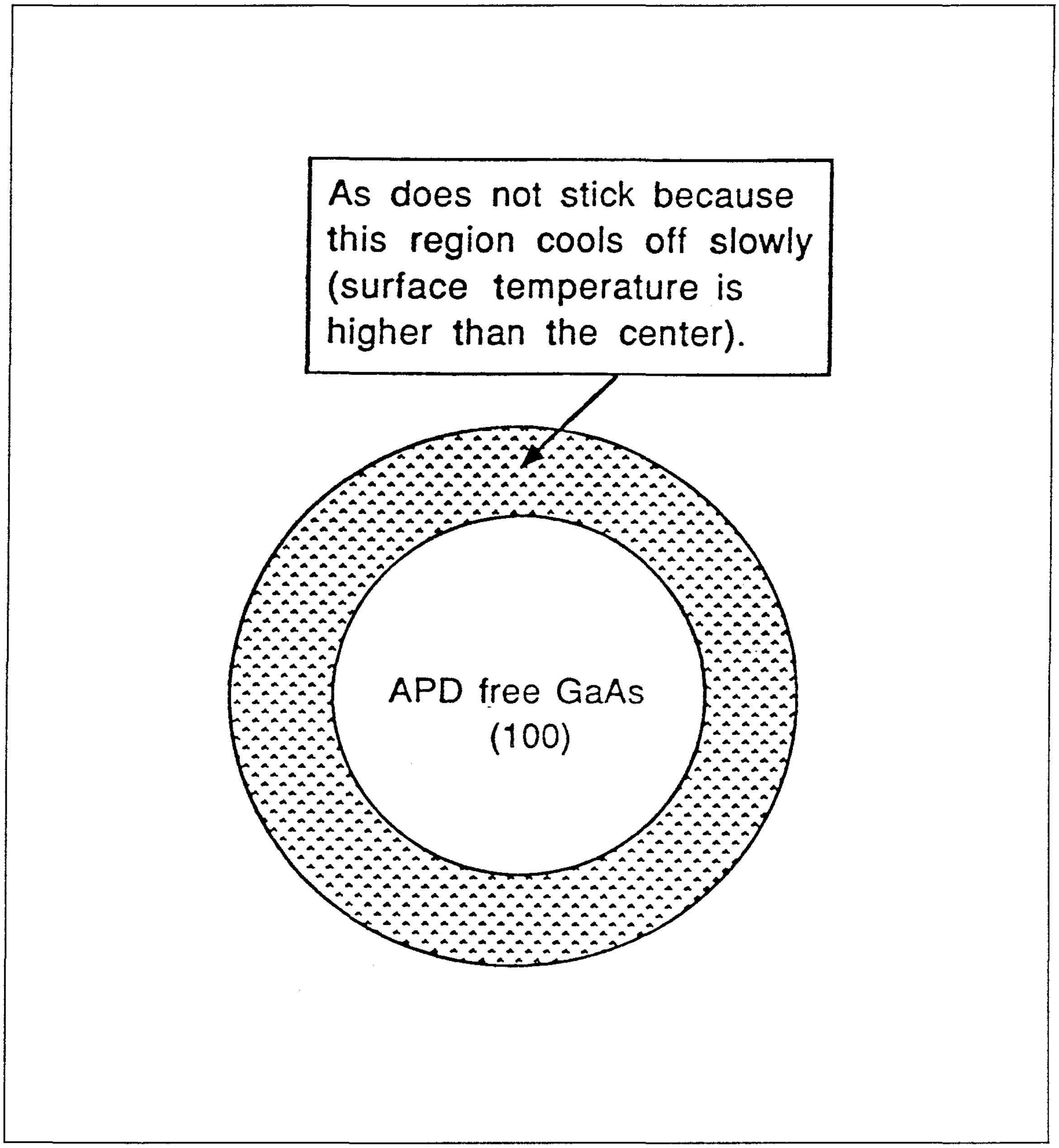

**Figure 5.5** *The effect of growth temperature on As sticking coefficient and surface morphology shown on a finished growth. The center region is APD free and has good morphology but the outside ring contains a high density of APD related defects.*

time that high device-quality GaAs can be grown on a Si substrate.

Until this time we did not seriously think that CW operation was possible. There

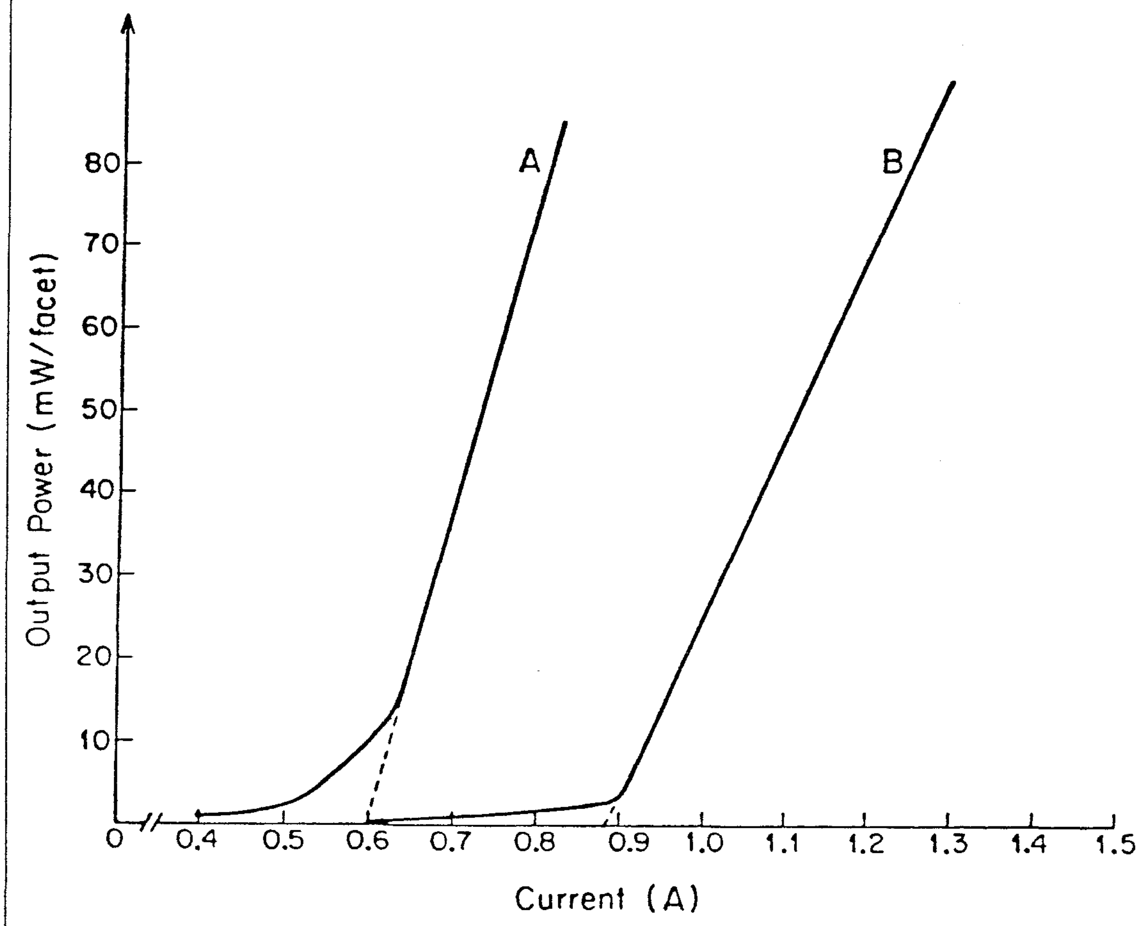

**Figure 5.6** *The light versus current characteristics for two low-threshold GaAs-on-Si broad area lasers. Both exhibited threshold current density of 600 A/cm$^2$.*

were, however, some other very difficult technical problems to overcome even after achieving a low threshold current.

## Second step: Room temperature continuous wave operation

Several very good GaAs-on-Si samples were grown by MBE shortly afterwards.

Threshold current densities as low as 214 A/cm$^2$ were obtained from one of them. Historically, the first GaAs-on-GaAs CW laser had a threshold current density of $1.6\times10^3$A/cm$^2$ [13] which is several times higher than our GaAs-on-Si result. A CW operation of GaAs-on-Si laser thus appeared possible.

The first question is what kind of laser device should be attempted in CW operation. A laser with proton-bombardment-defined stripe was used in the first CW operation of GaAs-on-GaAs lasers. Such a device is easy to fabricate and was chosen for our first attempt. Unfortunately, we were unable to achieve any CW operation. The failure was mainly due to the damage incurred during device processing, and the difficulty in making good thermal contact to a heatsink. In addition, the stripe laser exhibited a much higher threshold current density than that of the broad area devices, and as a result, the heat dissipation per unit area is much higher. Therefore, we decided that a broad area laser would be used to accomplish CW operation. The difficulty with a broad area laser, is that we have to make uniform thermal contact over the entire area.

Having decided the type of laser device to be used, we focused our attention on other technical problems. First, unless we could solve the problem of lapping and cleaving we would not obtain low-threshold lasers for CW operations. The problem with lapping occurs when a wafer is being removed from a lapping block. The removal involves heating up the lapping block to melt the wax used to attach the wafer. This will cause a large wafer-bow due to the large difference in thermal expansion coefficients. In addition, the difference in thickness between GaAs epilayer (a few $\mu$m) and Si substrate (about 100 $\mu$m thick) causes bowing of the entire wafer visible by the naked eye. When this happens, the two cleaved facets are not parallel and the photon loss in the cavity is very high. In the worst case, the wafer is bowed to a degree that further processing is impossible. The solution was to soak the entire lapping block with the wafer in acetone solution, so that the wafer could come off the block by itself with the disassociation of wax. Next, we were faced with the problem of cleaving, which is caused by the fact that GaAs cleaves along (110) and Si cleaves along (111). To obtain a good alignment of two cleaved facets, it is important to lap the wafer as thin as possible. The cleaving should be done in such a way that the knife-edge used in cleaving is as close to the center of the piece of wafer as possible for a symmetric breakage.

After the fabrication, we were faced with the very difficult problem of mounting the laser with the substrate side up on a heatsink for heat dissipation through thermal contact (the distance between the p-n junction and the heat sink is only 2.5 $\mu m$ compared to 100 $\mu m$ in the substrate down mounting). At first, lapped copper blocks were used, but this did not work because the copper blocks used were not smooth enough and copper was not sufficiently good a heat conductor. At one point, the laser did operate CW, but the lifetime was not long enough for recording.

Finally heatsink squares made of industrial diamond were ordered whose thermal conductivity is 3 times better than that of copper. The mounting scheme was the following: (i) mount a piece of diamond on a copper block using an indium alloy that has a high melting point around 400°C, and (ii) then mount the laser chip upside down on the diamond with a low melting point indium alloy around 200°C. The amount of indium on the diamond surface is important since excessive indium will flow and short the p-n junction of the laser which is only 2.5 $\mu$m away from the mounting surface. Too little indium will leave gaps in the indium underneath the laser where heat can not be removed and can cause burning when CW operation is attempted.

The actual attempt to obtain CW operation was hampered by the unsuccessful effort in mounting. This tedious task lasted about three weeks without success, until one day when everything was just right and we finally achieved the first CW operation.

The first CW operation is shown in **Figure 5.7**, which was operated for 5 minutes. The operation was stopped to preserve this first CW laser as a souvenir. A light-current characteristic is shown in **Figure 5.8**. The laser that was operated CW has an surface area of 120×980 $\mu m^2$ and has a threshold current of 350 mA. It lased at a wavelength of 8630 Å. This was the first CW operation ever obtained, and it was reported at the GaAs-on-Si Workshop in Marina del Rey on June, 18, 1987, in California [14]. Until this time no current-injected room temperature CW operation had been reported, although there has been report of optically pumped CW operation without a p-n junction.

Later, we improved and perfected the mounting method (**Figure 5.9**). Its details are given in the following: first, mount the diamond on the copper block as described before; then put a drop of rosin-based solder flux on the diamond, the size of the flux being large enough to cover the entire diamond. Next, a very small indium ball (they are commercially available from Indium Corporation of America) is dropped into the flux and placed at the center of the diamond heatsink. A cleaved single laser can then be dropped onto the flux carefully. It should stay on the center top of the flux. The entire (laser chip + diamond heatsink + copper block) stack is then heated up slowly. The flux will become more fluid and the laser chip will come down slowly as a result of gravity. The laser makes contact to the indium ball sitting inside the flux, and when the temperature is high enough, the indium ball melts into a small pool covering the entire diamond surface. Down with the indium ball comes the laser chip onto the diamond, which makes a good thermal contact to the diamond through a very thin layer of In. No gap exists between the chip and diamond since there is no air in the flux drop. The entire mounted block is then removed from heat. After it cools down, it is put in acetone solution to remove the flux on the facets (mirrors).

After the success of CW operation, several other characteristics were measured to obtain a complete picture of the GaAs-on-Si laser.

### Polarization of laser emission

It has been speculated (unpublished results among some researchers) that the po-

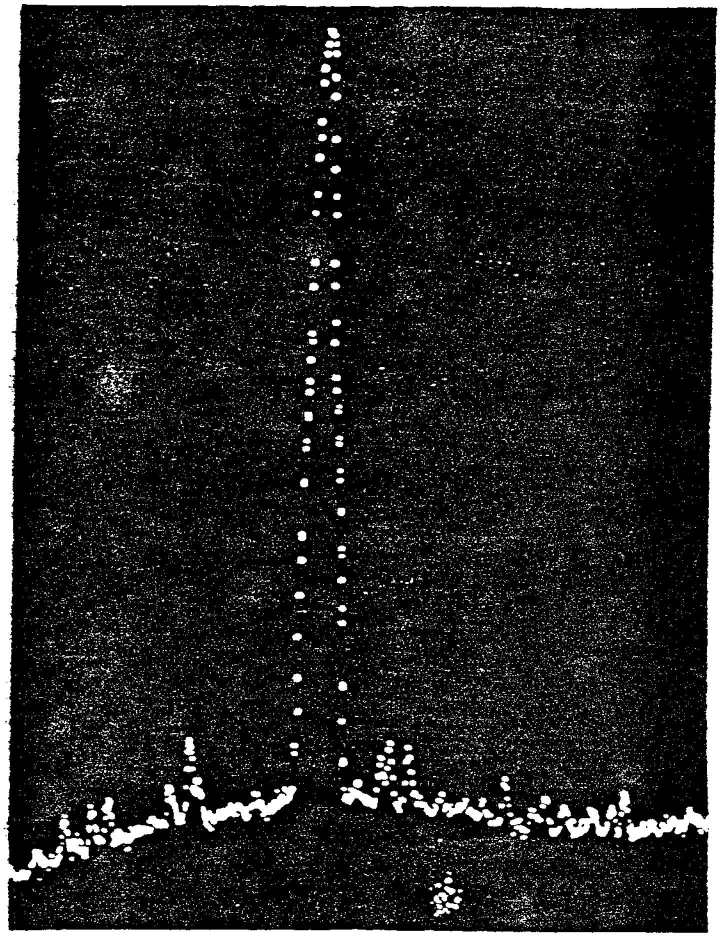

**Figure 5.7** *A photograph of the first room temperature, current-injected, continuous wave (CW) operation in a broad area GaAs-on-Si laser. The center frequency is 8630 Å,and the horizontal scale is 100 Å. The quantum well width $L_z$ is 125 Å. It was operated CW for 5 minutes and had a threshold current of 350 mA for an area of* $120 \times 980 \mu m^2$.

larization of light from a GaAs-on-Si laser consists of both transverse electric (TE) and transverse magnetic (TM) field modes due to the strain induced by the residual lattice and thermal mismatch. To investigate this, we have measured the polarization of light

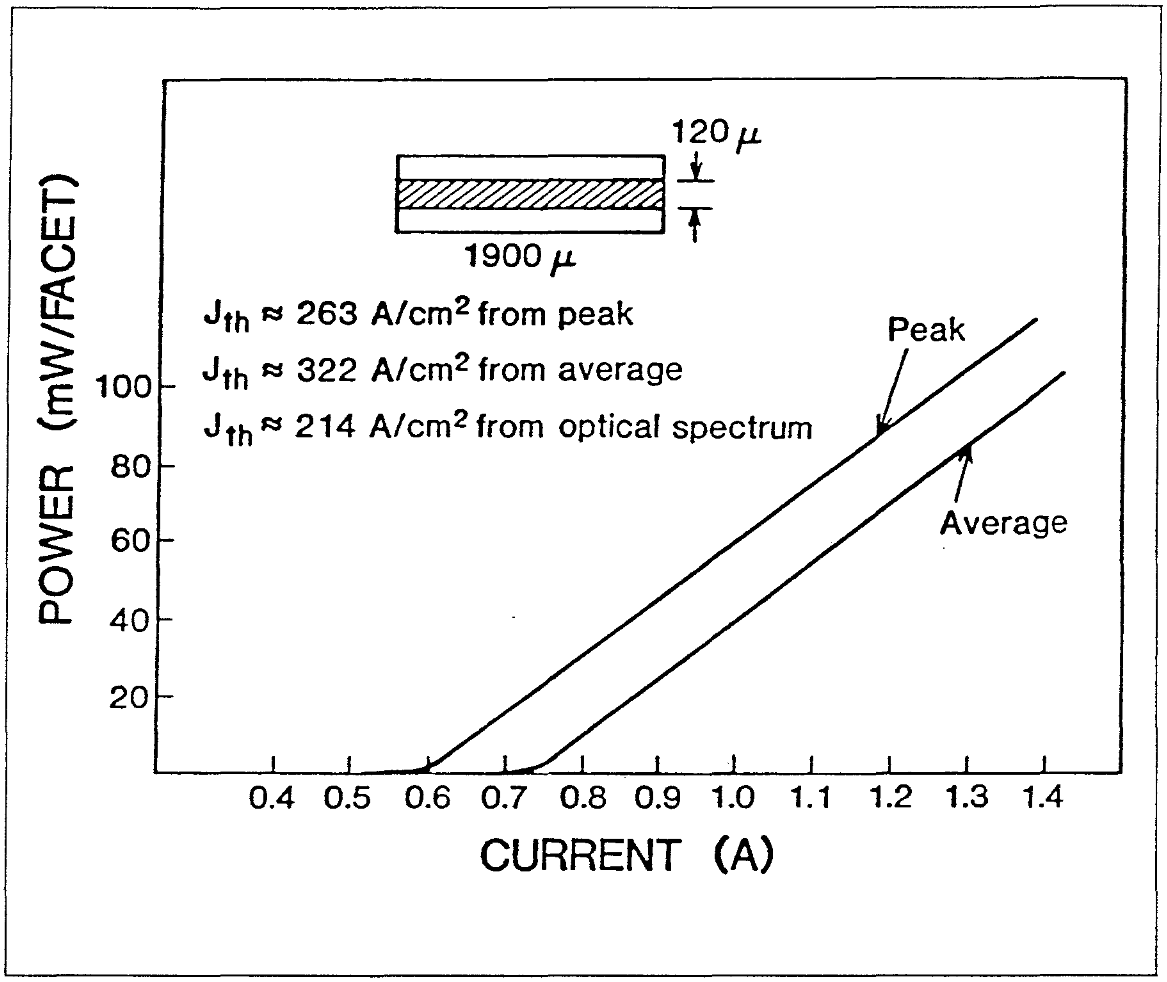

**Figure 5.8** *The light versus current curve of a CW broad area GaAs-on-Si laser that exhibited the lowest threshold current density of 214 A/cm*$^2$.

from two lasers with very large thermal and lattice mismatch that resulted in some visible surface cracks. In one case, the cracks were running perpendicular to the laser cavity, in the other case, the cracks were running parallel to the cavity. A polarizer was inserted between the laser and a monochrometer which can pass either one of the two polarizations at a time. The polarization resolved spectra for both lasers are shown in **Figure 5.10** and **Figure 5.11**. The measurement did not confirm the existence of any TM mode.

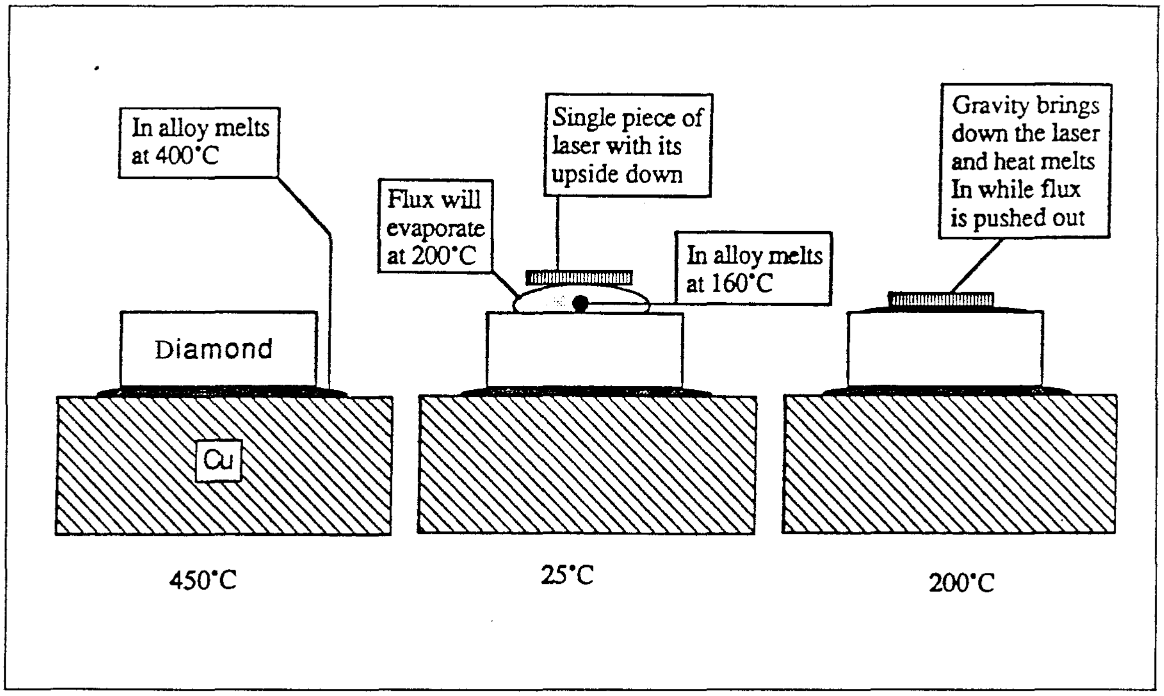

**Figure 5.9** *A better mounting method of a laser onto a heatsink. This is used in industry presently.*

This study, however, shed some light on the apparent effect of strain on mode selection. In the laser with surface cracks perpendicular to the cavity, the spectral lines are centered around 8700 Å( 1.425 eV ), much like a typical GaAs-on-GaAs laser except some very weak modes at higher energy around 1.48 eV. In the laser with surface cracks running parallel to the cavity, the spectrum is much different and consists of peaks of comparable strength centered around 1.425 eV and 1.48 eV. All of the above are TE modes. This is consistent with the fact that the mirror reflectivity of TE polarized light is always higher than that of TM polarized, because the boundary conditions imply that the light polarized perpendicular to the plane of incidence (TE) always has higher reflectivity. A TE mode therefore, suffers lower mirror losses. At this time, we attribute the observed difference in the lasing spectrum to the effect of strain on the gain coefficient [15].

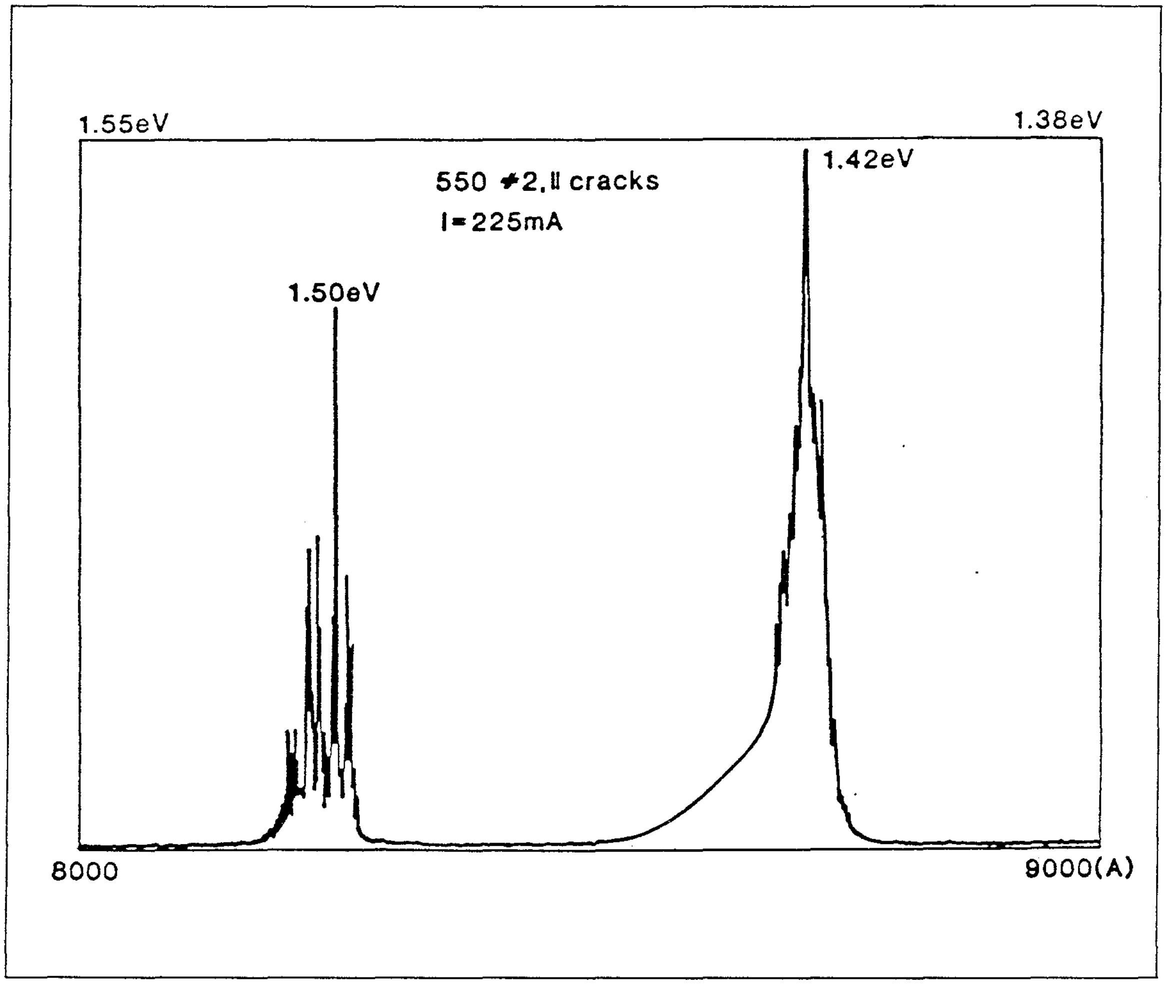

**Figure 5.10** *The optical spectrum obtained for a GaAs-on-Si stripe laser with surface cracks parallel to laser cavity.*

## Near and far field patterns

Near and far field patterns can provide valuable information of the spatial modes in a laser. It is well known that filamentation can cause undesired instabilities in the device performance. **Figure 5.12** shows the near field of a typical ridge-waveguide laser, which clearly demonstrates good current guiding in the lateral dimension and a single lasing filament.

A plot of light vs. current also shows no sign of kinks typically caused by mode

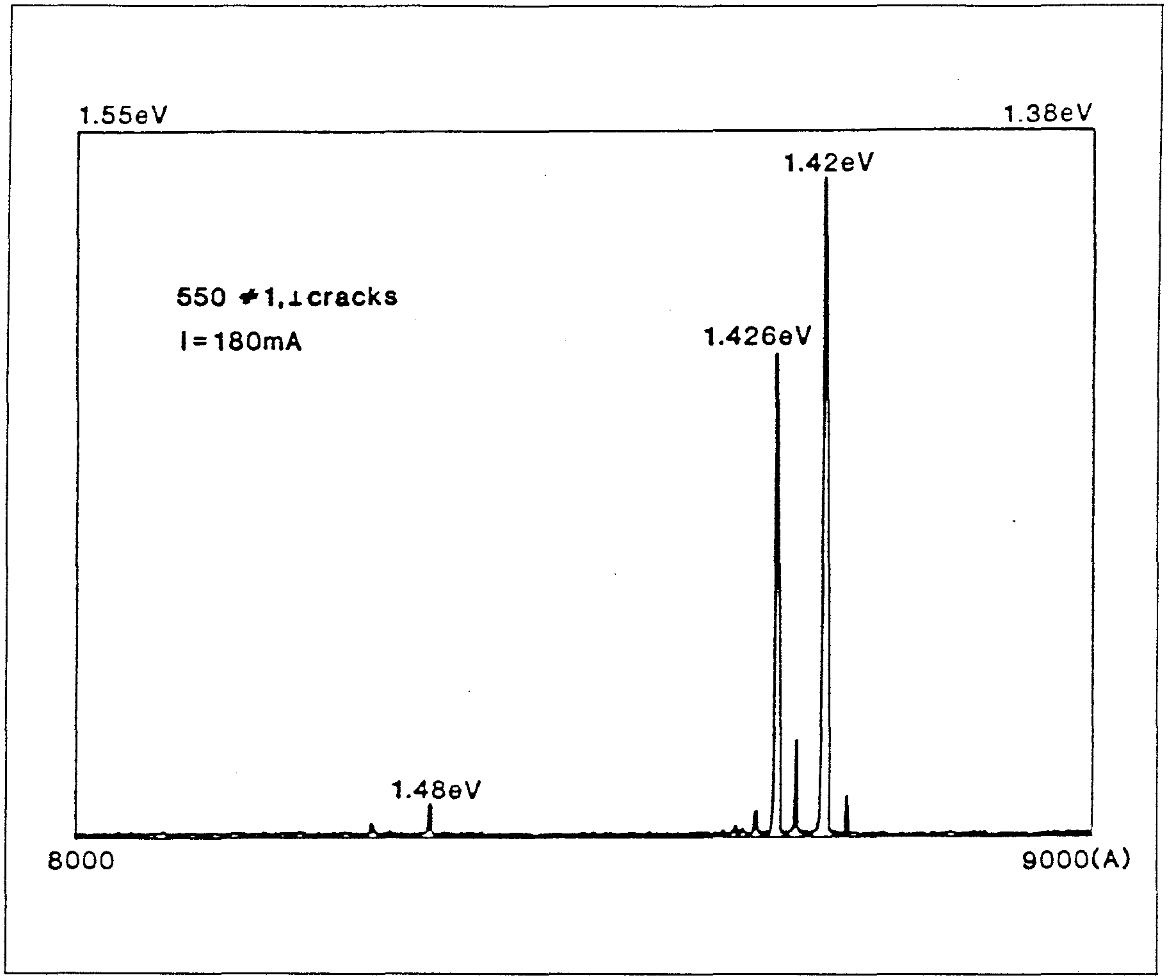

**Figure 5.11** *The optical spectrum obtained for a GaAs-on-Si stripe laser with surface cracks perpendicular to laser cavity.*

hoping. A very narrow and single lobed far field pattern (**Figure 5.13**) is also observed. The beam angle (in the lateral dimension) of 4.8° compares very well with that of typical GaAs-on-GaAs stripe lasers [15].

## § 5.6 Ridge-waveguide geometry stripe lasers

The response of a device is determined by the RC time constant in any high-speed microwave modulation measurement. In the case of a laser, the capacitance of the p-n junction can severely limit the speed of modulation. Stripe geometry lasers with small

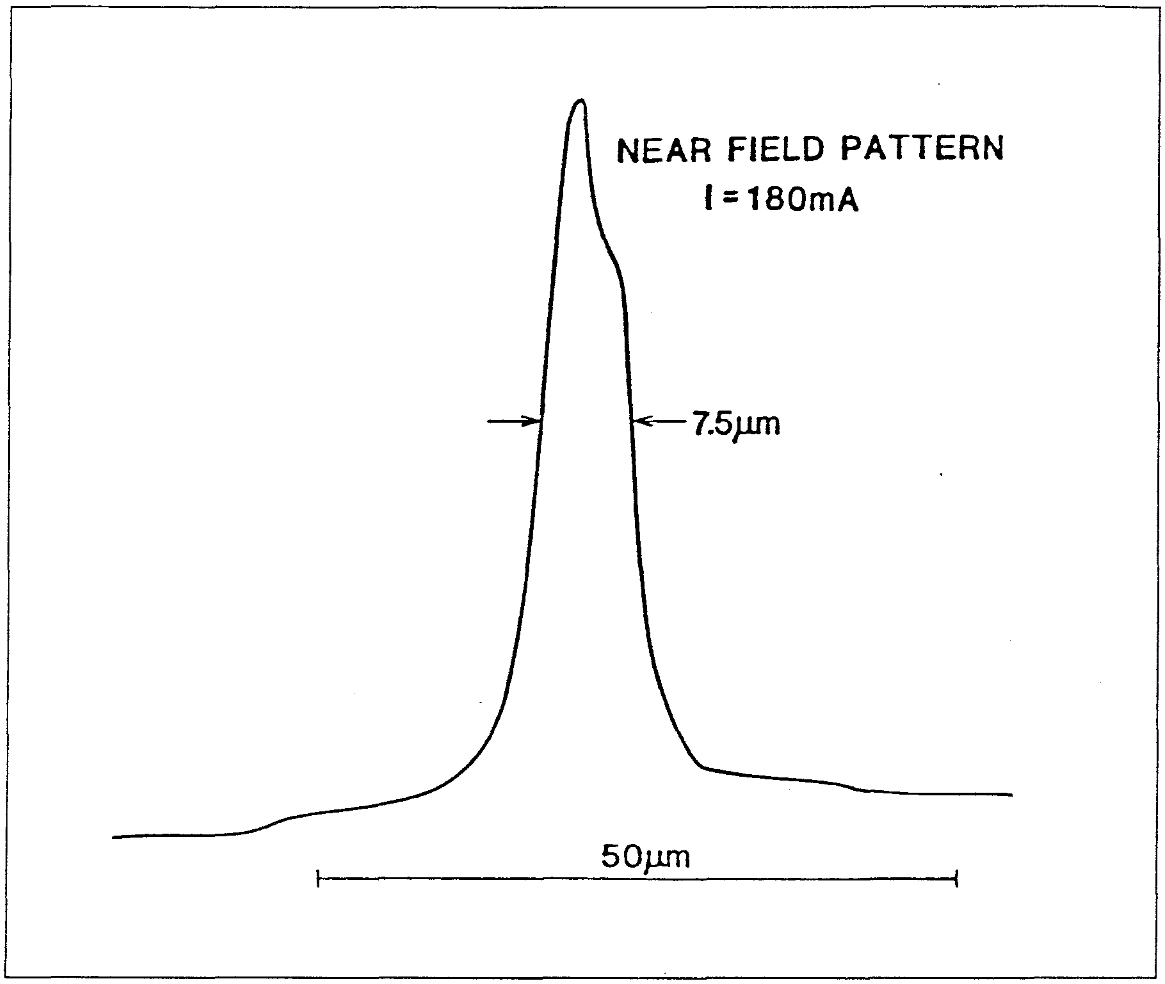

**Figure 5.12** *The near field pattern of a 10 µm GaAs-on-Si stripe laser which is biased at three times above its threshold.*

junction areas (capacitances) have been used for high-speed modulation experiments.

There are numerous structures of stripe geometry lasers published in literature, which can be put in two groups: (i) gain guided, and (ii) index guided. The index guided structures are usually fabricated by liquid phase epitaxy regrowth. The gain guided structures are based on the confinement of carriers by finite diffusion length. For example, if the stripe width is 1 µm, then the total current spread should be less than 10 µm at the junction. This current spread can be further reduced if a ridge

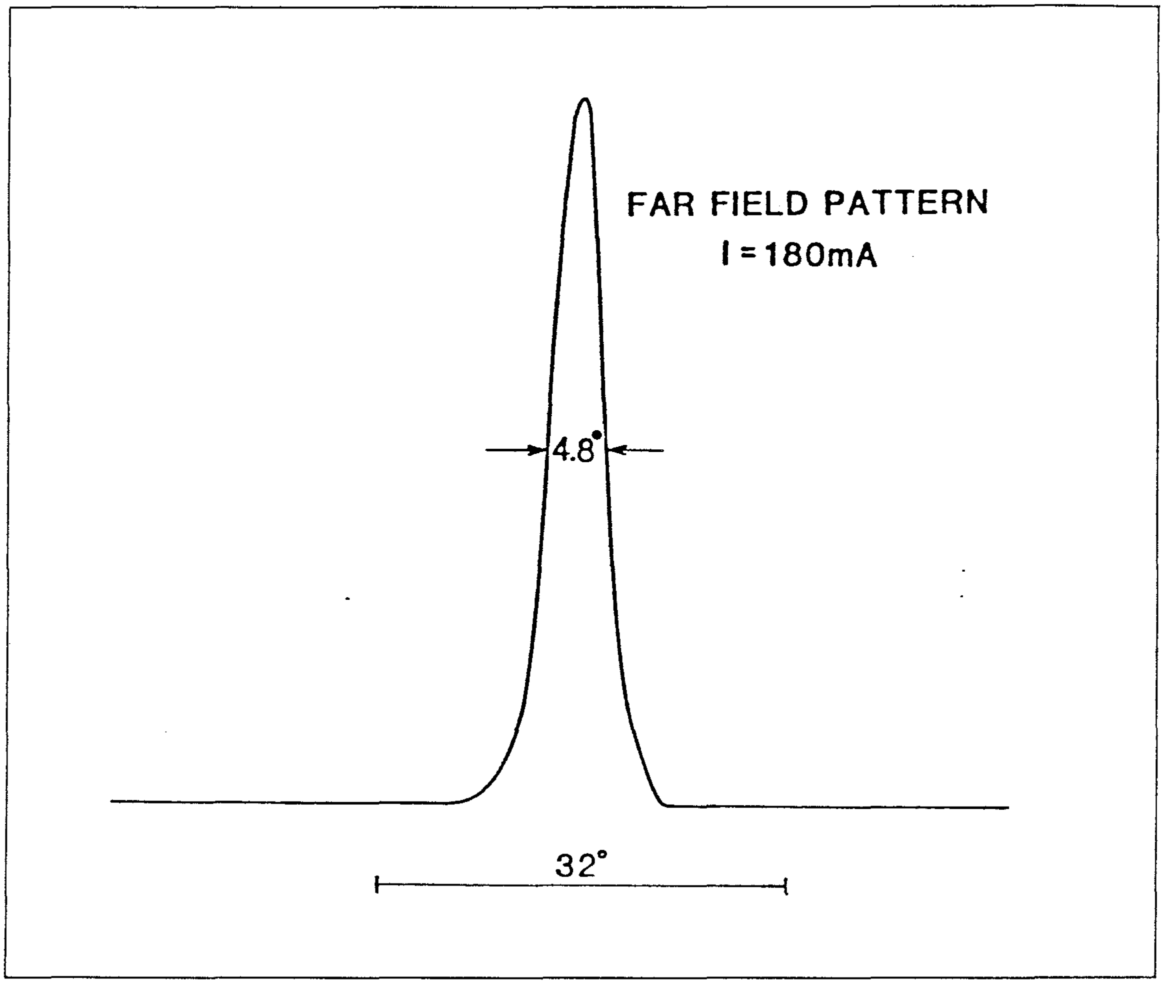

**Figure 5.13** *The lateral profile of the far field of a 10 μm GaAs-on-Si stripe laser which is biased at three times above its threshold.*

is etched. Gain guided structures with a etched ridge are call *ridge-waveguide* stripe lasers. These lasers do not have threshold currents as low as the index guided ones, but they are easy to fabricate and can be obtained in large quantities.

This procedure (**Appendix VI**) is the one we have been using in this thesis work and it has the 10 steps.

## § 5.7 High-speed modulation of GaAs-on-Si stripe lasers

One of the most important goals in GaAs-on-Si research is to modulate GaAs lasers on Si substrate using microwave signals that can be generated from a Si VLSI chip, or from a GaAs chip on the same Si wafer. Such modulation takes advantage of the optoelectronic capability of GaAs and the state-of-the-art of Si VLSI technology in future supercomputer systems.

The stripe laser used in modulation experiments is shown in **Figure 5.14**, and the experimental set-up is shown in **Figure 5.15**. The stripe laser is mounted on a copper heatsink which is screwed onto a microwave package available from Ortel Corporation. The DC current bias and the microwave signal are applied through a microwave bias-Tee. The light from the laser is collected and collimated by a microscope objective, and then focused onto a high-speed photodetector (3dB bandwidth = 8GHz). The output of the photodetector is sent to a spectrum analyzer. The frequency response measurement is shown in **Figure 5.16**. As can be seen, the $10\mu m \times 380\mu m$ stripe laser exhibited a threshold current of 40 mA, a lasing wavelength of 8650 Å, and a modulation corner frequency of 2.5 GHz. The modulation was performed at frequencies as high as 4.5 GHz [15,16].

This result compares very favorably with those obtained from GaAs-on-GaAs lasers of similar structures (they have a corner frequency of about 2 GHz [17]). Furthermore, such a laser can be used in as chip-to-chip optical link together with a high-speed GaAs-on-Si detector.

## § 5.8 High-speed GaAs-on-Si p-i-n detectors

Si is not a good material for detecting GaAs laser emission at high-speed since Si has a large absorption depth of nearly $10\mu m$ and thus a long sweep-out time proportional to this length. GaAs on the other hand, has only a absorption depth of about $1\mu m$ and a carrier speed two times higher. As a result, GaAs is expected to out perform Si at high-speed by a factor of 20 at the same sensitivity level.

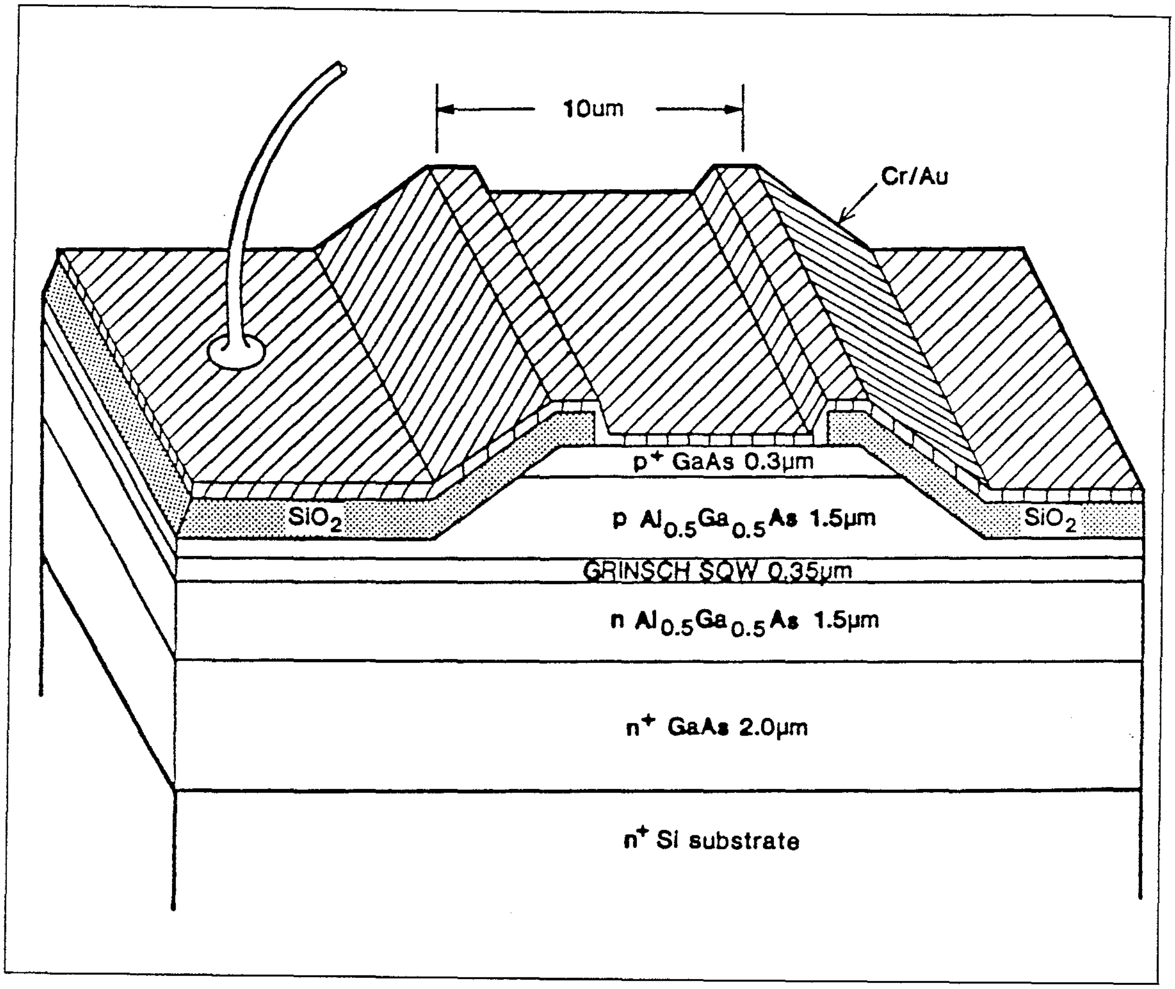

**Figure 5.14** *Schematic drawing of a ridge-waveguide stripe geometry laser used in the high-speed modulation experiment.*

The growth of the GaAs-on-Si p-i-n detector is the same as that of lasers except the growth temperature was at 600°C for the entire p-i-n structure. The doping level for both p and n region is $1\times10^{18}\text{cm}^{-3}$. The structure of the p-i-n detector is shown in **Figure 5.17**. The width of the intrinsic region varies from 1 to 3 $\mu$m to balance the transit time and the RC time constant. The area of the junction is $70\times100\mu\text{m}^2$. The measurement apparatus is shown in **Figure 5.18**. The detector was biased through a microwave bias tee and illuminated with 5 ps optical pulses from a synchronously

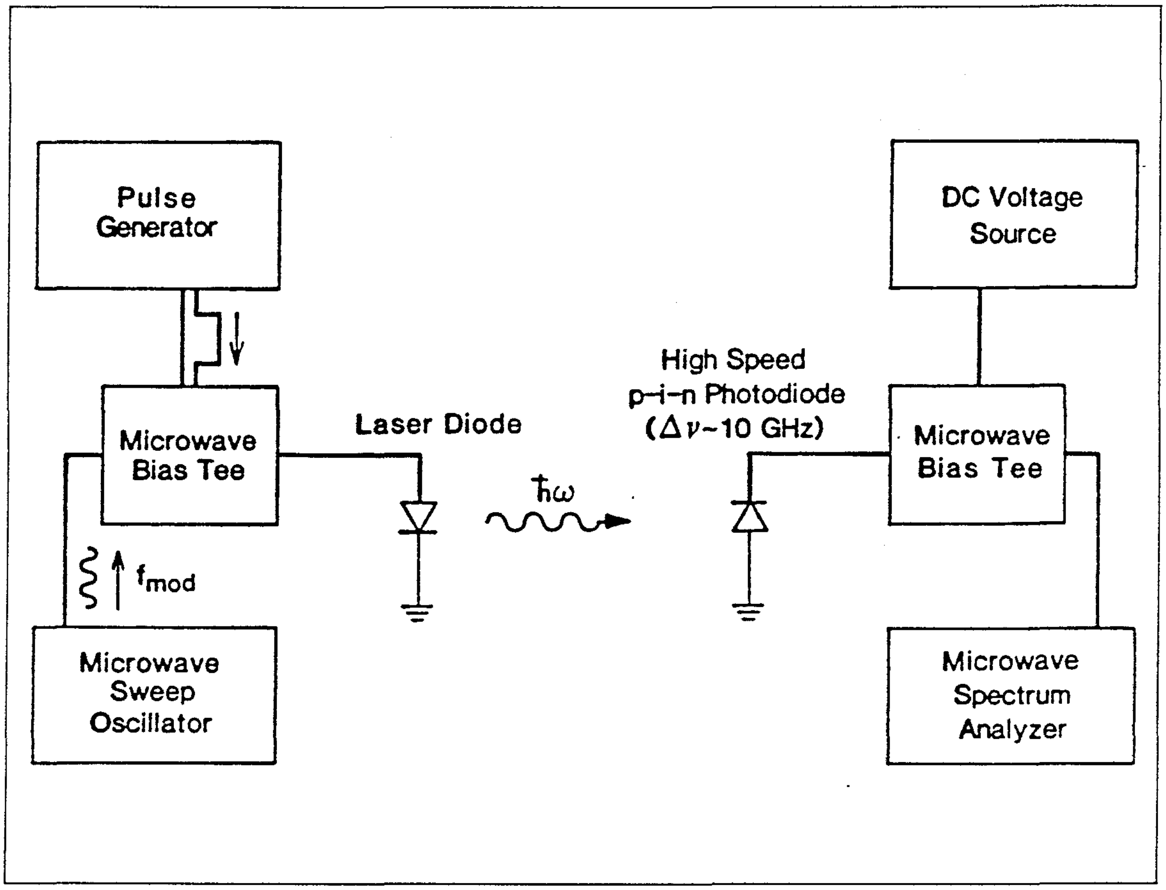

**Figure 5.15** *Schematic drawing of the experimental set-up of high-speed modulation measurement.*

pumped mode-locked dye laser ($\lambda$ =6000 Å) at a 100 MHz repetition rate. The output of the detector was then measured both with a sampling oscilloscope and a microwave spectrum analyzer. For a 2$\mu$m intrinsic region, the impulse response shows a 45 ps FWHM, corresponding to a 3dB bandwidth of 4 GHz (**Figure** 5.19). This compares very well with the results obtained with identical GaAs-on-GaAs p-i-n detectors fabricated using the same process [18].

## § 5.9 Conclusions

In this chapter, we have reviewed and discussed the details of the popular methods

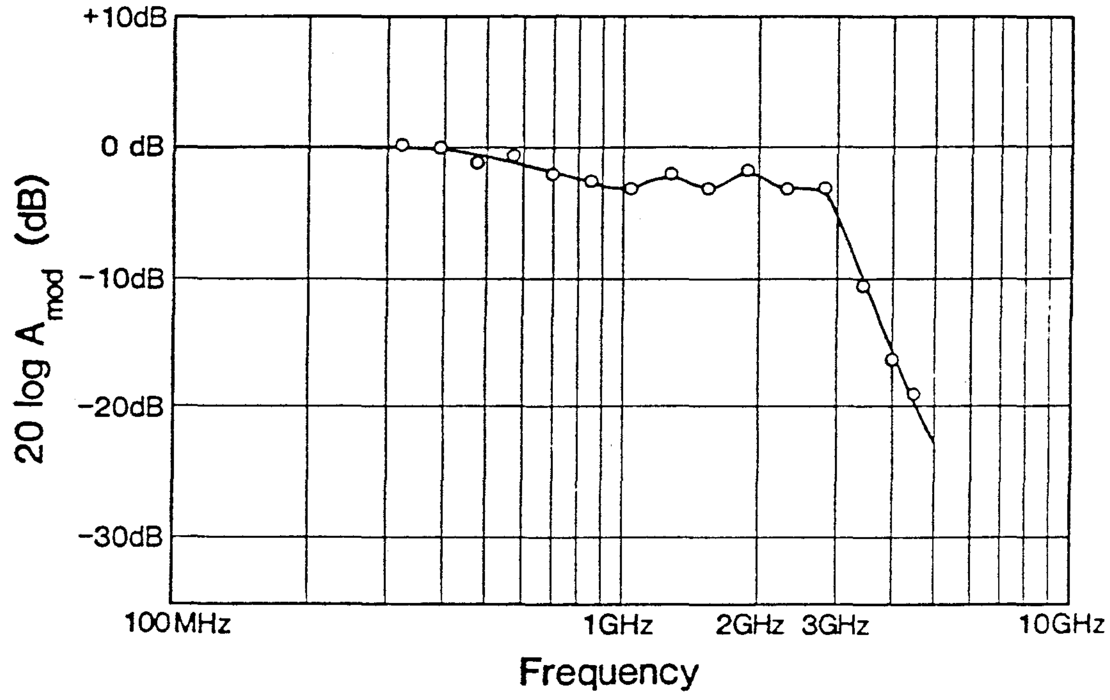

**Figure 5.16** *The modulation response versus frequency for a 10 × 380$\mu m^2$ stripe under direct microwave current modulation showing a 3dB bandwidth of 2.5GHz.*

used by us and other researchers in the field to grow high quality GaAs-on-Si substrates. Defect reduction is shown to be a major technological barrier in the growth of high quality GaAs-on-Si. Antiphase domain disorder can be avoided by the use of an As prelayer, and dislocations can be reduced by use of a tilted substrate. Very satisfactory results have been obtained using an As prelayer coverage and low substrate temperature at the beginning of the growth. Record low threshold current density lasers have been demonstrated, which eventually led to the first current-injected room temperature CW operation of GaAs-on-Si lasers. The fabrication of ridge-waveguide geometry stripe lasers is described. high-speed current modulation of GaAs-on-Si lasers has been

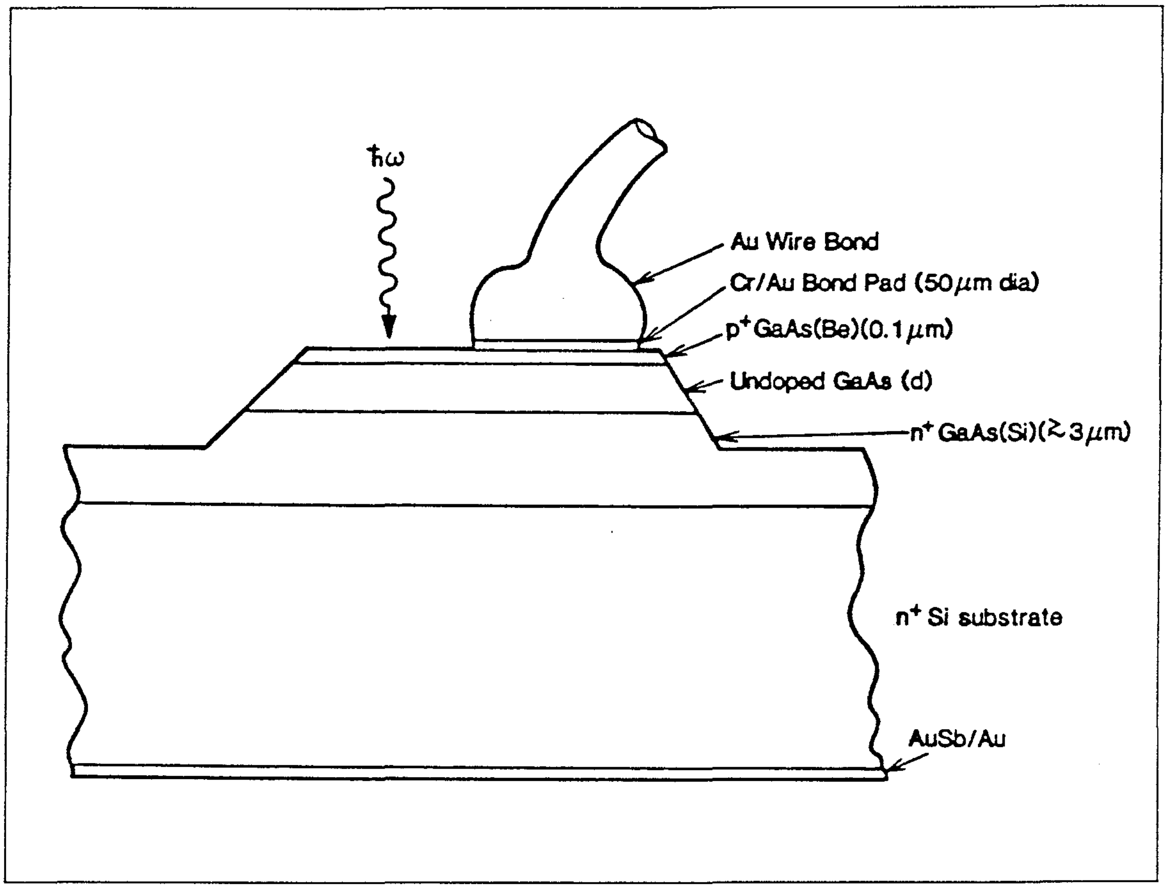

**Figure 5.17** *Schematic drawing of a p-i-n GaAs-on-Si photodiode.*

demonstrated, which opens the door to chip-to-chip communication in a Si VLSI system [19]. High-speed photodetectors have also been demonstrated in this study.

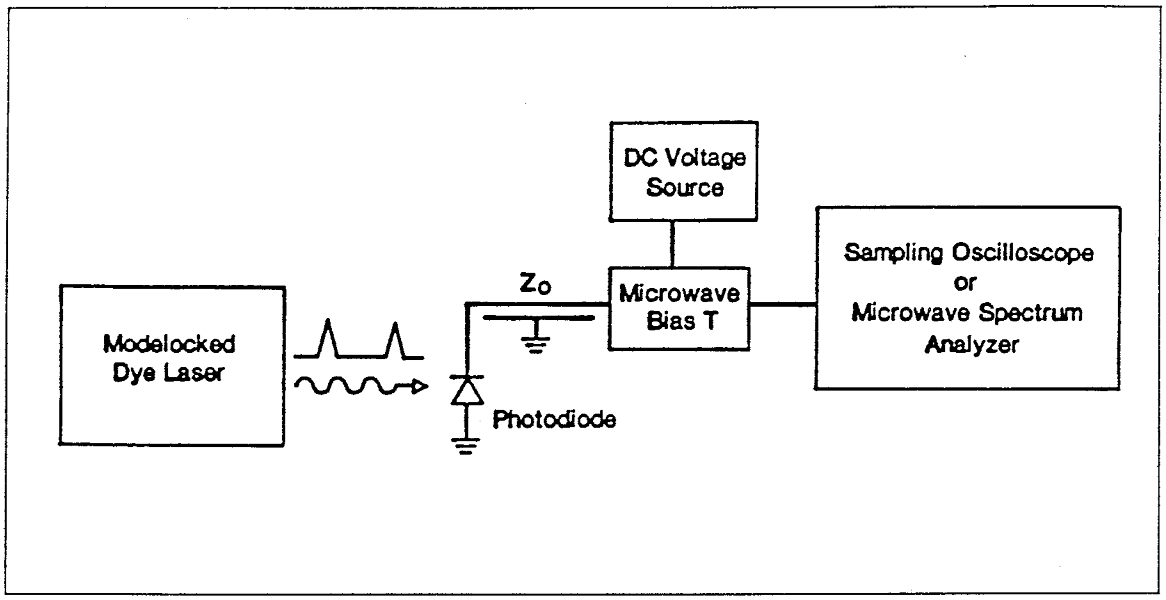

**Figure 5.18** *Schematic drawing of the experimental set-up used in the measurement of a p-i-n detector.*

## § 5.10 References

[1] R. C. Henderson, J. Electrochem. Soc. , **119**, 772(1972).

[2] R. Houdre and H. Morkoç, *CRC Critical Review*, to be published.

[3] W. I. Wang, Appl. Phys. Lett. , **44**, 1149(1984).

[4] R. Kaplan, Surf. Sci. , **93**, 145(1980).

[5] R. Fisher, H. Morkoç, D. A. Neumann, H. Zabel, C. Choi, N. Otsuka, M. Longerbone, and L. P. Erickson, J. Appl. Phys. , **60**, 1640(1986).

[6] W. T. Masselink, T. Henderson, J. Klem, R. Fisher, P. Pearah, H. Morkoç, M. Hafich, P. D. Wang, and G. Y. Robinson, Appl. Phys. Lett. , **45**, 1309(1984).

[7] see Ref. [2] for more details.

[8] N. Otsuka, C. Choi, L. A. Kolodziejski, R. L. Gunshor, R. Fisher, C. K. Peng, H. Morkoç, Y. Nakamura, and S. Nagakura, J. Vac. Sci. Technol. , **B4**, 896(1986).

[9] R. Fisher, D. Neumann, H. Zabel, H. Morkoç, C. Choi, and N. Otsuka, Appl. Phys. Lett. ,

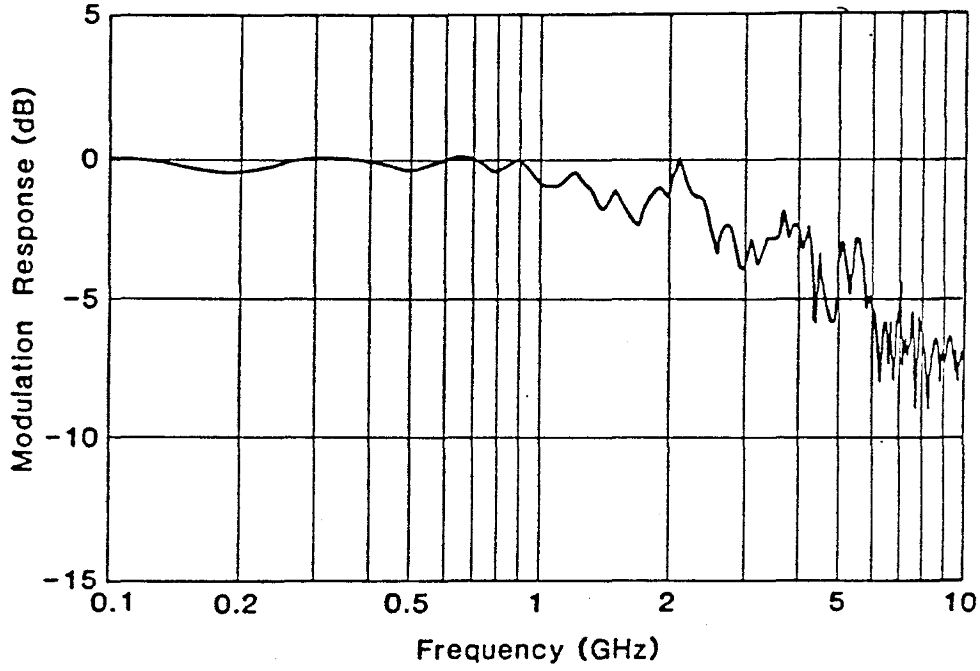

**Figure 5.19** *The modulation response versus frequency of a GaAs-on-Si p-i-n photodetector showing a 3dB band width of 4GHz.*

**48**, 1223(1986).

[10] C. Choi, N. Otsuka, G. Munns, R. Houdre, H. Morkoç, S. L. Zhang, D. Levi, and M. V. Klein, Appl. Phys. Lett. , to be published.

[11] R. D. Dupuis, J. P. Van der Ziel, R. A. Logan, J. M. Brown, and C. J. Pinzone, Appl. Phys. Lett, **50**, 407(1987).

[12] H. Z. Chen, A. Ghaffari, H. Wang, H. Morkoç, and A. Yariv, Appl. Phys. Lett. , **51**, 1320(1987).

[13] I. Hayashi, M. B. Panish, P. W. Foy, and S. Sumski, Appl. Phys. Lett. , **17**, 109(1970).

[14] H. Z. Chen, A. Ghaffari, H. Wang, H. Morkoç, and A. Yariv, Opt. News, 13, Oct. , 4(1987), Dec. , 12(1987), also Photonic Spectra, **21**, 36(1987), and Semicon. Int. , **10**, 22(1987).

[15] H. Z. Chen, J. Paslaski, A. Ghaffari, H. Wang, H. Morkoç, and A. Yariv, IEEE IEDM Tech. Digest, 238(1987).

[16] H. Z. Chen, J. Paslaski, A. Yariv, and H. Morkoç, Research and Development, 61, Jan. , 1988.

[17] K. Lau and A. Yariv, *Semiconductor and Semimetals*, ed. W. T. Tsang, (Academic, Orlando, Fl, 1985), Vol. 22, p. 69.

[18] J. Paslaski, H. Z. Chen, H. Morkoç, and A. Yariv, Appl. Phys. Lett. , **52**, 1410(1988).

[19] H. Z. Chen, J. Paslaski, A. Yariv, and H. Morkoç, Opt. News, **14**, 24(1988).

# Appendix I

## Operation and Maintenance of an MBE System

### § I.1 An introduction

The operation and maintenance of an MBE system has been characterized as a *black art* because of the tremendous difficulty in teaching it. No manual can cover everything that can happen during MBE operations, and one has to make correct judgments and swift actions. There are however a few things that are established and proven effective through our extensive use of MBE. The purpose of this chapter is not to present a general review of MBE operations, but to present the operating procedure we use with regularity. Although some of the procedures only apply to our Riber-2300 system, most of them are quite general. The interested reader can use this to supplement the MBE user's manual [1] and a general book on high vacuum systems [2].

An MBE system contains a UHV (ultra-high vacuum) processing environment which employs unparalleled cleanliness, a large heating power input of about $1kW$, and frequent mechanical shutter movements. In order to satisfy these demanding specifications, more complex molecular beam and crystal growth monitoring instruments are being introduced into the system, making it impossible for anyone not familiar with MBE to fully understand its operation and appreciate its enormous capability. Therefore, we begin with a discussion of the minimum requirements of an MBE system.

## § I.2 Minimum system requirements

In general, complexity implies poor reliability. Such is the case for a fully equipped MBE system. Each component of an MBE system has a lifetime of say, 3 years, but there are so many of them operating at the same time. For example, there are: 8 effusion cells and shutters; 1 RHEED system; 1 mass spectrometer; 10 thermal couples; 1 sample manipulator; 3 major viewports; 2 vacuum gauges; 8 power supply units; 1 flux gauge; ... etc. As a result, statistically, we can *always* expect some kind of problem with MBE at any given time. Therefore, the most important thing is to know which components are absolutely essential to a good crystal growth and how to cope with the failures of non-essential parts.

Let's first look at the important components of an ideal MBE operation and determine which ones are absolutely required.

### Vacuum.

No leak, especially on the growth chamber, is allowed. A leak will introduce $O_2$ into the vacuum system which is very detrimental to the growth of high quality GaAs/AlGaAs layers since it forms a deep trap at mid-bandgap where the impurity recombination is strongest. A leak also results in a high density of surface defects. Without $LN_2$ cooling, the system pressure can be as high as $5 \times 10^{-6}$torr, while it should reach at least $2 \times 10^{-9}$torr or lower with $LN_2$ cooling .

### Pyrometer

This is used to monitor the temperature of the substrate surface before and during a growth. Ideally, a pyrometer can provide valuable information to an operator since growth temperature is probably the single most important parameter. However, the viewport in front of the pyrometer slowly gets coated by As, and sometimes almost no light can go through it. When this alone happens, the operation of MBE should be continued. To obtain the substrate growth temperature, which can be used to regulate the heating power, one needs to go back to the previous record when the viewport was not coated and find out the pyrometer reading and the substrate heating power ($P = IV$) and use the same power $P$.

### RHEED

RHEED (Reflection High Energy Electron Diffraction) provides dynamic information on the surface structure of the substrate and growing films; in particular, it signals when the oxide layer on the surface has desorbed and when growth should begin. If the screen in front of the RHEED is coated by As, one can go back to the previous record when the RHEED was working and find the heating power at which the oxide film was thermally removed.

### Tantalum shutters

If the Ga or As shutter can not be closed, growth may proceed since we always need Ga and As. But if either one of them can not be opened then we must repair it. The Al shutter has to be opened if one needs to grow AlGaAs; a malfunctioning Al shutter restricts the growth to GaAs alone. Si and Be shutters are needed to be open at least (if they don't close) if a p-n junction (such is the case of a laser) is to be grown. When Si or Be shutter can not be closed, the molecular beam from the cell has to be cut down by reducing its heating power as rapidly as possible.

### Computer

We use a computer to automatically control the heating powers by sending temperature settings to the power supply regulators, recording temperatures, and synchronizing the cells. If the computer is down, one can simply put the control switch on regulator to "local" instead of "remote" mode and operate manually.

## Flux gauge

A flux gauge measures the beam flux from a cell. It can tell us for example, the Ga to As ratio (normally around 1:6). This is not very important since we always try to find the minimum As flux for the purpose of saving As and to obtain better AlGaAs growth quality.

The minimum requirements of a working MBE system, therefore, include a good vacuum and several good shutters and a detailed record of each previous operation.

## § I.3 The proper vacuum pumping procedure

An MBE system usually has four (at least three) pumping stages. A first mechanical pump brings pressure to 100 mmHg. A cryosoption pump then brings it to $10^{-4}$ torr, followed by a titanium sublimation pump (TSP) which brings it to $10^{-5}$ torr. Finally, an ion pump pumps it down to $10^{-7} \rightarrow 10^{-11}$ torr. The use of TSP is optional but usually is recommended since it will help the ion pump last longer and the TSP filaments can be replaced easily. After the MBE system is opened, it should be flushed a few times with $N_2$ (to remove water vapor, etc.) and finally be filled with clean $N_2$ ($N_2$ has a high pumping efficiency in cryosorption pumps). At first, the mechanical pump is used to stream out $N_2$. Then three cryosorption pumps should be used in the following way: the first one is open as long as the streaming-out of gas molecules lasts (because the $N_2$ molecules can stream out the hard-to-pump argon molecules); the second pump is open for as long as it pumps; and finally to the third pump. When the third pump stops pumping, the TSP should be turned on. After a short outgasing of a filament inside the TSP ( now the valve is still open to cryosorption pumps), the valve to the outside is closed and the TSP pumps down fast. When the TSP stops pumping, the ion pump is switched on to reach a UHV environment.

### MBE system baking

Each time the MBE system has been opened to air for repair and/or recharge, it has to be baked. The purpose of baking is to heat up the MBE system to a temperature high enough that most gas molecules condensed during opening will outgas, yet the temperature is low enough that the ion pump can handle the pumping. The heating is done with heater tapes rather than with the baking oven provided by Riber. The heating power can be directly controlled by the electrical current. The ion pump is equipped with a protection mechanism that will turn it off when the pressure reaches above $1\times10^{-4}$torr, so a safe baking pressure is slightly below $5\times10^{-5}$torr. The ion-pump can also be baked at the same time.

The three cryosorption pumps should be baked and pumped while not being used to maintain their pumping ability.

## § I.4 Handling and changing source materials

Whenever a source material (usually As) runs out, it has to be refilled. Whenever we open the MBE to replace or repair something, the source materials in the effusion cells become oxidized and should be replaced. As is often the case, we wait to open the MBE system to repair some broken parts and replace or refill some source materials at the same time.

The source materials used in a MBE system are contained in pyrolitic boron nitride (PBN) crucibles which have a impurity level of less than 10 parts per million, and do not dissociate below 1400°C. Before we change an old crucible, the new one is always put in a separate small vacuum system and outgased at 1200°C for several hours in a Knudsen cell. The source materials should be handled differently. Al chunks can be lightly etched in HCl and rinsed in deionized water. Ga (purchased with seven 9's purity) is usually contained in a plastic bottle which needs to be kept at about 40°C in liquid form. As chunks are usually concealed in a glass ampule under an inert gas since As reacts with $O_2$ easily. Be is usually contained in a glass bottle. Cleaned Al chunks can be put into a crucible with a tweezers; Ga liquid can be poured into a crucible; and As chunks can be dumped into a crucible carefully. Be flakes have to be handled with extreme care since Be is highly toxic. A plastic glove box is used to handle Be; but fortunately, Be material can last a very long time and only needs to be refilled about every 5 years. Si is available in ingot form, and it can be loaded into the MBE system without further cleaning.

The Al cell, when not in use, should be kept above 700°C since the melting point of Al is around 550-600 °C, and a rapid heating or cooling through this point causes a sudden change of volume, which can crack the PBN crucible and damage the entire effusion cell. The Ga cell is kept at 200°C when not used for the same reason.

The As cracker cell (manufactured by Perkin-Elmer) has two main parts: a large crucible in the back to hold enough As material that can last for a year, and a long and thin Mo tube in the front to crack $As_4$ to $As_2$. The Mo tube should always be heated before the source As gets hot to prevent As from clogging in the Mo tube.

Finally, there is the problem of hole-burning on Ga and Al shutters (unfortunately the Riber specialists have not been able to explain the cause) which occurs every year. The solution to this is to keep Ga and Al cell temperatures down as much as possible before the shutters are opened.

## § I.5 Calibrations

Growth rate of GaAs and AlGaAs, Al mole fraction, Si and Be doping levels all change after the MBE system is opened. Therefore, many calibrations have to be performed before any device can be grown.

## Doping concentration calibrations

Two measurements are performed: the Hall measurement, and the capacitance-voltage (C-V) measurement.

In the case of Hall measurement, both the mobility and concentration of free carriers are obtained. The measurement can also be done at liquid nitrogen temperature 77K in a specially designed dewar to obtain the effect of impurity on carrier mobility. A sample with a constant doping profile and a given thickness (e.g., 1$\mu$m) is grown by MBE for the Hall measurement. To make ohmic contacts for a four-point van der Paul measurement, four small In balls are pressed onto the four corners of a square sample, which is then annealed in hydrogen gas for 20 seconds at 400°C. The sample is then put into a specially designed holder for measurement.

In the case of C-V measurement, there is no need for making any ohmic contact since the measurement relies on the formation of a Schottky contact between Hg and sample by a commercially available mercury probe that allows liquid mercury to form a Schottky barrier to GaAs. The capacitance of this reverse biased diode is then measured as a function of biasing voltage and information on doping level can then be obtained.

## Growth rate calibrations

Since GaAs is grown at 600°C and AlGaAs at 720°C, we need to measure $r_{GaAs}(600)$, $r_{GaAs}(720)$, $r_{AlAs}(720)$, where $r$ refers to the growth rate, with the help of a scanning electron microscope (SEM) together with a photoluminescence setup (PL) known as cathodoluminescence (CL). We need to grow, for example, one hour of each material, and then put this stack of materials into the CL system to measure the thicknesses as well as the cathodoluminescence from each layer and calculate the growth rates and Al mole fractions.

Al mole fraction $x$ in $Al_xGa_{1-x}As$ is related to the direct energy bandgap in the following way

$$E_g^{\Gamma}(x) \;=\; 1.424 \;+\; 1.247x \; eV \qquad\qquad for \; x \; < 0.45$$

and

$$E_g^{\Gamma}(x) \;=\; 1.424 \;+\; 1.247x \;+\; 1.147(x-0.45)^2 eV \qquad\qquad for \; x \; \geq 0.45 \tag{3.1}$$

Therefore, if we know $E_g^{\Gamma}(x)$ we can determine $x$.

$E(x)$ can be obtained from the spectrum measured by CL using the following relationship:

$$E(\hbar\omega) \;=\; \frac{12398}{\lambda_{peak}(\mathring{A})} \; eV \tag{3.2}$$

where $\lambda_{peak}$ is the peak of PL curve. Thus $x$ can be determined. Once $x$ is determined, one can easily estimate the growth rate of $Al_xGa_{1-x}As$ by

$$r_{AlAs} \;=\; \frac{x}{1-x} \; \mu m/h \qquad and \qquad r_{AlGaAs} \;=\; r_{GaAs} \;+\; r_{AlAs} \tag{3.3}$$

and use the result as a double-check of growth rates.

## § I.6 Conclusions

In this chapter, the techniques of daily maintenance of an MBE system are described and are discussed from an operations point of view. Although there are many sophisticated instruments installed in an MBE system, only a few of them are required for growing high quality epitaxial material. The key to a consistent and long-lasting MBE operation is keeping a good record of all MBE data including substrate temperature, heating power, and vacuum level at all stages for each growth.

## § I.7 References

[1] Riber user's manual.

[2] J. F. O'Hanlon, *A User's Guide to Vacuum Technology*, John Wiley and sons, New York, 1980.

# Appendix II

## GaAs wafer cleaning procedure

The procedure we have been using is the same one used by the Morkoç group at University of Illinois, and it has the following steps:

1. Boiling substrate in trichloroethylene (TCE) several times. The purpose is to remove any wax or oil-based contaminations on a wafer. This step can also be done with a hot (70°C) $H_2SO_4$ solution with similar effect.
2. Rinse substrate in acetone, methanol, and deionized water several times. The purpose is to remove TCE with acetone, remove acetone with methanol, and remove methanol with water, since acetone does not dissolve very well in water.
3. Blow dry the substrate with filtered nitrogen. This is important because the next few steps involve the use of pure $H_2SO_4$.
4. Put substrate in hot (70°C) $H_2SO_4$ for 5 minutes. The purpose is to remove any residual organics left from previous cleaning. The temperature of $H_2SO_4$ has to be kept below 100°C, otherwise there will be surface reactions between GaAs and $H_2SO_4$ as we have experienced. When this happens, the process should be continued since this bad-looking surface layer will be etched away next.
5. Put substrate in cold (25°C) $H_2SO_4$ for 5 minutes, then transfer it to 4:1:1

($H_2SO_4$:$H_2O_2$:$H_2O$) to etch for 5 minutes. The purpose is to etch away a few microns of GaAs surface material that may contain surface contaminations such as carbons, structural defects, etc.

6. Transfer the substrate to another cold $H_2SO_4$ for 1 minute, and rinse in running deionized water for 5 minutes. The long rinsing removes any $H_2SO_4$ left on the surface.
7. Transfer the substrate to HCl for 1 minute. This will remove the very thick oxide layer on the surface which resulted from a previous 5-minute 4:1:1 etch.
8. Rinse in deionized water again for 5 minutes, and blow dry with filtered nitrogen.

# Appendix III

## Technique of growth interruption

It has become increasingly popular in the MBE community to apply growth interruption techniques to improve interface quality. The purpose of a growth interruption is to allow the growing surface to relax (or to reconstruct) following a change in atomic composition (such as Al grading in AlGaAs). Such a technique can improve the quality of "inverted" GaAs on AlGaAs. The procedure for the (Ga,Al)As system is the following:

1. close Al shutter
2. drop substrate temperature from 720°C to 600°C
3. grow a thin layer of GaAs (one monolayer)
4. close all shutters (Ga, Si, Be, etc.) except As and wait for 1 minute
5. open Ga, Si, and Be shutters and grow one monolayer of GaAs
6. open Al shutter and raise substrate temperature to 720°C

# Appendix IV

## Fabrication of broad area lasers

The fabrication procedure of broad area lasers consists of the following steps:

1. First, cleave a small piece of sample, usually smaller than 1cm×1cm. See if the In on the back is smooth. If it is then one can use the spinner attached to a vacuum holder without a double-sided masking tape, to spin on a layer of photoresist. If the In is rough, the tape should be used. Since we will do a lift-off, a thick photoresist is preferred. AZ-4400 is used for a layer of thick metal layer and 1350J is used for a layer of thin metal.
2. Then put the sample in a 85°C oven for 30 minutes as a soft-bake to remove moisture and harden the photoresist so that we can put a mask on it. Some people prefer to use a infrared lamp to bake photoresist for 5 minutes; this is not a reliable method and it only saves about 20 minutes.
3. Photolithography is done with a mask. $100\mu$m wide openings separated by $150\mu$m wide photoresists are obtained. If the opening is not clear (residual resist on surface), the oxygen plasma can be used to remove a thin layer of photoresist on the sample especially in the openings.
4. The sample is slightly etched before it is brought into a metalization evaporator

where a 1000 Å of Au (AuZn is used if the p-doping in contact layer is not very high) is deposited. Lift-off is then done in acetone with the help of a cotton Q-tip.

5. The sample is then mounted upside down with wax to a lapping block. The back side with In is lapped until the total thickness of wafer is about 5 mils. It is then cleaved into desirable sizes for threshold current measurement.

# Appendix V

## Si wafer cleaning procedure

The details of this cleaning procedure is listed in the following:

1. Degreasing by boiling in trichloroethylene (TCE) 3 minutes, 3 times, rinse in acetone, methanol, deionized water and blow dry with filtered nitrogen. To remove heavy metal contamination use 60°C 1:1 ($HNO_3$:$H_2SO_4$) for 5 minutes.
2. 5:3:3 ($H_2O$:HCl:$H_2O_2$) at 60°C for 5 minutes
3. 2-minute rinse in $H_2O$
4. 1:10 (HF:$H_2O$) for 20 seconds
5. 2-minute rinse in $H_2O$
6. 5:3:3 for 2 minutes
7. 2-minute rinse in $H_2O$, 1:10 (HF:$H_2O$) for 20 seconds, 2-minute rinse in $H_2O$, go to step 4 and repeat 4 times.
8. 5:3:3 for 5 minutes.
9. rinse in $H_2O$ and blow dry with nitrogen.

# Appendix VI

## Fabrication of stripe lasers

The procedure described below is the one we have been using in this thesis work. It has the 10 steps:

1. Photolithographically define 5 $\mu$m wide photoresist stripes along $(01\bar{1})$ facet.
2. Hard bake for at least 2 hours, sometimes the wafer can be left for overnight.
3. Etch in 1:3:40 ($H_2O_2$:$H_3PO_4$:$H_2O$) at 1000 Å per minute rate until 0.25 $\mu$m away from the GRIN region (waveguide).
4. Grow silicon dioxide film all over the entire surface. The thickness of the oxide film is not as important as the smoothness.
5. Photolithographically define 1 $\mu$m wide photoresist openings centered on top of the oxide-covered ridges.
6. Hard bake it overnight. Insufficient baking results in rough edges in oxide etch.
7. Etch silicon dioxide in buffered hydroflouric acid (BF HF) according to the thickness and etching rate of the BF HF.
8. Photolithographically define 100 $\mu$m wide photoresist openings centered over the ridge.
9. Evaporate on 1000 Å Au and lift-off in acetone solution.

10. Lap the back substrate to 4-5 mils and put on 1000 Å Au for back contact.